Complete dipole response in ^{208}Pb from high-resolution polarized proton scattering at 0°

Vollständige Dipolstärkeverteilung in ^{208}Pb aus hochauflösender polarisierter Protonenstreuung unter 0°
Zur Erlangung des Grades eines Doktors der Naturwissenschaften (Dr. rer. nat.)
genehmigte Dissertation von M. Sc. (V.N. Karazin Kharkiv National University) Iryna Poltoratska
aus Kamianets-Podilskyi, Ukraine
Mai 2011 — Darmstadt — D 17

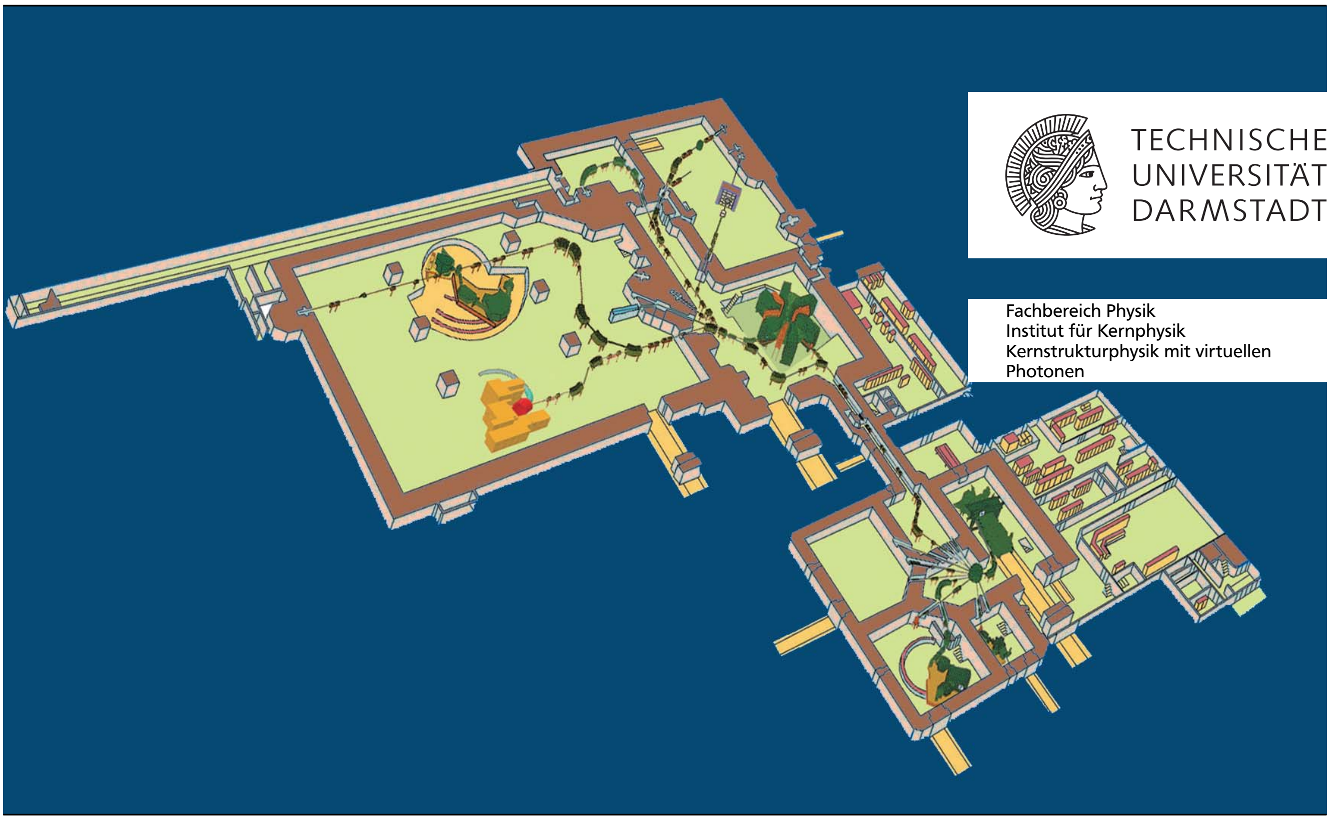

TECHNISCHE
UNIVERSITÄT
DARMSTADT

Fachbereich Physik
Institut für Kernphysik
Kernstrukturphysik mit virtuellen Photonen

Supported by the DFG through SFB 634 and 446JAP 113/267/0-2.

Complete dipole response in ^{208}Pb from high-resolution polarized proton scattering at 0°
Vollständige Dipolstärkeverteilung in ^{208}Pb aus hochauflösender polarisierter Protonenstreuung unter 0°

Genehmigte Dissertation von M. Sc. (V.N. Karazin Kharkiv National University) Iryna Poltoratska aus Kamianets-Podilskyi, Ukraine

1. Gutachten: Prof. Dr. Peter von Neumann-Cosel
2. Gutachten: Prof. Dr. Jochen Wambach

Tag der Einreichung: 15. Februar 2011
Tag der Prüfung: 4. Mai 2011

Darmstadt — D 17

Bitte zitieren Sie dieses Dokument als:
URN: urn:nbn:de:tuda-tuprints-26719
URL: http://tuprints.ulb.tu-darmstadt.de/2671

Zusammenfassung

Am Research Center for Nuclear Physics, Osaka, Japan, wurde die inelastische Streuung polarisierter Protonen am Kern ^{208}Pb bei einer Energie von $E_p = 295$ MeV und Streuwinkeln von $\Theta_{lab} = 0° - 10°$ untersucht. Hierbei wurde eine Energieauflösung der Größenordnung $\Delta E/E \approx 8 \cdot 10^{-5}$, was einer Halbwertsbreite von $\Delta E = 25 - 30$ keV entspricht, erreicht.

Die dominierenden Beiträge zum Wirkungsquerschnitt unter extremen Vorwärtswinkeln stammen von E1 Übergängen, angeregt durch die Coulomb-Wechselwirkung, sowie Spin M1 Anregungen, resultierend aus dem Spin-Isospin Anteil der Proton-Nukleon-Wechselwirkung. Eine Trennung dieser Anteile mit zwei unabhängigen Methoden durch eine Multipolanalyse der Winkelverteilungen und die Messung der Polarisationstranferobservablen D_{SS} und D_{LL} führt zu konsistenten Resultaten innerhalb der experimentellen Fehler.

Die Extrahierung der B(E1)-Stärkeverteilung im Energiebereich zwischen 5 und 20 MeV zeigt eine sehr gute Übereinstimmung mit vorhandenen Daten aus (γ,γ') Experimenten unterhalb der Neutronenseparationsschwelle und Photoabsorptionexperimenten im Energiebereich der Dipolriesenresonanz. Die Winkelverteilungen deuten auf eine unterschiedliche Struktur der E1-Übergänge unter- und oberhalb von 8.2 MeV hin. Die Schwerpunktsenergie und die summierte B(E1)-Stärke der Pygmydipolresonanz wurden zu E_c=7.43(2) MeV bzw. $\sum\limits_{6.2\ \mathrm{MeV}}^{8.2\ \mathrm{MeV}} \mathrm{B(E1)}=1.54(16)\ \mathrm{e^2fm^2}$ bestimmt. Oberhalb der Neutronenschwelle ($S_n = 7.367$ Mev) wurde bislang unbeobachtete Stärke bis zu einer Energie von 8.2 MeV gefunden.

Außerdem konnte im Energiebereich von 5 bis 19 MeV die E1 Polarisierbarkeit zu $\alpha_D = 18.7(13)\ \mathrm{fm^3/e^2}$ bestimmt werden. Eine Mittelung über alle vorhandenen Daten liefert einen sehr präzisen Wert $\alpha_D = 18.9(5)\ \mathrm{fm^3/e^2}$. Aufgrund der starken Korrelation in mikroskopischen Modellen liefert dies eine wichtige Einschränkung der Dicke der Neutronenhaut in ^{208}Pb und der Dichteabhängigkeit der Symmetrieenergie.

Die Feinstruktur der Dipolriesenresonanz wurde mittels Wavelet-Methoden analysiert. Es konnten charakteristische Skalen bei Energien von 100 keV, 340 keV, 520 keV, 1 MeV und 2.1 MeV gefunden werden. Ein Vergleich mit mikroskopischen Modell-rechnungen, die eine Kopplung von Zweiteilchen-Zweiloch-Zuständen beinhalten, lassen auf einen Anteil von Landau-Dämpfung an der Breite schließen.

Mit Hilfe einer Fluktuationsanalyse wurde die Niveaudichte der 1^- Zustände im Energiebereich der Dipolriesenresonanz bestimmt. Alle phänomenologischen und mikroskopischen Modelle scheitern an der Beschreibung der Niveaudichte in ^{208}Pb mit Ausnahme einer Version des back-shifted Fermigas-Modells, das zusätzliche phänomenologische Parameter in lokalen Massenregionen zulässt.

Abstract

At the Research Center for Nuclear Physics, Osaka, Japan, the ^{208}Pb$(\vec{p},\vec{p}')$ reaction was measured at $E_p = 295$ MeV and scattering angles $\Theta_{lab} = 0° - 10°$. A high energy resolution of the order of $\Delta E/E \approx 8 \cdot 10^{-5}$ was achieved, corresponding to $\Delta E = 25 - 30$ keV (FWHM).

Cross sections were extracted by a multipole decomposition analysis of the angular distributions. Dominant contributions at very forward angles originate from E1 excitation due to Coulomb projectile-target interaction and spin M1 transitions caused by the spin-isospin part of the proton-nucleus interaction. A separation of these contributions was performed with two independent methods, viz. a multipole decomposition of the angular distributions and utilizing polarization transfer observables. Excellent agreement between both techniques is achieved within errors bars.

The B(E1) strength distribution was extracted in the energy range between 5 and 20 MeV. Below the neutron separation energy ($S_n = 7.367$ MeV) it shows excellent agreement with available (γ,γ') data and in the region of the giant dipole resonance with photoabsorption experiments. The shape of the angular distributions indicates a structural change of E1 strength below and above 8.2 MeV. The centroid energy and summed B(E1) strength of the PDR are extracted and amount to E_c=7.43(2) MeV and $\sum\limits_{6.2\ \mathrm{MeV}}^{8.2\ \mathrm{MeV}} \mathrm{B(E1)} = 1.54(16)\ \mathrm{e}^2\mathrm{fm}^2$, respectively. Previously unobserved strength is found in the region above neutron threshold up to 8.2 MeV.

The deduced E1 polarizability in the energy range from 5 to 19 MeV is $\alpha_D = 18.7(13)\ \mathrm{fm}^3/\mathrm{e}^2$. Averaging over all available data a highly precise value of $\alpha_D = 18.9(5)\ \mathrm{fm}^3/\mathrm{e}^2$ can be extracted. As the strong correlations predicted by microscopical models, this puts important constraints on the neutron skin thickness in ^{208}Pb and the density dependence of the symmetry energy.

The fine structure of the giant dipole resonance was analyzed with wavelet methods. Characteristic scales at E = 100 keV, 340 keV, 520 keV, 1 MeV, and 2.1 MeV can be found. A comparison with microscopic calculations including the coupling to $2p-2h$ states suggests Landau damping as the dominant mechanism contributing to the decay width.

Level densities of 1^- states were extracted with a fluctuation analysis in the giant dipole resonance region. All phenomenological and microscopic models fail to describe the level densities in ^{208}Pb, except for a version of the back-shifted Fermi gas model allowing for additional phenomenological parameters in local mass regions.

Table of contents

List of Figures

List of Tables

1 Introduction

Electric and magnetic resonances in nuclei allow studies of the complexity of collective phenomena that take place in many-body fermionic quantum systems. In nuclei these excitations can be classified according to their angular momentum (ΔL), spin (ΔS) and isospin (ΔT) transfer. Monopole ($\Delta L = 0$), dipole ($\Delta L = 1$), quadrupole ($\Delta L = 2$) modes show a compact structure, while resonances with higher ΔL are damped over large energy regions [1, 2]. *Isoscalar* ($\Delta T = 0$) modes are vibrations in which neutrons and protons move in phase. Modes in which neutrons and protons oscillate out of phase are called *isovector* ($\Delta T = 1$). Similar oscillations may take place in spin space. Nucleons with spin up and spin down can move either in phase ($\Delta S = 0$ modes) or out of phase ($\Delta S = 1$ modes). The latter class is referred to as *spinflip* transitions or spin excitations.

The investigation of the electric dipole response has been a major field of nuclear structure research in recent years. One can schematically divide such excitations into three groups indicated in Fig. 1.1. They correspond to the giant dipole resonance (GDR), the pygmy dipole resonance (PDR) and the low-energy heterogeneous two-phonon excitation of the type $[2^+ \otimes 3^-]_{1^-}$. The first experimental finding of a large photon absorption cross section with resonance-like structure in some nuclei was by Bothe and Gentner [3] and afterwards confirmed in uranium nuclei by Baldwin and Klaiber [4]. A first interpretation was given by Goldhaber and Teller [5] and Steinwedel and Jensen [6] within the macroscopic hydrodynamical model, which treats protons and neutrons as fluids, oscillating relative to each other. This mode was identified as an isovector giant dipole resonance (IVGDR or GDR), characterized by the multipolarity, spin and isospin quantum numbers $L = 1$, $S = 0$, and $T = 1$, respectively. It is situated at energies between 10 and 20 MeV and forms a broad structure. Owed to the repulsive nature of the particle-hole (p-h) interaction [7], the major part of the total E1 strength is concentrated at high excitati-

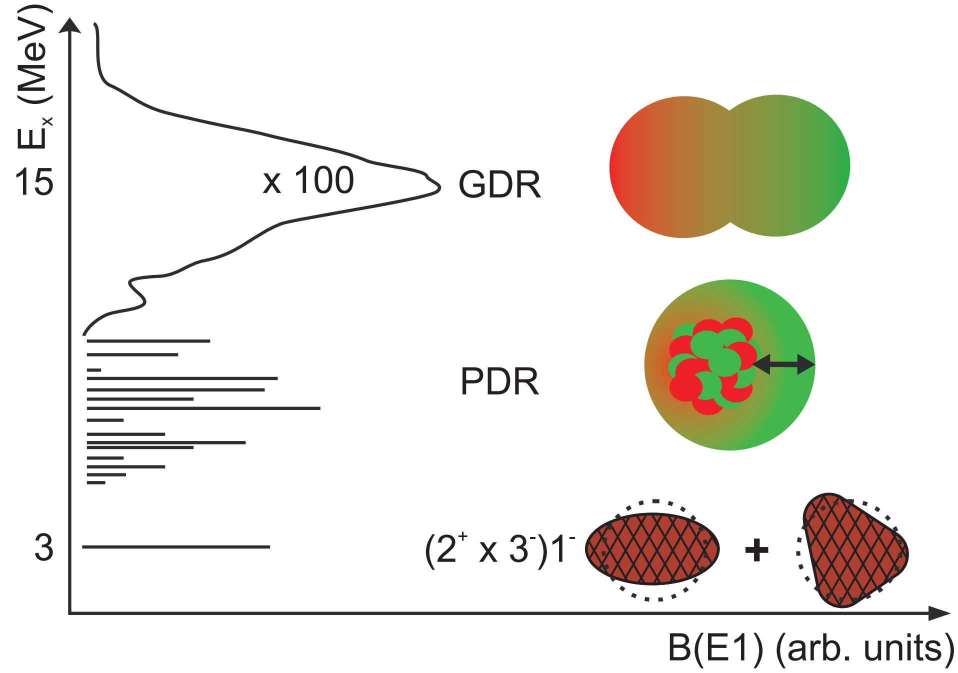

Fig. 1.1: Schematic overview of the B(E1) strength distribution in nuclei.

on energies. The centroid of the excitation strength of such oscillations is formed at an energy approximately [1]

$$E_x = 31.2 \cdot A^{-1/3} + 20.6 \cdot A^{-1/6}. \tag{1.1}$$

The experimentally observed dipole strength of the GDR exhausts the expected total dipole strength, which can be estimated with the help of the Thomas-Reiche-Kuhn energy-weighted sum rule (EWSR), giving the total integrated cross section for electric dipole photon absorption in the absence of exchange forces as

$$\mathrm{EWSR} \;=\; 60\,\frac{NZ}{A}\;\mathrm{mb\,MeV}. \tag{1.2}$$

Here N, Z and A denote neutron, charge and mass numbers of the nucleus, respectively.

At low excitation energies in spherical nuclei one observes a strong isolated electric dipole excitation which is interpreted as a member of a quintuplet of states ($J^\pi = 1^-, ..., 5^-$) originating from the coupling of the first 2^+ and 3^- phonons [8,9]. Here, the term phonon describes low-energy collective surface vibrations of the nucleus. The two-phonon character of these states can be proved unambiguously by investigating their excitation and decay behavior [10].

Low-energy electric-dipole resonances, so-called pygmy dipole resonances (PDRs), are a topic of high current interest, caused by significant experimental progress in studies of its properties in stable as well as exotic, neutron-rich nuclei. These resonances are assumed to result from oscillations of the excess neutrons against an stable proton−neutron core with $\mathrm{N} \simeq \mathrm{Z}$. In stable nuclei these excitations have been known for a long time [11], but their nature and systematic features remained poorly understood. It, certainly, is an interesting question whether the low-lying $E1$ strength in nuclei close to the valley of stability, although less pronounced, is generated by the same mechanisms or if the structural features change for extreme neutron-to-proton ratios.

One of the possible methods to study the PDR is nuclear resonance fluorescence (NRF) [12]. Recent experimental progress has been achieved by detailed measurements of low-lying $E1$ strength and its fine structure at $Z = 20$ [13] and $N = 82$ [14, 15] shell closures, performed at the S-DALINAC in Darmstadt using the high-intensity photon scattering setup [16]. Successful investigation of the dipole strength in the Mo isotopic chain [17, 18] and in other nuclei around the $\mathrm{N} = 50$ shell closure (see e.g. [19]) was performed at the ELBE photon-scattering facility [20] in Dresden-Rossendorf. In particular, the tin isotope chain is lately in the focus of investigations as it provides a high number of stable isotopes. NRF measurements of stable tin isotopes have been done for ^{116,124}Sn in Gent [21] and for ^{112,120}Sn at the S-DALINAC in Darmstadt [22]. Furthermore, E1 strength distributions below the GDR of the unstable neutron-rich nuclei $^{129-132}$Sn have been measured at GSI using Coulomb excitation with highly relativistic radioactive beams in inverse kinematics [23, 24].

Studies of the nucleus ^{208}Pb are of special importance since it is the heaviest stable nucleus with doubly-closed shell structure. In the 1970's a number of experiments dealing with the investigation of gamma transitions in lead have been carried out [25, 26, 27]. However, either they had a small end-point energy, not sufficient to cover the whole excitation energy range of interest, or a limited sensitivity to weak transitions needed for such kind of studies. Thus, the aim of the (γ,γ') experiments performed recently [28, 29, 30, 31] was to study transitions with higher sensitivity and to cover the energy range near and if possible above the particle emission threshold. These experiments provide consistent data but only roughly up to the neutron separation energy. The knowledge of the complete dipole strength is desirable for the test of theoretical predictions, since ^{208}Pb serves as a reference case for a variety of microscopic models.

The neutron distribution in ^{208}Pb and its root mean square (rms) radius in particular, is attracting significant interest both in experiment and theory. The neutron skin thickness, that is the neutron-proton rms radius difference

$$r_{skin} \equiv \Delta r_{np} = \left\langle r^2 \right\rangle_n^{1/2} - \left\langle r^2 \right\rangle_p^{1/2}, \tag{1.3}$$

of nuclei is closely connected to the density dependence of the nuclear symmetry energy and with the equation of state (EoS) of neutron-rich matter [32]. In various models, r_{skin} of ^{208}Pb displays a nearly linear correlation with the slope of the EoS of neutron matter [33], i.e. the density derivative of the symmetry energy [34], and with the surface symmetry energy of the finite nucleus [35]. A sophisticated measurement attempting to determine this quantity in ^{208}Pb is the PREX experiment at Jefferson Laboratory [36]. It uses the parity-violating electro-weak asymmetry in the elastic scattering of polarized electrons to determine the neutron radius of ^{208}Pb, which would allow an extraction of the neutron skin [37] with high experimental precision. Moreover, recent theoretical results in the framework of energy density functional theory (EDFT) using Skyrme-forces [38] and a relativistic mean field (RMF) approach [39] indicate that the static electric dipole nuclear polarizability α_D, which is proportional to the inverse energy weighted sum rule of the B(E1) strength, can be an appropriate observable to determine the neutron skin in ^{208}Pb. Both models predict a linear correlation between the polarizability and the neutron skin. They differ, however in their predictions of a similar correlation between PDR strength and neutron skin, which is expected to be weak in Ref. [38] and strong in Ref. [39].

A central goal of nuclear astrophysics is the description of the observed element abundances. The reaction mechanisms, exploring the stellar nucleosynthesis of heavy elements include rapid neutron capture (r-process), slow neutron capture (s-process), and photodisintegration (p- or γ-process). However, a full understanding of these processes is not yet achieved. One reason is that the astrophysical site of the rapid neutron capture process is still not completely established; another is due to the variety of required nuclear information. Neutron capture and photodisintegration reactions are described by a statistical model [40] in large-scale network calculations. Two very important quantities enter the reaction codes: the nuclear level density (NLD) and the photon strength function (PSF). The PSF carries information on different multipolarities contained, and is dominated by the GDR. However, low-lying strength concentrated close to the neutron threshold may have a large impact on the neutron-capture cross sections and consequently on the astrophysical reaction rates relevant for the r-process [41, 42, 43]. The knowledge of the γ-ray strength function is also important for the calculations of the cross sections used, e.g., in reactor physics and nuclear waste management [44]. One can express the photon strength function for different types X (electric or magnetic) and multipolarities λ of radiation [45] as

$$f^{X\lambda}(E,J) = \frac{\overline{\Gamma}_{X\lambda}(E,J)\rho(E,J)}{E^{2\lambda+1}}. \tag{1.4}$$

Here, $\rho(E,J)$ is the nuclear level density of the states with energy E and spin J, and $\overline{\Gamma}_{X\lambda}(E,J)$ is the γ-ray partial width averaged over these states. Utilizing the Axel-Brink hypothesis [46, 47] f^{XL} is dependent only on the energy of the emitted radiation and independent of any other properties of the initial and final states. Thus, decay of excited nuclei is often described within a statistical approach based on the concept of a compound nucleus [48], assuming the validity of the Axel-Brink hypothesis. In recent years the PSF has been deduced in a large number of nuclei from the γ-decay of compound nuclei formed in inelastic scattering or particle transfer reactions [49]. The extraction is based on the techniques described in [50]. The difficulties of this method lie in the assumptions made for the nuclear level densities, often adopted from model predictions, and in the normalization of the obtained data at the neutron separation energy to values extracted from other types of experiments such as photon and ion scattering.

According to the principle of the detailed balance, there is a connection between the PSF and the total photoabsorption cross section, measured in experiments with real or virtual photons

$$f^{X\lambda}(E,J) = \frac{2J_i+1}{(\pi\hbar c)^2\left(2J_f+1\right)} \cdot \frac{\overline{\sigma}^{X\lambda}_{abs}(E)}{E^{2\lambda-1}}, \tag{1.5}$$

where J_i and J_f are spins of the initial and final states, and $\overline{\sigma}^{X\lambda}_{abs}(E)$ is the photoabsorption cross section for radiation type $X\lambda$. However, the results from the different techniques often disagree. As an example, in Fig. 1.2 the photon strength function in ^{98}Mo obtained from different experiments is shown. The data from the (γ,xn) reaction are presented with crosses, full circles and diamond are the results of the (γ,γ') scattering [52, 53], empty squares show the data from the (^{3}He,^{3}He$'\gamma$) reaction [54]. The data are clearly inconsistent. The (γ,γ') reaction cross sections depend on the particle emission threshold, dropping rapidly at the neutron separation energy. The results from the photon scattering also depend on the knowledge of the branching ratios. Usually in the analysis of (γ,γ') experiments it is assumed that the ground state branching ratio is equal to unity, giving a lower limit of the photon strength function. One may correct it utilizing statistical model calculations of γ-ray cascades (see [18] and references therein) and thereby obtain an upper limit of the reaction cross sections. Other types of experiments such as (γ,xn) reactions supply information on the PSF above the separation energy only. Thus, an experiment that provides consistent information on the dipole response below and above the particle threshold provides an unique opportunity to test different approaches in the photon strength function determination.

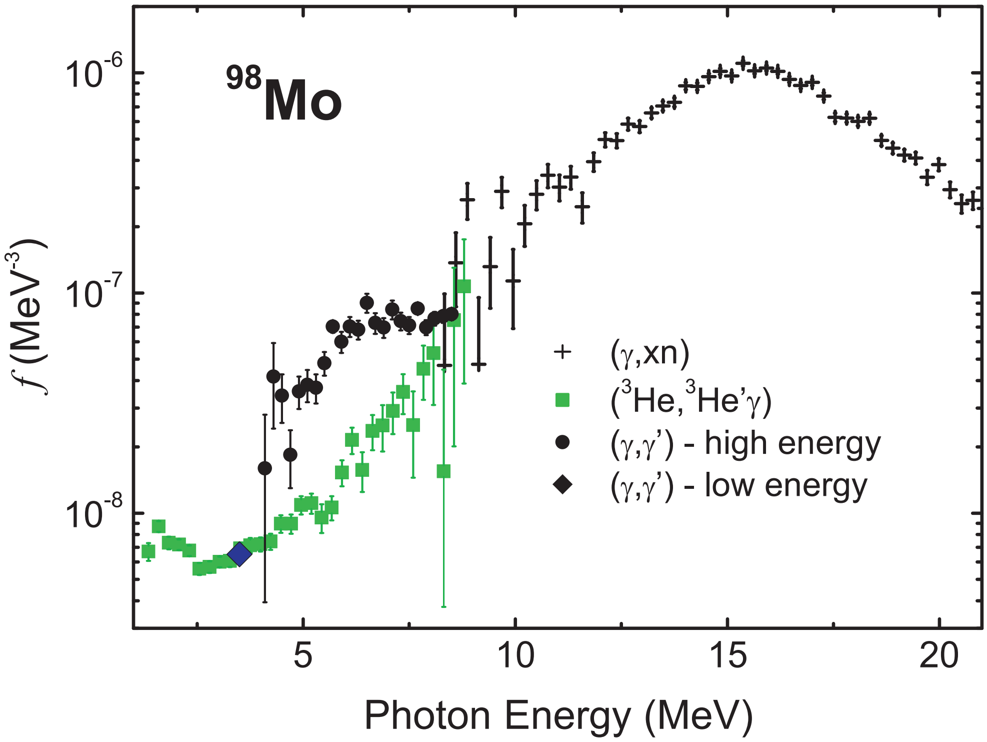

Fig. 1.2: Available data on PSF in ^{98}Mo. (γ,xn) data are taken from [51], (γ,γ') results are from [52, 53] and (^{3}He,^{3}He$'\gamma$) data are from [54]. The figure is adopted from [55].

One very promising technique to investigate dipole transition strength over a large excitation range in nuclei is Coulomb excitation in relativistic ion scattering [56], where the cross sections are related to multipole matrix elements that characterize the γ-decay of excited nuclear states. The simplest way to describe the reaction mechanism in relativistic collisions is provided by the equivalent photon method, which is originally due to Fermi [57] and later on developed by Weizsäcker [58] and Williams [59], (commonly referred as the Weizsäcker-Williams method). In the present work the Coulomb interaction between the proton beam with an energy of about 300 MeV and the ^{208}Pb target is used. In order to minimize the influence of the nuclear forces, scattering angles were limited to very forward angles including zero degree. Under these kinematic conditions the nuclear response is dominated by $\Delta L = 0$, $\Delta S = 1$, $\Delta T = 1$ transitions. Thus, such an experiment also provides information on the isovector M1 spinflip resonance. The spin magnetic dipole strength distribution is closely related to the still unsettled quenching problem of the Gamow-Teller response in nuclei (e.g. see [60] and references therein). Knowledge of spin M1 excitation strengths is particularly important for estimates of neutral-current neutrino-nucleus cross sections in supernova explosions [61] and terrestrial detection of supernova neutrinos [62], which are dominated by low-multipolarity excitations. The magnetic dipole excitation in the nucleus ^{208}Pb also has an astrophysical importance [63], because of the sizable strength near the neutron emission threshold. As advanced theoretical methods, like second RPA, can be applied, data in a doubly magic nucleus, such as ^{208}Pb, are of particular interest. The observation that the experimental spin M1 resonance strength is systematically smaller than all model predictions, called quenching, is an intriguing nuclear structure problem [64]. A concentration of 1^+ strength in ^{208}Pb was first predicted by Vergados [65] with two low-energy states at 5.45 and 7.52 MeV. The low-energy component is of dominant isoscalar nature; the high energy component is expected to be isovector and highly fragmented. The existence of the isoscalar component was first established at 5.846 MeV by a resonance fluorescence measurement with polarized photons [66] and confirmed by different (e,e′) [67] and ion scattering experiments [68, 69]. Due to the presence of many other states in the excitation energy region from 7 to 10 MeV, it has been much more difficult to localize the high energy component of the 1^+ spin excitation [70, 71]. Therefore, the assignment of the isospin character of the transitions is rather difficult [72, 73]. Proton inelastic scattering at small scattering angles has been shown to be an excellent probe for the study of both IS and IV spin-M1 transition strengths. Utilizing the experimental development of high-resolution proton scattering at forward angles at the Research Center for Nuclear Physics (RCNP) in Osaka, Japan [74], one is able to study the spin magnetic dipole strength with high precision.

Another point of interest in studies of giant resonances is the phenomenon of their fine structure, which provides an unique insight into the role of different damping mechanisms. The decay of giant resonances is a prime example of how a well-ordered collective excitation dissolves into disordered motion of internal degrees of freedom in fermionic quantum many-body systems. Indeed, damping mechanisms and corresponding lifetimes are questions of general interest in many-body physics. In quantum mechanics lifetimes are directly related to the width of the states through the energy-time uncertainty relation. Several mechanisms contribute to the total width Γ of giant resonances in nuclei [1, 75], whose full width at half maximum (FWHM) is of the order of a few MeV. First of all, a fragmentation of the collective response into a number of collective states is possible, leading to the so-called Landau damping. Another contribution results from a direct particle emission from the initial one particle–one hole ($1p-1h$) excitations, giving rise to a corresponding escape width. However, the role of the escape width should not be very important [75]. Finally the evolution of the collective modes towards compound nuclear states leads to a spreading width caused by internal mixing. An interpretation for the spreading width is given by the *doorway state model*. It is generally accepted that internal mixing occurs through a hierarchy of couplings towards more and more complex degrees of freedom in the nucleus, starting from the $2p-2h$ up to $np-nh$ states of the compound nucleus. The concept of doorway states was introduced by Block and Feshbach [76] and was later generally formulated by Feshbach [77, 78]. A schematic representation of the damping of giant resonances within a doorway picture is shown in Fig. 1.3. Initially a doorway state $|Coll\rangle$ is introduced. When coupled to more complex states, one can introduce a hierarchy of residual interactions V_1; V_2 $\cdots$ V_n. In the first step, giant resonances are assumed to decay towards $2p-2h$ states giving rise to the characteristic energy scale Γ_1. These states are themselves coupled to $3p-3h$ states. This step is reflected in the scale denoted Γ_2. The procedure can be continued down to the compound nuclear states. The scheme shown in Fig. 1.3 is rather simplified. Indeed, the interactions V_i are not unique. Therefore even at one and the same level of complexity a number of different scales may exist.

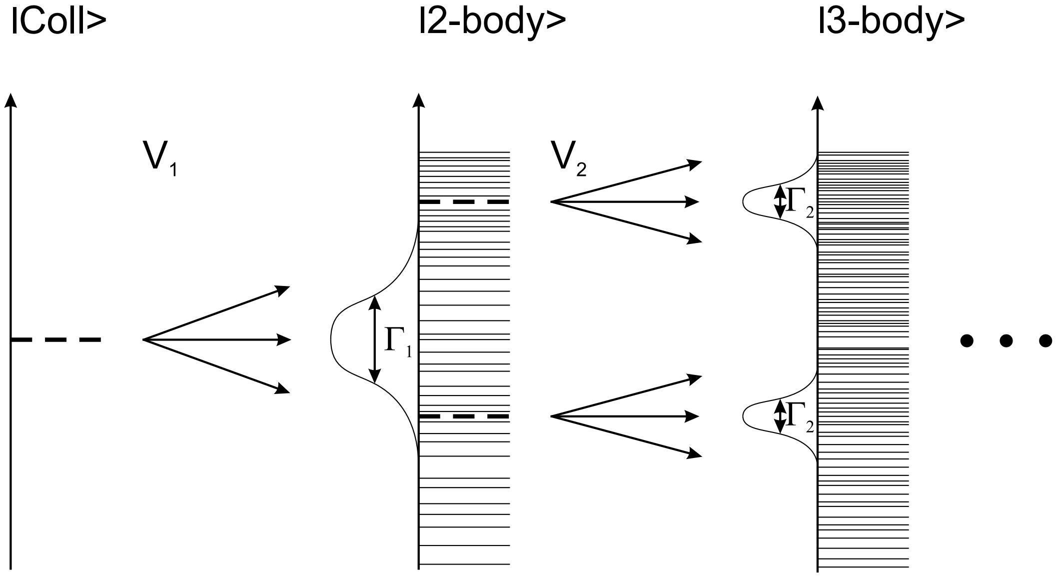

Fig. 1.3: Damping of giant resonances. A hierarchy of lifetimes and energy scales in the decay of giant resonances is expected as a result of the coupling to states with increasing complexity. Even at one and the same coupling step a number of different scales may exist. The picture is adopted from [79].

The search for experimental signatures of scales associated with the coupling between collective states and internal and external degrees of freedom is a long-standing problem. On the one hand, the spectral analysis requires high-resolution experiments. Fine structure has been observed in many types of giant resonances such as the isovector giant dipole resonance [80], the magnetic quadrupole resonance [81], the Gamow- Teller (GT) mode [82] and the isoscalar quadrupole resonance (ISGQR) [83], establishing it as a generic phenomenon in nuclei. According to the experience achieved in these studies, an energy resolution $\Delta E \leq 50$ keV (FWHM) is necessary to reveal the fine structure in heavy nuclei and to extract the scales from the data. At typical incident beam energies of a few hundred MeV per nucleon necessary for a selective direct excitation process, such a high resolution can only be achieved if dispersion matching conditions between the beam line and magnetic spectrometer are satisfied [84, 85]. Today, worldwide only a few cyclotron laboratories, such as the Research Center for Nuclear Physics (RCNP), Osaka University, Japan and iThemba LABs, Somerset West, South Africa, can provide this for proton scattering experiments. However, it should be noted that pioneering work in this field [86, 87], dealing with the fine structure of ISGQR in ^{208}Pb, was performed at the DALINAC using an (e,e′) energy-loss spectrometer [84]. On the other hand, techniques for a quantitative analysis of fine structure is needed. A variety of methods has been proposed [88] of which wavelet analysis is commonly seen as the most promising [83, 89] and will be applied to the presented data.

Another important aspect of the fine structure is its connection to nuclear level densities in the excitation energy region of giant resonances. Nuclear level densities can be determined even in the regime of not fully resolved states by means of a well established fluctuation analysis [90]. Recently, it was shown that the discrete variant of the wavelet analysis is a useful technique to determine the shape of the background [82]. In the present experiment, the extraction of level densities of 1^- states in the excitation energy region of GDR is possible and will be discussed in comparison to a variety of models.

The aim of the present thesis is a study of the complete electric and spin magnetic dipole response in ^{208}Pb. For this purpose a high-resolution polarized proton scattering experiment at very forward angles including zero degree and with an energy of about 300 MeV was carried out at the Research Center for Nuclear Physics (RCNP) at Osaka University, Japan. It will be shown that a separation of E1 and spin M1 cross sections can be achieved by two independent methods, viz. a multipole decomposition analysis of cross section angular distributions and by measurements of the polarization transfer observables.

This thesis is structured in the following way. Section 2 provides a brief background to the description of polarized proton scattering, Coulomb excitation, and modern theoretical calculations of the dipole strength and nuclear level densities. The cyclotron facility at RCNP and the experimental setup for the high resolution measurements together with technical details of the experiment carried out are described in Section 3. In the Section 4 the main steps in the data analysis and the finally obtained excitation spectra of ^{208}Pb are presented. The results of a spectra decomposition into M1/E1, respectively spinflip/non-spinflip cross sections, extraction of the B(E1) strength distribution below and above neutron separation energy, dipole polarizability and comparison with theoretical predictions are discussed in Section 5. Section 6 deals with an analysis of the fine structure of the giant dipole resonance and explains the extraction of $J^\pi = 1^-$ level densities in the resonance region. The thesis closes with a summary and outlook.

2 Theoretical background

This section covers the relevant theoretical concepts needed for the analysis of the inelastic polarized proton scattering data. This includes: the projectile-target interaction via nuclear and Coulomb forces, the description of the polarization transfer observables and an overview of the theoretical microscopic models, used to calculate the dipole strength distribution in ^{208}Pb. Additionally, level density models are described, which are compared to experimental data on $J^{\pi} = 1^{-}$ states, deduced from the fine structure of the giant dipole resonance.

2.1 Proton scattering basics

Three basic aspects of the inelastic proton scattering will be briefly discussed here: the projectile-target interaction, the description of the projectile distorted wave functions and information on effective nucleon-nucleon interaction.

As, so far, no complete view of the strong interaction has been established, the proton-nucleus scattering process has to be described using effective interactions. Here, one has to distinguish between the electromagnetic excitation by Coulomb interaction of dipole transitions, dominant at extreme forward angles, and excitations that are caused by the strong interaction, such as the spinflip excitations. In the case of electric giant resonances, which can be described macroscopically as density oscillations on the nucleus surface, the transition potential is determined as the variation of the optical potential or the Coulomb potential. The description of the spinflip cross sections is made within the context of the so-called distorted waves Born approximation (DWBA), using the effective t-Matrix interaction of Franey and Love [91, 92].

2.1.1 Inelastic scattering

In this section we follow the formalism presented in [93,94] and define the important quantities involved in the process of inelastic scattering of a proton at a nucleus. The proton-nucleus interaction in the non-relativistic case can be described with the time-independent Schrödinger equation:

$$(H_0 + V)\psi = (H_N + K_0 + V)\psi = E\psi. \tag{2.1}$$

H_N denotes the nuclear Hamiltonian, $K_0 = p_0^2/2m_p$ represents the kinetic energy of the incoming proton and V is the proton-nucleus interaction. The eigenfunctions ψ are given by the Lippman-Schwinger equation:

$$\psi^{\pm} = \phi^{\pm} + \frac{1}{E - H_0 \pm \imath\epsilon} V \psi^{\pm}. \tag{2.2}$$

Here, $\phi^{\pm}$ is the ground state eigenfunction of the unperturbed system ($V = 0$), and the + and - signs indicate incoming and outgoing waves, respectively. After the interaction V is switched on, the transition probability between perturbed/unperturbed states is given by the transition operator

$$T = V + V \frac{1}{E - H_0 \pm \imath\epsilon} T. \tag{2.3}$$

The integral representation of the operator T follows from the Eq. (2.2)

$$T = \langle \phi^{-} \mid V \mid \psi^{+} \rangle. \tag{2.4}$$

The connection between differential cross section $d\sigma/d\Omega$ and the t-matrix elements (transition amplitudes) is given by the equation

$$\frac{d\sigma}{d\Omega}(\vec{k},\vec{k}') = \left(\frac{\mu}{2\pi\hbar^2}\right)^2 \frac{|\vec{k}'|}{|\vec{k}|} \, | \, T_{fi}(\vec{k},\vec{k}') \, |^2, \tag{2.5}$$

where μ is the reduced mass, and $\vec{k}$ and $\vec{k}'$ are the momenta of the incoming and outgoing protons in the laboratory system, respectively. The equation is only valid for the case of a nucleus with $J^\pi = 0^+$ ground state.

2.1.2 Distorted waves and optical potential

The distorted wave Born approximation forms the basis of the computer code DWBA07 [95] used for the calculation of the transition amplitudes. In this approach, the scattering matrix T_{fi} is expanded in a basis of distorted wave functions χ defined by the Lippman-Schwinger equation (2.2)

$$\chi^\pm = \phi^\pm + \frac{1}{E - H_0 \pm i\epsilon} V_0 \chi^\pm, \tag{2.6}$$

where $V_0 = V_0(\vec{r} - \vec{r}_N)$ describes the interaction between projectile and nucleus in the incoming channel. A local representation of the potential, the optical potential $U_0(\vec{r})$, can be obtained by folding the interaction with the ground state density $\rho_0(\vec{r}_N)$ of the nucleus

$$U_0(\vec{r}) = \int \rho_0(\vec{r}_N) V_0(\vec{r} - \vec{r}_N) d^3 r_N. \tag{2.7}$$

An alternative approach is the use of a phenomenological optical potential, which is usually determined by a fit to elastic scattering data. The optical potential consists of a real and imaginary part with a central and a spin-orbit term. The parametrization of the potential in the non-relativistic case has the standard form

$$U(\vec{r}) = V_{coul}(r) + V_0 f(x_0) + iW_0 f(x_0) - 2(V_{so} + iW_{so}) \frac{1}{r}\frac{d}{dr} f(x_{so}) \vec{L} \cdot \vec{\sigma}, \tag{2.8}$$

with

$$f(x_i) = \frac{1}{1 + e^{x_i}} \text{ and } x_i = \frac{(r - r_i A^{1/3})}{a_i}, \quad (i = 0, so).$$

Here $V_{coul}(r)$ is the Coulomb potential, V_0 and W_0 are the depths of the spin-independent central term and V_{so} and W_{so} are those of the spin-orbit potential. For charged-particle scattering the Coulomb potential V_{coul} is additionally taken into account. The radial dependence is described by Woods-Saxon functions $f(x_i)$ with a radius r_i and a surface diffuseness a_i. All parameters are determined by a fit to elastic scattering data.

2.1.3 Effective interaction

The proton-nucleus interaction can be described as the sum of the two-particle interactions v_n between the projectile and the individual nucleons in the nucleus

$$V = \sum_{n=1}^{A} v_n. \tag{2.9}$$

In first Born approximation the transition amplitudes T_{fi} can be expressed in the distorted basis χ given in Eq. (2.6) as a sum of nucleon-nucleon scattering amplitudes

$$T_{fi} \simeq \langle \chi_f^- \mid \sum_{n=1}^{A} v_n \mid \chi_i^+ \rangle \simeq \langle \chi_f^- \mid \sum_{n=1}^{A} t_n \mid \chi_i^+ \rangle. \tag{2.10}$$

In the Distorted Wave Impulse Approximation (DWIA) the potential energy of the target nucleons is neglected. The two-particle interaction t_n is obtained from a kinematic transformation of the free-nucleon scattering transition matrix. For beam energies E_0 >150 MeV, the DWIA provides a good approximation. For some excitations, effects from Pauli blocking of forbidden intermediate states play a role, even at beam energies larger than 150 MeV. One of the possible ways to take this into account is to use Brueckner's g-matrix which is defined by the Bethe-Goldstone equation.

$$G = V + V \frac{Q}{E - H_1 + i\epsilon} G, \tag{2.11}$$

where Q represents the Pauli exclusion operator to block forbidden intermediate states, H_1 is a Hamiltonian that provides the energy between two nucleons in the nuclear mean field. Love and Franey [91] derived for beam energies of 100-800 MeV a phenomenological description of the free nucleon-nucleon t-matrix. Parametrizations starting from the g-matrix were developed e.g. using Paris- or Bonn-NN potentials by von Geramb [96] or Karataglidis *et al.* [97], respectively. These are different approaches to approximate the nonlocal scattering matrix using local operators. As local representation of the nucleon-nucleon interaction the following form is chosen

$$v(\vec{r}, \vec{p}) = v^C(r) + v^{LS}(r)\vec{L} \cdot \vec{S} + v^T(r) S_{12}, \tag{2.12}$$

which includes a central part $v^C(r)$, a spin-orbit $v^{LS}(r)$ and a $v^T(r)$ tensor term, where

$\vec{L}$ - relative angular momentum,
$\vec{S}$ - relative spin, $\vec{S} = \vec{\sigma}_1 + \vec{\sigma}_2$,
$\vec{L} \cdot \vec{S}$ - spin-orbit operator,
S_{12} - tensor operator $S_{12} = 3(\vec{\sigma}_1 \cdot \hat{r})(\vec{\sigma}_2 \cdot \hat{r}) - \vec{\sigma}_1 \cdot \vec{\sigma}_2$, $\hat{r} = \vec{r}/\mid \vec{r} \mid$,
$\vec{\sigma}_i$ - Pauli spin matrices, and
$\vec{r}$ - relative distance.

The radial dependence of the complex amplitudes $v^C(r)$ and $v^{LS}(r)$ is approximated by a sum of Yukawa potentials $Y(x)$

$$v^j(r) = \sum_{i=1}^{N_j} v_i^j Y(r/R_i), \tag{2.13}$$

with $j = C$ or LS, $Y(x) = e^{-x}/x$, and $x = r/R_i$. The radial dependence of the tensor term is described as

$$v^T(r) = \sum_{i=1}^{N_T} v_i^T r^2 Y(r/R_i). \tag{2.14}$$

The constituents of Eqs. (2.13) and (2.14) differ in their strengths v_i^m ($m = j$ or T) and ranges R_i. In the limit of momentum transfer $q \to 0$, spin-orbital and tensor parts of the interaction are small compared to the central term. In such a case the effective interaction can be expanded in terms according to their spin-isospin transfer properties

$$v(\vec{r},\vec{p}) = v_0^C(r) + v_\sigma^C(r)\vec{\sigma}_1 \cdot \vec{\sigma}_2 + v_\tau^C(r)\vec{\tau}_1 \cdot \vec{\tau}_2 + v_{\sigma\tau}^C(r)\vec{\sigma}_1 \cdot \vec{\sigma}_2\vec{\tau}_1 \cdot \vec{\tau}_2. \tag{2.15}$$

The isospin operator $\vec{\tau}_1 \cdot \vec{\tau}_2$ causes the isospinflip transitions. Spinflip transitions are induced via $\vec{\sigma}_1 \cdot \vec{\sigma}_2$ operators. The energy dependence of the free nucleon-nucleon interaction for momentum transfer $q \to 0$ is presented in Fig. 2.1. The dominant term of the central interaction $V_0^C(r)$ is the isoscalar spin-independent part. Spin- and/or isospin exchange between projectile and target nucleus are described by the $V_{\sigma\tau}^C(r)$ isovector spin-dependent term, the isovector spin-independent part $V_\tau^C(r)$ and isoscalar spin-dependent term $V_\sigma^C(r)$, respectively. Incident energies of E_0 = 200 - 300 MeV and vanishing momentum transfer are favorable conditions to study isovector spinflip transitions with $\Delta L = 0$, $\Delta S = 1$, $\Delta T = 1$ (i.e. the spin M1 resonance), because the ratio $V_{\sigma\tau}^C/V_\tau^C$ has a maximum, while the dominating term V_0^C has a minimum.

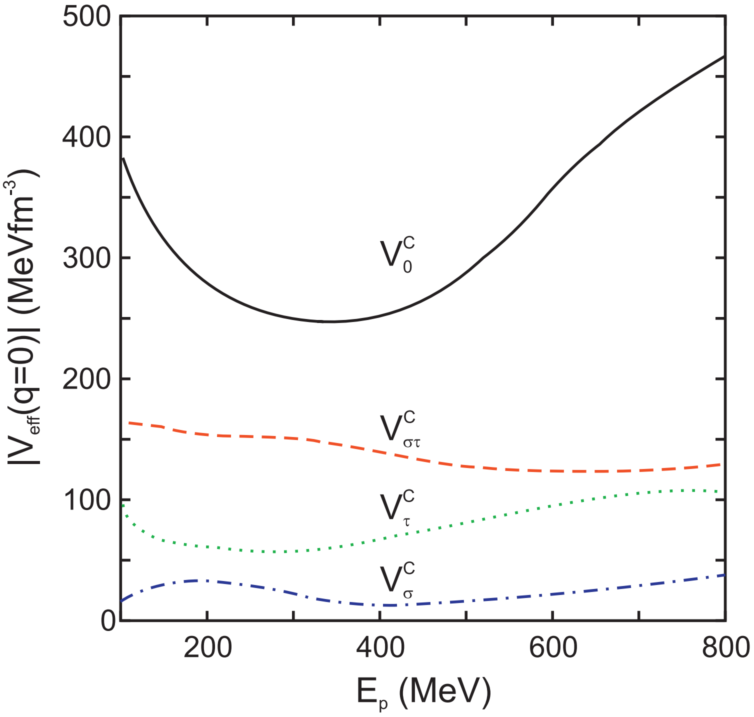

Fig. 2.1: Energy dependence of the central terms of the free nucleon-nucleon interaction from Love and Franey [92] for vanishing momentum transfer.

2.2 Coulomb excitation

Coulomb excitation describes the excitation of a target nucleus in the electromagnetic field of a projectile, or vice versa. At large impact parameters $b > r_{Coul}$, with $r_{Coul} = R_t + R_p$ being the sum of target and projectile radii, respectively, corresponding to small scattering angles, the nuclear excitation cross sections are small in comparison with those due to Coulomb interaction. In such a case, the excitation cross section can be expressed in terms of multipole matrix elements describing the electromagnetic field. Therefore, a determination of the Coulomb excitation cross section leads directly to basic nuclear structure information. The Coulomb excitation process, as outlined below, is well understood, and results are largely model independent. A full description of the method can be found in Refs. [98, 99].

2.2.1 Classical approach

In the semiclassical treatment of the Coulomb excitation process, the projectile is considered as a point-like charge moving along a hyperbolic orbit in the repulsive Coulomb field of a target nucleus. The motion of the projectile along the orbit is illustrated in Fig. 2.2. At low energies those are Rutherford trajectories for the relative motion, while at high energies one assumes an undisturbed straight-line motion. For the relativistic case, the projectile deflection angle in the laboratory reference frame is given by

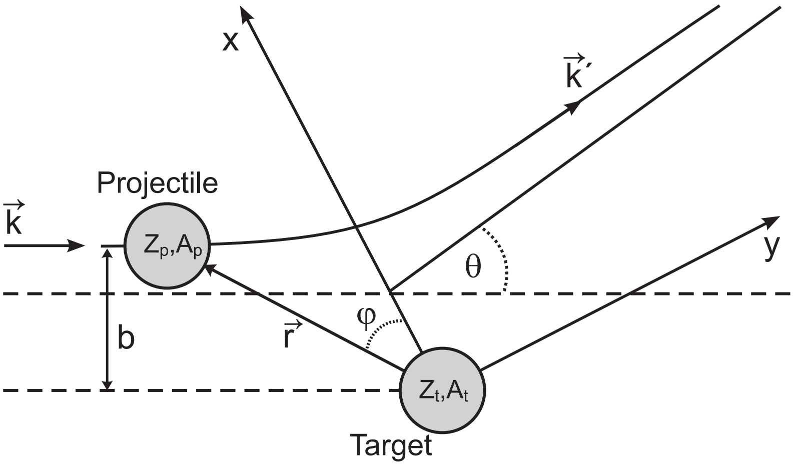

Fig. 2.2: Classical picture of the projectile trajectory in the nucleus-nucleus scattering. The position and the momentum of the projectile are denoted by φ, $\vec{r}$ and $\vec{k}$, respectively, the deflection angle by θ. The charge and mass numbers of the projectile and target are represented by Z_p, A_p, Z_t, and A_t, respectively.

$$\theta_{lab} = \frac{2Z_p Z_t e^2}{\gamma m_p v_p^2} \cdot \frac{1}{b}, \tag{2.16}$$

where v_p is the velocity of the projectile and γ denotes its Lorentz factor. The straight-line motion is characterized by an impact parameter b given by the distance of closest approach at the nuclear interaction radius.

In the following excitation of the target nucleus is considered. However, the excitation of the projectile is entirely analogous to the excitation of the target apart from the magnitudes of the exciting fields, which are proportional to Z_t and Z_p, respectively. Since recoil effects on the trajectory are neglected in the description of relativistic Coulomb excitation, the nuclear center of mass may be taken as the origin of the coordinate system. Furthermore, the energy loss of the projectile is small compared to the bombarding energy, thus the effect of the excitation on the particle motion can be neglected. In such a treatment, the nuclear excitation is a result of the time-dependent electromagnetic field generated by the projectile acting on the target nucleus. If the effect of this field is small, it may be treated by first-order quantum-mechanical perturbation theory. The differential elastic scattering cross section is given by the Rutherford formula

$$\frac{d\sigma}{d\Omega_R} = \frac{1}{4}a^2\frac{1}{\sin^4\left(\frac{\theta}{2}\right)}, \qquad \text{with } a = \frac{1}{4\pi\epsilon_0}\frac{Z_pZ_te^2}{4E}, \tag{2.17}$$

where θ is the scattering angle in the center-of-mass system. Since it has been assumed that the orbit of the particle is not affected by the excitation, the differential excitation cross section is given by

$$\frac{d\sigma}{d\Omega} = \frac{d\sigma}{d\Omega_R}P_{i\to f}, \tag{2.18}$$

where $P_{i\to f}$ is the excitation probability from an initial state $|i\rangle$ to a final state $|f\rangle$. Within perturbation theory one can evaluate $P_{i\to f}$ as

$$P_{i\to f} = \frac{1}{(2I_i+1)}\sum_{M_iM_f}|S_{i\to f}|^2. \tag{2.19}$$

Here I_i denotes the spin of the initial state, and M_i, M_f are the magnetic quantum numbers of the initial and final states, respectively. The excitation amplitude can be expressed as

$$S_{i\to f} = \frac{1}{i\hbar}\int\limits_{-\infty}^{\infty} dt e^{i\omega t}\langle f|V(r(t))|i\rangle, \tag{2.20}$$

where $\omega = (E_i - E_f)/\hbar$. The excitation cross section can be obtained by integrating the excitation probability from a minimum impact parameter b_{min}, determined by the experimental conditions (e.g. a maximum scattering angle), to infinity. An approximate result is obtained by expressing the excitation amplitude as a product of two factors

$$S_{i\to f} = i\sum_{\lambda}\chi_{i\to f}f_\lambda(\xi). \tag{2.21}$$

The parameter χ is a measure of the strength of the interaction, the λ is a multipolarity of a transition, and the function $f(\xi)$ measures the degree of adiabaticity of the process in terms of the parameter $\xi = \omega R/\gamma v$. The parameter R is equal to the sum of the two nuclear radii. The total cross section is then given by

$$\sigma = 2\pi\int\limits_{b_{min}}^{\infty} P_{i\to f}b\,\mathrm{d}b \approx 2\pi\int\limits_{b_{min}}^{b_{max}} |\chi|^2 b\,\mathrm{d}b, \tag{2.22}$$

where $b_{max} = \gamma v/\omega$. This leads to an approximate expression for the excitation cross section as function of parity π and multipolarity λ

$$\sigma_{\pi\lambda} \approx \left(\frac{Z_te^2}{\hbar c}\right)^2\frac{B(\pi\lambda, 0\to\lambda)}{e^2}\pi b_{min}^{2(1-\lambda)}\cdot\begin{cases}(\lambda-1)^{-1} & \text{for } \lambda\geq 2\\ 2\ln(\frac{b_{max}}{b_{min}}) & \text{for } \lambda = 1,\end{cases} \tag{2.23}$$

where $b_{max} \gg b_{min}$ was assumed. The quantity $B(\pi\lambda, 0 \rightarrow \lambda)$ is the reduced transition probability

$$B(\pi\lambda, I_i \rightarrow I_f) = \frac{1}{(2I_i+1)} \sum_{M_i M_f} |\langle I_f M_f | M_{\pi\lambda m} | I_i M_i \rangle|^2. \tag{2.24}$$

Hereof, the condition $M_{\pi lm}$ is the multipole operator for electromagnetic transitions. The exact expression for the excitation cross section, summed over parities and multipolarities is [98]

$$\sigma_{i\rightarrow f} = \left(\frac{Z_t e^2}{\hbar c}\right)^2 \sum_{\pi\lambda m} \frac{B(\pi\lambda, I_i \rightarrow I_f)}{e^2} \left| G_{\pi\lambda m}\left(\frac{c}{v}\right)\right|^2 g_m(\xi). \tag{2.25}$$

The functions $G_{\pi\lambda m}(x)$ can be introduced in terms of the Legendre polynomials and are tabulated in [56]. Functions $g_m(\xi)$ are given by

$$\begin{aligned} g_m(\xi) = g_{-m}(\xi) &= 2\pi(\omega/\gamma v)^2 \int_R^\infty K_m^2(\omega b/\gamma v) b \, \mathrm{d}b \\ &= \pi\xi^2 \left[K_{m+1}(\xi) K_{m-1}(\xi) - K_m^2(\xi)\right]. \end{aligned} \tag{2.26}$$

Here $K_m(\xi)$ are the modified Bessel's functions of m^{th} order. Equation (2.25) highlights the direct proportionality between the Coulomb excitation cross section and the reduced transition probability

$$\sigma_{i\rightarrow f} \sim B(\pi\lambda, I_i \rightarrow I_f). \tag{2.27}$$

Hence, the $B(\pi\lambda)$ values can be extracted from a cross section measurement.

2.2.2 Equivalent photon method

In principle, Coulomb excitation can be viewed as the absorption of virtual photons by the target nucleus. These virtual photons are produced by the moving projectile and the equivalent photon number (the number of real photons that would have an equivalent net effect for one particular transition) is related to the Fourier transformation of the time-dependent electromagnetic field produced by the projectile. One can express the Coulomb excitation cross section as

$$\sigma_{i\rightarrow f} = \sum_{\pi\lambda} \int N_{\pi\lambda}(E_\gamma) \sigma_\gamma^{\pi\lambda}(E_\gamma) \frac{dE_\gamma}{E_\gamma}, \tag{2.28}$$

where the spectrum of photons of multipolarity λ is determined by the equivalent photon number $N_{\pi\lambda}$ and the photoabsorption cross section is given by $\sigma_\gamma^{\pi\lambda}(E_\gamma)$ The photoabsorption cross section for real photons is given by [99]

$$\sigma_\gamma^{\pi\lambda}(E_\gamma) = \frac{(2\pi)^3 (l+1)}{l[(2l+1)!!]^2} \sum_f \rho_f(\epsilon) k^{2l-1} B(\pi\lambda). \tag{2.29}$$

The quantity $\rho_f(\epsilon)$ represents the density of the final states in the target with energy $E_f = E_i + \epsilon$ and $k = \omega/c$. This allows to obtain equivalent photon numbers $N_{\pi\lambda}(E_\gamma)$. Inserting Eq. (2.29) into Eq. (2.28) and comparing to Eq. (2.25) results in

$$N_{\pi\lambda}(E_\gamma) = Z_p^2 \alpha \frac{l[(2l+1)!!]^2}{(2\pi)^3(l+1)} \sum_m \left| G_{\pi\lambda m}\left(\frac{c}{v}\right)\right|^2 g_m(\xi). \tag{2.30}$$

Here, Z_p is the projectile charge number, v its velocity and $\alpha = e^2/\hbar c$ is the fine structure constant. The double differential cross section can be expressed in the terms of equivalent photon numbers as

$$\frac{d^2\sigma}{d\Omega dE_\gamma} = \frac{1}{E_\gamma}\sum_{\pi\lambda}\frac{dN_{\pi\lambda}}{d\Omega}\sigma_\gamma^{\pi\lambda}. \tag{2.31}$$

Using tabulated $G_{\pi\lambda m}$ and g_m functions from the textbook of Alder and Winther for E1 multipolarities [56], one can obtain equivalent photon numbers per unit solid angle for relativistic projectile energies

$$\left(\frac{dN_{E1}}{d\Omega}\right)_{rel} = \frac{Z_p^2\alpha}{4\pi^2}\zeta^2\varepsilon^4\left(\frac{1}{\gamma\beta}\right)^2\left[K_1^2(x) + \frac{1}{\gamma^2}K_0^2(x)\right]. \tag{2.32}$$

The adiabaticity parameter can be written as $\zeta = \omega a/v$, where $a = Z_p Z_t e^2/\mu v^2$ corresponds to half the distance of closest approach in a head-on collision. The reduced mass is denoted as μ, $\varepsilon = \sin^{-1}(\theta/2)$ is the eccentricity parameter, the parameter β represents the velocity of the projectile in terms of the speed of light, and the K's are modified Bessel functions of the argument $x = (\varepsilon\zeta/\gamma)\cos(\theta/2)$. In the nonrelativistic limit a small scattering angle is related to a large impact parameter $\varepsilon \gg 1$. Thus, the corresponding value can be written as

$$\left(\frac{dN_{E1}}{d\Omega}\right)_{nonrel} = \frac{Z_p^2\alpha}{4\pi^2}\epsilon^2\left(\frac{1}{\beta}\right)^2\left[x^2[K_1^2(x) + K_0^2(x)\right]. \tag{2.33}$$

For other multipolarities it is not possible to derive analytical expression for the equivalent photon numbers in the non-relativistic case. However, in relativistic kinematics one can derive approximate expressions for M1 and E2 excitations for the angular distributions leading to

$$\begin{aligned}\frac{dN_{E2}}{d\Omega} &= \frac{Z_p^2\alpha}{4\pi^2}\left(\frac{1}{\beta}\right)^4\varepsilon^2 e^{-\pi\zeta/\gamma}\left\{\frac{4}{\gamma^2}\left[K_1^2 + xK_0K_1 + x^2K_0^2\right] + x^2\left(2-\beta^2\right)^2K_1^2\right\},\\ \frac{dN_{M1}}{d\Omega} &= \frac{Z_p^2\alpha}{4\pi^2}\left(\frac{\zeta}{\gamma}\right)^2\varepsilon^4 e^{-\pi\zeta/\gamma}K_1^2,\end{aligned} \tag{2.34}$$

where all K's are functions of $x = \varepsilon\zeta/\gamma$. In this work the intensity spectra of E1, M1 and E2 virtual photons are generated by inelastic proton scattering on ^{208}Pb at the incident beam energy of 295 MeV. They are illustrated in Fig. 2.3. Since the number of equivalent photons can be determined, the photoabsorption cross section can be related to the Coulomb excitation cross section and vice versa. For example, this relation is used to derive astrophysically important photodissociation cross sections from Coulomb excitation results (see e.g. [99]).

2.3 Polarization transfer

In the present study, it is crucial to separate spinflip M1 strength from the E1 strength since both are excited in proton inelastic scattering at extreme forward angles. Measurements using polarized beams provide a tool to determine the angular momentum character of a transition. The following section briefly presents the formalism and conventions of polarization transfer measurements. Detailed presentations can be found in [100, 101]. The description of reactions of the type $\vec{\frac{1}{2}} + A \to \vec{\frac{1}{2}} + B$, where $\vec{\frac{1}{2}}$ represents a polarized spin-$\frac{1}{2}$ particle is discussed within the plane wave impulse approximation (PWIA). Some arguments about symmetries are given to

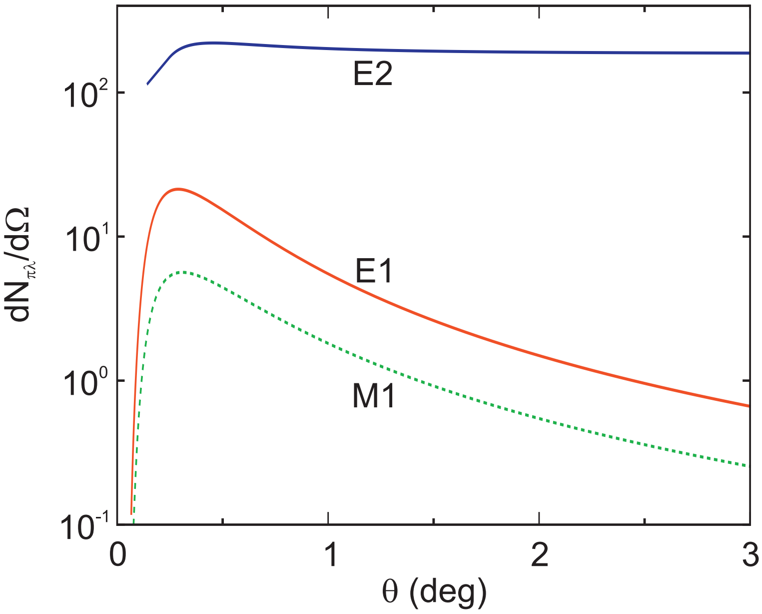

Fig. 2.3: Virtual photon numbers per unit solid angle for E1, M1 and E2 transitions in Coulomb excitation induced by 295 MeV protons on ^{208}Pb at E_γ =3 MeV calculated using Eqs. (2.32) and (2.34).

limit the number of experimental observables. In the PWIA framework the t-matrix for nucleon-nucleus scattering is given by

$$T = \left\langle f \left| M_{NN} e^{-i\vec{q}\cdot\vec{r}} \right| i \right\rangle . \tag{2.35}$$

The analyzing power for the j^{th} component of the beam polarization vector A_j, the cross section σ and the polarization transfer coefficients (PTC) D_{ij} depend on the t-matrix in the following way [102, 103]

$$A_j = \frac{\mathrm{Tr}(TT^\dagger\sigma_n)}{\mathrm{Tr}(TT^\dagger)}, \qquad \frac{\mathrm{d}\sigma}{\mathrm{d}\Omega} = \frac{1}{2}\mathrm{Tr}(TT^\dagger), \qquad D_{ij} = \frac{\mathrm{Tr}(T\sigma_j T^\dagger \sigma_i)}{\mathrm{Tr}(TT^\dagger)}, \tag{2.36}$$

where the index $i(j)$ refers to the direction of the projectile spin in the initial(final) state. The nucleon-nucleon scattering amplitude, M_{NN}, can be phenomenologically expressed as an operator in the spin space of the pair of the interacting nucleons [104]

$$M_{NN} = A + B\sigma_{1\hat{n}}\sigma_{2\hat{n}} + C\left(\sigma_{1\hat{n}} + \sigma_{2\hat{n}}\right) + E\sigma_{1\hat{q}}\sigma_{2\hat{q}} + F\sigma_{1\hat{p}}\sigma_{2\hat{p}}. \tag{2.37}$$

The indices $\hat{n}$, $\hat{p}$ and $\hat{q}$ denote unit vectors of the coordinate system, defined as

$$\hat{n} = \frac{\vec{n}}{|\vec{n}|}, \qquad \vec{n} = \vec{k}' \times \vec{k}, \tag{2.38}$$

$$\hat{q} = \frac{\vec{q}}{|\vec{q}|}, \qquad \vec{q} = \vec{k}' - \vec{k}, \tag{2.39}$$

$$\hat{p} = \hat{q} \times \hat{n}, \tag{2.40}$$

with initial $\vec{k}$ and final $\vec{k}'$ momentum vectors. Each of the amplitude coefficients consists of isoscalar and isovector terms: $A = A_{IS} + A_{IV}\vec{\tau}_1 \cdot \vec{\tau}_2$, etc. Thus Eq. (2.37) can be rewritten as

$$M_{NN} = A + \frac{1}{3}(B+E+F)\vec{\sigma}_1\cdot\vec{\sigma}_2 + C(\sigma_1+\sigma_2)\cdot\hat{n} + \frac{1}{3}(E-B)S_{12}(\hat{q}) + \frac{1}{3}(F-B)S_{12}(\hat{p}). \tag{2.41}$$

$S_{12}(\hat{q})$ is a tensor operator defined by

$$S_{12}(\hat{q}) = \frac{3(\vec{\sigma}_1 \cdot \vec{r})(\vec{\sigma}_2 \cdot \vec{r})}{r^2} - \vec{\sigma}_1 \cdot \vec{\sigma}_2. \tag{2.42}$$

The components of Eq. (2.41) correspond to the central spin-independent, central spin-dependent, spin-orbit, direct tensor, and exchange tensor terms of the effective interaction, respectively. However, the spin-orbit (C) and direct tensor $(E - B)$ components vanish in the case of 0° scattering. Furthermore, the central spin-independent term (A) vanishes for spinflip transitions [105]. Thus, the PTC can be rewritten as

$$D_{SL} = D_{LS} = 0, \tag{2.43}$$

$$D_{SS} = D_{NN} = \frac{\left(|B_i|^2 - |F_i|^2\right) X_T^2 - |B_i|^2 X_L^2}{\left(|B_i|^2 + |F_i|^2\right) X_T^2 + |B_i|^2 X_L^2}, \tag{2.44}$$

$$D_{LL} = \frac{\left(-3|B_i|^2 + |F_i|^2\right) X_T^2 + |B_i|^2 X_L^2}{\left(|B_i|^2 + |F_i|^2\right) X_T^2 + |B_i|^2 X_L^2}. \tag{2.45}$$

The indices L (longitudinal), N (normal) and S sideways correspond to the axes $\hat{l}$, $\hat{n}$ and $\hat{s}$ in the projectile helicity frame. As illustrated in Fig. 2.4, they are parallel to $\vec{k}$, $\vec{k} \times \vec{k}'$, and $\vec{k} \times (\vec{k} \times \vec{k}')$. Due to rotational symmetry at 0° the polarization transfer observable D_{NN} is equal to D_{SS}.

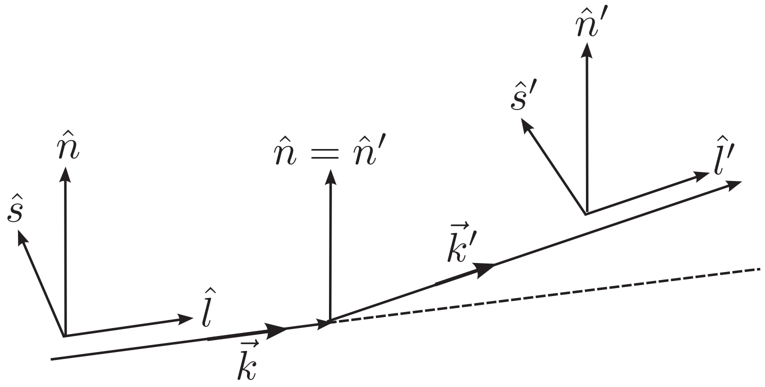

Fig. 2.4: Coordinate system for polarization measurements.The l axis is aligned in the beam direction, the n axis is along the normal to the plane formed by $\vec{k}$ and $\vec{k}'$, and the s axis completes the right-handed coordinate system.

The quantities X_T and X_L represent the spin-transverse and spin-longitudinal form factors. At forward angles, for which the spin-orbit part is negligible, the sum of the diagonal elements is equal to -1 for spinflip transitions and equal to 3 for non-spinflip transitions [106]. Exploiting these relations Sakai et.al. [107] suggested a new quantity, viz. the total spin transfer

$$\Sigma = \frac{3 - (D_{SS} + D_{NN} + D_{LL})}{4}, \tag{2.46}$$

which in the specific case 0° simplifies to

$$\Sigma = \frac{3 - (2D_{NN} + D_{LL})}{4}. \tag{2.47}$$

At forward angles $\left(\vec{l} \approx \vec{l}'\right)$ it takes a discrete value of 1 for spinflip or 0 for non-spinflip transitions. Therefore, from polarization transfer measurements the spinflip and non-spinflip cross sections parts at 0° can be decomposed

$$\frac{d\sigma}{d\Omega}(\Delta S = 1) \equiv \Sigma \cdot \frac{d\sigma}{d\Omega}, \tag{2.48}$$

$$\frac{d\sigma}{d\Omega}(\Delta S = 0) \equiv (1 - \Sigma) \cdot \frac{d\sigma}{d\Omega}. \tag{2.49}$$

Due to the different excitation mechanisms discussed above, non-spinflip cross sections can be identified with E1 excitations, and spinflip cross sections with M1 excitations, respectively. A successful application of this technique has been demonstrated for ^{12}C and ^{16}O in Refs. [108, 109].

2.4 Microscopic models for the calculation of dipole strength distributions

To extract quantitative information on the structure of the dipole strength in ^{208}Pb extracted from the experimental data, theoretical calculations using the quasiparticle-phonon model (QPM) and the relativistic quasiparticle time blocking approximation (RQTBA) were performed.

2.4.1 Quasiparticle-phonon model

In order to reveal the physical nature of the giant resonances one needs theoretical predictions obtained in the framework of models which consider couplings to complex degrees of freedom. In this work the quasiparticle-phonon model (QPM) [110, 111] is used. In the past this model has proven itself to be highly successful in describing collective modes in heavy nuclei [29, 112]. Within this model $1p-1h$ excitations are projected on a space of one-phonon states, whose properties (excitation energies and internal fermionic structure) are obtained from solving quasiparticle-RPA equations [110]. When the phonon basis is constructed, the wave function of excited states are written as a combination of interacting one- and multi-phonon configurations (see, e.g., [113]). The latter are obtained by coupling one-phonon configurations. In realistic calculations the QPM requires a basis truncation. This reduction is performed following two main principles. First, very complex N-phonon configurations are neglected. In practice, the most complex configurations included in the wave function of low-lying states are of 3-phonon nature. Secondly, only configurations with an excitation energy below an arbitrary threshold are accounted for. In fact, these truncation principles are physically motivated. The density of complex configurations is rather low below the particle threshold and the influence of truncated configurations at high excitation energies on the properties of low-lying states is very weak. Altogether it allows to consider the QPM calculations as rather realistic from the point of view of the basis completeness at low excitation energies. Although in scattering reactions the levels are mainly excited via one-phonon components of the wave function, multiphonon configurations are important because they are responsible for fragmentation of the one-phonon strength.

The structure of excited states in the QPM calculations is obtained from a diagonalization of the QPM Hamiltonian for the above-mentioned wave functions. The diagonalization yields eigenenergies of excited states and their wave functions in terms of phonons or $1p-1h$, $2p-2h$, and $3p-3h$ configurations. The model Hamiltonian is based on the idea of nucleons moving in an average self-consistent field and interacting with each other by means of a residual interaction

$$\mathbf{H} = \mathbf{H}_{s.p.} + \mathbf{H}_{pair} + \mathbf{H}_{r.i.}. \tag{2.50}$$

The first term in Eq. (2.50) corresponds to the average field for neutrons (n) and protons (p) and has in the second-quantized representation the form

$$\mathbf{H}_{s.p.} = \sum_{\tau}^{n,p} \sum_{j,m} E_{j\tau} \mathbf{a}^{+}_{jm\tau} \mathbf{a}_{jm\tau}, \tag{2.51}$$

where $j \equiv [n, l, j]$ and m are the quantum numbers, $\tau = -1(+1)$ refers to neutrons (protons), $E_{j\tau}$ is the energy of the single-particle level. $\mathbf{a}^{+}_{jm\tau}(\mathbf{a}_{jm\tau})$ are creation (annihilation) operators of particles in a state j with the above mentioned quantum numbers. The second part of Eq. (2.50) characterizes the residual interaction responsible for pairing in non-magic nuclei. It is described by a monopole pairing and is fixed from the description of pairing energies [111]. In a semi-magic nucleus the pairing term gives a non-zero contribution for either protons or neutrons in the open shells only. Since the QPM is usually applied to medium-mass and heavy nuclei with filling of different subshells of neutrons and protons, the neutron-proton monopole pairing is neglected.

The residual interaction $\mathbf{H}_{r.i.}$ is chosen in a separable form allowing for a multipole decomposition. Its part in the particle-hole channel can be written as

$$\mathbf{H}^{(p-h)}_{r.i.} = \sum_{\lambda\mu} \sum_{\tau\rho}^{\pm 1} (\kappa^{(\lambda)}_{0} + \rho\kappa^{(\lambda)}_{1}) \mathbf{M}^{+}_{\lambda\mu}(\tau) \mathbf{M}_{\lambda\mu}(\rho\tau)\,, \tag{2.52}$$

where $\kappa^{(\lambda)}_{0(1)}$ are the coupling constants, which determine the strength of isoscalar (isovector) residual interaction. The quantity $\rho = \pm 1$ differentiates between isoscalar and isovector transitions. For natural-parity states the multipole operator $\mathbf{M}^{+}_{\lambda\mu}(\tau)$ is given by

$$\mathbf{M}^{+}_{\lambda\mu}(\tau) = \sum_{j,m,j',m'} < jm\tau | i^{\lambda} f^{\tau}_{\lambda}(r) \mathbf{Y}_{\lambda\mu}(\Omega) | j'm'\tau > \mathbf{a}^{+}_{jm\tau} \mathbf{a}_{j'm'\tau} \tag{2.53}$$

and for unnatural-parity states by

$$\mathbf{M}^{+}_{\lambda\mu}(\tau) = \sum_{j,m,j',m',lm_1} < jm\tau | i^{l} f^{\tau}_{l}(r) [\sigma \cdot \mathbf{Y}_{lm_1}(\Omega)]_{\lambda\mu} | j'm'\tau > \mathbf{a}^{+}_{jm\tau} \mathbf{a}_{j'm'\tau}. \tag{2.54}$$

The function $f^{\tau}_{\lambda}(r)$ is a radial formfactor which is taken either in form r^{λ} or as a derivative of the central part of the average field $f^{\tau}_{\lambda}(r) = dU^{\tau}(r)/dr$.

The solution of the Schrödinger equation is obtained by means of a step-by-step diagonalization of the model Hamiltonian given in Eq. (2.50). The first two terms are diagonalized at the beginning. For this purpose Bogoliubov's canonical transformation from particle creation (annihilation) operators to quasiparticle creation (annihilation) operators is applied

$$\mathbf{a}^{+}_{jm\tau} = u_j \alpha^{+}_{jm\tau} + (-1)^{j-m} v_j \alpha_{j-m\tau}\,. \tag{2.55}$$

The values u^2_j and v^2_j correspond to occupation probabilities for particles and holes in the state j. The ground state of even-even nuclei is considered as a quasiparticle vacuum $\alpha_{jm\tau}|\rangle_q \equiv 0$. Minimization of the energy of the ground state,

$$\delta\{\Big\langle |\mathbf{H}_{s.p.} + \mathbf{H}_{pair}| \Big\rangle_q + \sum_{j} \mu_j (u^2_j + v^2_j - 1)\} = 0\,, \tag{2.56}$$

results in the well-known BCS equations, whose solutions provide the correlation functions $C_\tau = G_\tau^{(0)} \sum_j u_j v_j$ and the chemical potentials λ_τ for the neutron and proton systems. The coefficients of the Bogoliubov transformation can be calculated from these values according to

$$v_j^2 = \frac{1}{2}\left(1 - \frac{E_{j\tau} - \lambda_\tau}{\epsilon_{j\tau}}\right),\; u_j^2 = 1 - v_j^2\,, \tag{2.57}$$

where $\epsilon_{j\tau}$ is the quasiparticle energy:

$$\epsilon_{j\tau} = \sqrt{C_\tau^2 + [E_{j\tau} - \lambda_\tau]^2}\,. \tag{2.58}$$

Having diagonalized the first two terms of the model Hamiltonian, one can write

$$\mathbf{H}_{s.p.} + \mathbf{H}_{pair} = \sum_{\tau}^{n,p} \sum_{j,m} \epsilon_{j\tau} \alpha_{jm\tau}^{+} \alpha_{jm\tau}\,. \tag{2.59}$$

Since the ground state is determined as a quasiparticle vacuum, the simplest excited states are two-quasiparticle states $\alpha_{jm\tau}^{+}\alpha_{j'm'\tau}^{+}|\rangle_q$ which correspond to particle-hole transitions if monopole pairing vanishes. For collective transitions the process can also be described as creation of a phonon. The following phonon operator with multipolarity λ and projection μ is introduced

$$\mathbf{Q}_{\lambda\mu i}^{+} = \frac{1}{2}\sum_{\tau}^{n,p}\sum_{j,j'}\{\psi_{jj'\tau}^{\lambda i}[\alpha_{j\tau}^{+}\alpha_{j'\tau}^{+}]_{\lambda\mu} - (-1)^{\lambda-\mu}\phi_{jj'\tau}^{\lambda i}[\alpha_{j'\tau}\alpha_{j\tau}]_{\lambda-\mu}\}\,. \tag{2.60}$$

The total number of different phonons for a given λ should be equal to the sum of neutron and proton two-quasiparticle states coupled to the same angular momentum. An index i, the so-called root quantum number, is used to label these phonons. The coefficients $\psi_{jj'\tau}^{\lambda i}$ and $\phi_{jj'\tau}^{\lambda i}$ can be obtained from a diagonalization of the Hamiltonian in the space of one-phonon states $\mathbf{Q}_{\lambda\mu i}^{+}|\rangle_{ph}$. This can be accomplished by the variation procedure

$$\delta\left\{\langle|\mathbf{Q}_{\lambda\mu i}\mathbf{H}\mathbf{Q}_{\lambda\mu i}^{+}|\rangle_{ph} - (\omega_{\lambda i}/2)\left[\sum_{jj'}\{(\psi_{jj'\tau}^{\lambda i})^2 - (\phi_{jj'\tau}^{\lambda i})^2\} - 2\right]\right\} = 0\,, \tag{2.61}$$

where $\omega_{\lambda i}$ is the energy of the phonon i. This procedure yields the well-known RPA equations, whose solutions for each multipolarity λ^π give a spectrum of one-phonon excitations. These equations have been obtained under the assumption that the ground state is the phonon vacuum. Thus, the ground-state correlations due to the last term of the model Hamiltonian, $\mathbf{H}_{r.i.}$, are taken into account. The phonons $\mathbf{Q}_{\lambda\mu i}^{+}$ describe excitation modes in the parent nucleus without changing its isospin.

The self-consistent field for neutrons and protons is approximated by a phenomenological Woods-Saxon potential with parameters from [114]

$$U^\tau(r) = \frac{V_0^\tau}{1 + e^{(r-R_0^\tau)/a_0^\tau}} - \frac{\hbar^2}{\mu^2 c^2}\frac{1}{r}\frac{d}{dr}\left(\frac{V_{ls}^\tau}{1 + e^{(r-R_{ls}^\tau)/a_{ls}^\tau}}\mathbf{l}\cdot\mathbf{s}\right) + V_{Coul}(r)\,, \tag{2.62}$$

including a central, a spin-orbit and a Coulomb term, respectively.

The present work deals with giant resonances, *i.e.* with collective excitations of nuclei, as well as low-lying excitations. GRs are characterized by many $1p-1h$ amplitudes which basically contribute in-phase to wave functions of phonons in the resonance region and therefore describe a collective motion of the nucleus. Complex configurations, for example two-phonon states, are not so important for the description of global properties of the GDR like the energy-weighted sum rule or the centroid energy. However, it is necessary to take them into account in order to explain the experimentally observed strength fragmentation, *i.e.* the fine structure of the giant resonance, and to describe the low-lying pygmy dipole modes. After solving the RPA equations the model Hamiltonian can be rewritten in terms of the phonon operators.

$$\mathbf{H} = \sum_{\lambda\mu i} \bar{\omega}_{\lambda i} Q^{+}_{\lambda\mu i} Q_{\lambda\mu i} + \mathbf{H}_{int.}\,. \tag{2.63}$$

The second term $\mathbf{H}_{int.}$ contains the remaining, not yet accounted for part of the residual interaction, which cannot be projected onto the space of the phonon operators. One can expand it in an infinite sum of even-number phonon operators. Keeping just the first term of the expansion, *i.e.* only two-phonon operators, the non-diagonal terms of the model Hamiltonian $\mathbf{H}_{int.}$ in the space of phonon operators are obtained in the form

$$\mathbf{H}_{int.} = \sum_{\substack{\lambda\mu i\\ \lambda_1\mu_1 i_1\\ \lambda_2\mu_2 i_2}} U^{\lambda_1 i_1}_{\lambda_2 i_2}(\lambda i) Q^{+}_{\lambda\mu i} [Q_{\lambda_1\mu_1 i_1} Q_{\lambda_2\mu_2 i_2}]_{\lambda\mu} + h.c.\,, \tag{2.64}$$

where the matrix elements of the interaction between one- and two-phonon configurations $U^{\lambda_1 i_1}_{\lambda_2 i_2}(\lambda i)$ can be calculated by making use of the internal fermion structure, *i.e.* from the amplitudes $\psi^{\lambda_2 i_2}_{jj'}$, $\phi^{\lambda_2 i_2}_{jj'}$; $\bar{\psi}^{\lambda_1 i_1}_{jj'}$, $\bar{\phi}^{\lambda_1 i_1}_{jj'}$, and $\bar{\psi}^{\lambda i}_{jj'}$, $\bar{\phi}^{\lambda i}_{jj'}$.

Accordingly, the wave function of excited states with angular momentum λ and projection μ in even-even nuclei in the most general form can be written as a composition of one-, two-, and three-phonon configurations

$$\begin{aligned} |\Psi\rangle_{\lambda\mu} = \Bigg(&\sum_{i} R_i\, Q^{+}_{\lambda\mu i} + \sum_{\substack{\lambda_1\mu_1 i_1\\ \lambda_2\mu_2 i_2}} P^{\lambda_1 i_1}_{\lambda_2 i_2} [Q^{+}_{\lambda_1\mu_1 i_1} Q^{+}_{\lambda_2\mu_2 i_2}]_{\lambda\mu} \\ &+ \sum_{\substack{\lambda_1\mu_1 i_1 \lambda_2\mu_2 i_2\\ \lambda_3\mu_3 i_3}} T^{\lambda_1 i_1 \lambda_2 i_2}_{\lambda_3 i_3}\, [Q^{+}_{\lambda_1\mu_1 i_1} Q^{+}_{\lambda_2\mu_2 i_2} Q^{+}_{\lambda_3\mu_3 i_3}]_{\lambda\mu} \Bigg) |\rangle_{ph}\,. \end{aligned} \tag{2.65}$$

The coefficients R, P, and T together with eigenenergies of the states (2.65) are calculated from the diagonalization of the Hamiltonian (2.63) in the space of the states (2.65).

This diagonalization is very useful for saving computational time. It allows to truncate a huge space of three-phonon configurations on a physical level by excluding the ones with very small matrix elements, *e.g.* $|U^{\lambda_1 i_1}_{\lambda_2 i_2}(\lambda i)| < 0.01|U_{max}|$. The omitted two- and three-phonon configurations give almost no contribution to the damping process of collective one-phonon states and their exclusion allows to significantly reduce the rank of the matrices to be diagonalized. The single-particle basis in QPM calculations is rather complete and includes all mean-field levels from $1s_{1/2}$ to quasi-bound levels in the continuum. For this reason, no effective charges are needed to describe collectivity of low-lying excited states [115].

2.4.2 Relativistic quasiparticle time blocking approximation

The relativistic quasiparticle time blocking approximation [116, 117] is based on the covariant density functional theory (CDFT) and utilizes a fully consistent parameter-free technique to account for nucleonic configurations beyond the simplest two-quasiparticle (2q) ones. Its excited states are built of the two-quasiparticle-phonon (2q⊗phonon) configurations.

The RQTBA is based on the relativistic mean field (RMF) between neutrons and protons, generated in a self-consistent way by the exchange of mesons and the photons. RMF models based on the CDFT have been successfully applied to describe ground state properties of finite spherical and deformed nuclei over the entire nuclear chart [118]. The relativistic random phase approximation (RRPA) [119] and the quasiparticle RRPA (RQRPA) [120], formulated as the small amplitude limit of the time-dependent RMF models were used for a description of excited nuclear states.

The main assumption of the quasiparticle-phonon coupling [121] is that two-quasiparticle and vibrational modes are coupled in such a way that configurations of 2q⊗phonon type with low-lying phonons strongly compete with simple 2q configurations close in energy or that quasiparticles can emit and absorb phonons with comparably high probabilities. Obviously, these processes affect both, the ground and excited states. Therefore, the corresponding amplitudes should be taken into account in the single-nucleon self-energy and in the effective interaction in the nuclear interior. Correspondingly, in addition to the spreading over the two-quasiparticle states, a fragmentation of the nuclear states over the two-phonon configurations appears in the excitation spectra. The quasiparticles are of Bogoliubov type and discussed in Sec. 2.4.1 The RQTBA model space is constructed from the particles that move in mean field and phonons computed within the RQRPA. The covariant density functional was obtained using the NL3 parameter set [122].

The computational procedure of the dipole strength can be described by the following main steps

- Calculation of the ground state properties.
  This requires a simultaneous solution of the Dirac + BCS equations for single nucleons and the Klein-Gordon equations for meson fields in a self-consistent way to get the single-particle basis. The Dirac equation can be written in the following form:

$$\int dx'\mathbf{H}^{\mathbf{D}}(\mathbf{x},\mathbf{x}')\phi(\mathbf{x},\mathbf{x}') = (\mathbf{m}+\varepsilon_{\mathbf{k}})\phi(\mathbf{x},\mathbf{x}'), \tag{2.66}$$

  where the coordinate $x = \{r, \alpha, t\}$ combines spatial coordinates r with Dirac index α =1,...,4, and $\mathbf{H}^{\mathbf{D}}$ is a single-particle Dirac Hamiltonian given in the form

$$\mathbf{H}^{\mathbf{D}} = \alpha\mathbf{p} + \beta\left(\mathbf{m} + \widetilde{\Sigma}\right). \tag{2.67}$$

  Here, α and β are Dirac matrices, $\boldsymbol{m}$ stands for the particle mass and $\widetilde{\Sigma}$ is the RMF self-energy. Using the BCS equation one defines the pairing field

$$\triangle_k = -\frac{1}{2}\sum_{k'} V^{pp}_{k\vec{k},k'\vec{k}'}\frac{\triangle_{k'}}{2E_{k'}}, \tag{2.68}$$

  where E_k is a quasiparticle energy, V^{pp} describes the particle-particle interaction and k is a set of quantum numbers $k = \{n_k, j_k, \pi_k, \tau_k\}$. The Klein-Gordon equations that describe the behavior of the meson and Coulomb fields in the static case have the form

$$\triangle\phi_m(r)+U'(\phi_m(r))=\mp\sum_k V_k^T(r)\beta\Gamma_m V_k^*(r). \tag{2.69}$$

Here, ϕ_m describes the classical fields of mesons and the photon $\phi_m=\{\sigma,\omega^\mu,\vec{\rho}^\mu,A^\mu\}$, $U(\phi_m)$ is given by the term $U(\phi_m)=\frac{1}{2}m_m^2\phi_m^2$, containing the meson masses, β is the Dirac matrix, the interaction potential is given by $V_k(r)$. The plus and minus signs hold for scalar and vector fields, respectively. The vertices Γ_m are given by

$$\Gamma_\sigma=g_\sigma,\ \ \Gamma_\omega^\mu=g_\omega^\mu\gamma^\mu,\ \ \vec{\Gamma}_\rho^\mu=g_\rho^\mu\vec{\tau}\gamma^\mu,\ \ \Gamma_e^\mu=e\frac{1-\tau_3}{2}\gamma^\mu, \tag{2.70}$$

with the corresponding coupling constants g_m and amplitudes γ^μ for the meson fields and for the electromagnetic field.

- Solution of the RQRPA equations for transition densities with the static interaction.
  It determines the low-lying collective vibrations (phonons), their energies and amplitudes. The RQRPA equations including quasiparticle phonon coupling in the linearized version can be expanded in the form

  $$\mathscr{R}^\eta_{\mu;k_1k_2}=\tilde{R}^{(0)\eta}_{k_1k_2}\sum_{k_3k_4}\sum_{\eta'}\tilde{V}^{\eta\eta'}_{k_1k_4,k_2k_3}\mathscr{R}^{\eta'}_{\mu;k_3k_4}, \tag{2.71}$$

  where $\mathscr{R}_\mu$ are the transition densities, $\tilde{R}$ is the two-particle propagator or the mean-field response function, and $\tilde{V}$ stands for the static quasiparticle interaction. This provides two sets of quasiparticles and phonons forming the 2q⊗phonon configurations which enter the quasiparticle-phonon coupling amplitude.

- Computation of the Bethe-Salpeter equation for the response function.
  In the quasiparticle time blocking approximation a time-projection technique is used to block the two-quasiparticle propagation through the states which have more complicated structure than 2q⊗phonon [123]. The nuclear response is then explicitly calculated on this level by summation of infinite series of Feynman's diagrams. Examples of such diagrams are schematically shown in Fig. 2.5.

- Double convolution of the response function with the external field.
  This is necessary in order to obtain polarizability and strength function, and to determine the excitation spectrum of the nucleus.

In the full model space, phonons of multipolarities 2^+, 3^-, 4^+, 5^-, 6^+ with energies below 10 MeV are included. The approach was successfully applied to study the low-lying dipole strength as well as the giant dipole resonance in neutron-rich $^{68-78}$Ni and in the chain of even-mass $^{100-140}$Sn isotopes and $N=50$ isotones [117, 125]. A comparison to the recent experimental data (see e.g. [126, 127]) shows fairly good agreement of the RQTBA results. The doubly magic structure of the ^{208}Pb nucleus investigated in the present work allows to use the relativistic time blocking approximation without the inclusion of the paring effects in to the interaction [117].

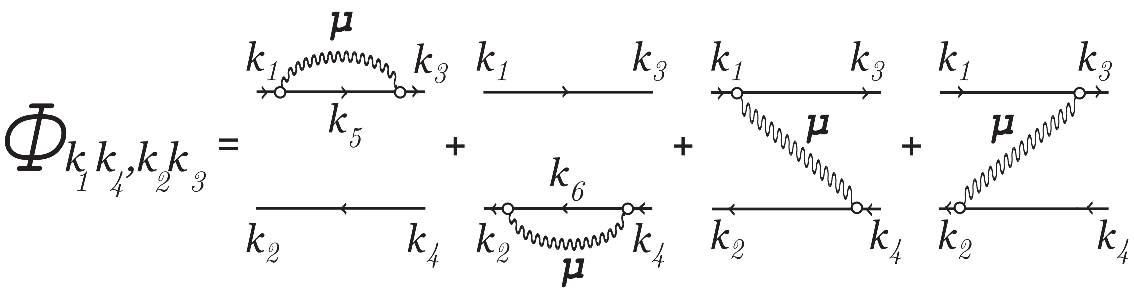

Fig. 2.5: 2q⊗phonon amplitude in the Feynman diagram representation. Solid lines with arrows and latin indices denote the single-quasiparticle nucleonic propagators, wavy curves with greek indices the phonon propagators, empty circles stand for phonon vertices [124].

2.5 Theoretical models for level density extraction

Nuclear level densities (NLD) represent the basic statistical information on nuclei at low and especially at higher energies. A lot of theoretical approaches were developed to investigate the total number of levels depending on the excitation energy E_x and spin J [128, 129]. The widely used back-shifted Fermi gas model [130, 131, 132] represents the semiimpirical modification to the original expression [133] including shell and pairing effects. The model was shown to satisfactorily describe nuclear level densities in a variety of nuclei up to 20 MeV excitation energy [134]. The formulas for the level density are usually separated in a part with the total level density $\rho(E)$ increasing exponentially with excitation energy E and a function for the spin distribution $f(J)$

$$\rho(E,J) = f(J)\rho(E). \tag{2.72}$$

A possible dependence on the level parity is neglected. In the BSFG model, the energy and spin dependence of the NLD are given by

$$\rho(E) = \frac{1}{12a^{1/4}} \frac{e^{2\sqrt{a(E_x-\delta)}}}{\sqrt{2}\sigma(E_x-\delta)^{5/4}}, \tag{2.73}$$

$$f(J) = \frac{2J+1}{a\sigma^2} e^{\frac{-J(J+1/2)}{2\sigma^2}}, \tag{2.74}$$

with the spin cut-off parameter σ^2=0.0888A$^{2/3}\sqrt{a(E_x-\delta}$, depending on the moment of inertia of the nucleus. Parameters a and δ denote the density of the single-particle states near the Fermi level and the back-shift of the ground state due to pairing and shell effects, respectively. Normally, a is determined from a fit to data. Attempts have been made to extract a systematic dependence of a on basic parameters of nuclei like ground states binding energies and mass numbers. One possible approach is given by Ref. [135]. There, the parameter a with included energy dependence can be expressed as

$$a\left(E_x-\delta, N, Z\right) = \tilde{a}(A)\left[1 + \frac{S(Z,N)-\Delta}{E_x-\delta} f\left(E_x-\delta\right)\right], \tag{2.75}$$

where

$$\tilde{a}(A) = \alpha A + \beta A^{2/3},\ f\left(E_x-\delta\right) = 1 - \exp\left(-\gamma\left(E_x-\delta\right)\right). \tag{2.76}$$

Here A is the mass number. The values of the free parameters α, β and γ were determined by a fit to experimental data in 272 nuclei and are given below

$$\alpha = 0.1337,\ \beta = -0.06571,\ \gamma = 0.04884\,. \tag{2.77}$$

The so-called shell correction parameter $S(Z,N)$ describes deformation-dependent effects which are vanishing at high excitation energies, and is defined as

$$S(Z,N) = M_{exp} - M_{LD}, \tag{2.78}$$

where M_{exp} is the experimental mass and M_{LD} is calculated with the liquid-drop model formula. As the pairing effects are not included, the pairing energy Δ has to be subtracted.

At low excitation energies the use of simple models with a small number of parameters, such as the Fermi gas model, is still one of the most practical ways of calculating nuclear level densities. One of the simplest models that can be used is the constant-temperature (CT) model. This is based on the definition of the nuclear temperature T as [121,136]

$$T^{-1} = \frac{d[\ln \rho(E_x)]}{dE_x}, \tag{2.79}$$

where $\rho(E_x)$ is the level density at excitation energy E_x. Assuming that temperature T is constant, one obtains the CT model expression

$$\rho(E_x) = \frac{1}{T} e^{\frac{E_x - E_0}{T}}\,. \tag{2.80}$$

Here, E_0 is a ground state back-shift energy. It was noted [137] that this simple formula gives a good fit to the cumulated number of levels at excitation energies E_x up to the neutron separation energy. It was also shown [137,138] that CT and BSFG models are equivalent in many cases at excitation energies below 10 MeV.

Besides these two phenomenological approaches described above, level densities obtained within a microscopic statistical model [128] are often applied. These calculations are performed using the deformed Hartree-Fock-BCS (HF-BCS) predictions of the ground-state structure properties and include a consistent treatment of the shell effects, pairing correlations, deformation effects and collective excitations. Among the other microscopic NLD approaches, the combinatorial approach has also proved its predictive power and recent developments have demonstrated that such an approach can clearly compete with the statistical approach in the global reproduction of experimental data [129]. One of the advantages of this approach is to provide not only the energy and spin dependence of the level densities, but also the parity dependence as well as the partial particlehole level density. At low energies, the combinatorial predictions also provide the non-statistical limit where by definition the statistical approach cannot be applied.

The cumulative number of levels as a function of excitation energy E_x is obtained by the integration of Eq. (2.72)

$$N_0\left(E_x,J\right) = \int_0^{E_x} \rho\left(E,J\right) dE\,. \tag{2.81}$$

The mean level spacing $\langle D\rangle$ in the energy interval $\left[E_x^a, E_x^b\right]$ can be expressed as

$$\langle D\rangle = \frac{E_x^b - E_x^a}{N_0\left(E_x^b,J\right) - N_0\left(E_x^a,J\right)}\,. \tag{2.82}$$

In the framework of this thesis the complete dipole strength distribution in ^{208}Pb has been studied with the ($\vec{p}$,$\vec{p}'$) reaction at very forward angles including zero degree. The experiment was performed at the ring cyclotron facility of the Research Center for Nuclear Physics (RCNP), Osaka University. An overview of the RCNP facility is shown in Fig. 3.1. A high intensity polarized ion source (HIPIS) provided a polarized proton beam employing the cold atomic beam techno-

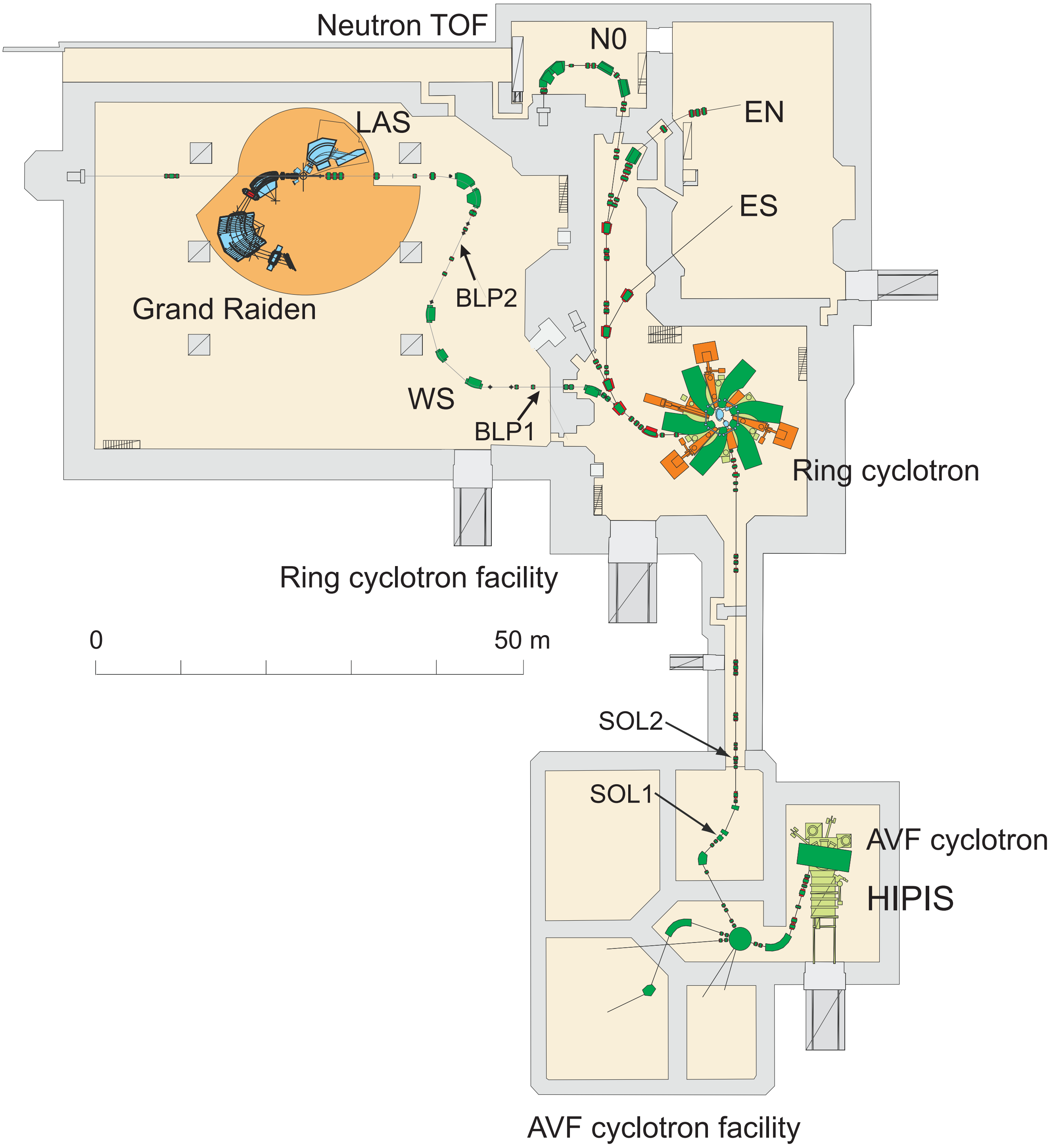

Fig. 3.1: Schematic layout of the RCNP cyclotron facility.

logy and an electron cyclotron resonance ionizer [139]. After bending from the horizontal to the vertical direction, the proton beam was injected to the K = 140 MeV Azimuthally Varying Field (AVF) cyclotron and there accelerated up to a kinetic energy of 54 MeV. The direction of the proton polarization was reversed every second to eliminate the geometrical asymmetries of the experimental setup. Further, the polarized protons were accelerated up to 295 MeV using a six sector ring cyclotron (K400) in a coupled mode. In order to control the spin axis of the polarized protons, two superconducting solenoids (SOL1, SOL2 in Fig. 3.1) are equipped in the injection line between two cyclotrons. After the ring cyclotron protons can be delivered to different experimental halls to perform a variety of experiments, e.g. to study unstable nuclei using East-North (EN) beam line [140] or ultra cold neutrons production in the East-South (ES) course. Using North (N0) beam line together with neutron-TOF setup one learn about spin-isospin excitations with (p,n) reactions [141]. In the present measurements a polarized proton beam with an energy of 295 MeV was transported to the target through the high resolution West-South (WS) [142] beam line. Two beam line polarimeters (BLP1 and BLP2 in Fig. 3.1) are placed in the WS beam line to control the beam polarization. Scattered protons were analyzed with the high resolution magnetic spectrometer Grand Raiden [143] and its focal plane detectors [144], while polarization transfer coefficients were measured by the focal plane polarimeter (FPP) [145], located downstream of the focal plane detectors. The so-called Large Acceptance Spectrometer (LAS) [146] was simultaneously used to monitor the vertical beam position, which is needed for the reconstruction of scattering angles.

3.1 Experimental conditions

The beam time was separated into two periods. In the first part (October, 2006) the measurements at angles between 0° and 10° with sideways polarized proton beam (10 days in total) were performed . The measurements with longitudinal polarization at 0° and 2.5° (14 days in total) were carried out in the second period (November, 2008). The polarization of the beam was typically about 70% during both periods, and an energy resolution of 25-30 keV full width at half maximum (FWHM) was achieved. Typical beam intensities on the target were 1-10 nA. Side-ways (D_{SS}) and longitudinal (D_{LL}) polarization transfer coefficients and analyzing power of the reaction were determined at 0°. Due to some technical problems, measurements had to be performed with two different magnetic field settings (called mag1 and mag2) during both periods. In order to achieve sufficient background suppression in the 0° measurements a stable halo-free beam is required. Thus, beam tuning is essential for such kind of experiments. Utilizing in addition lateral and angular dispersion matching techniques [147], a high energy resolution in the order of $\Delta E/E = 8 \cdot 10^{-5}$ could be obtained. To gain both good background subtraction and scattering angle resolution, the Grand Raiden spectrometer was used in an underfocus mode. For the calibration of the scattering angles, elastic scattering with a sieve-slit collimator was employed. It was performed at 10° and off a ^{208}Pb target with thickness of about 60 mg/cm^2 in October 2006 and at 16° off a 100 mg/cm^2 thick ^{58}Ni target in November 2008.

3.2 Beam line polarimeter

The polarization of the protons was constantly controlled by two sampling-type beam line polarimeters (BLP1 and BLP2 in Fig. 3.1) placed in the WS beam line. The BLPs consist of four (left, right, up and down) pairs of plastic scintillation counters to measure p-p scattering from a polyethylene $(CH_2)_n$ foil with an areal density of 3.5 mg/cm^2. In Fig. 3.2 left (L-L′) and right (R-R′) pairs of scintillators in the horizontal plane can be seen. The other (up and down) pairs are located in the vertical plane. Each pair of the detectors registers elastically and quasi-elastically scattered and recoiling protons from a BLP-target in coincidence. The scintillators were located

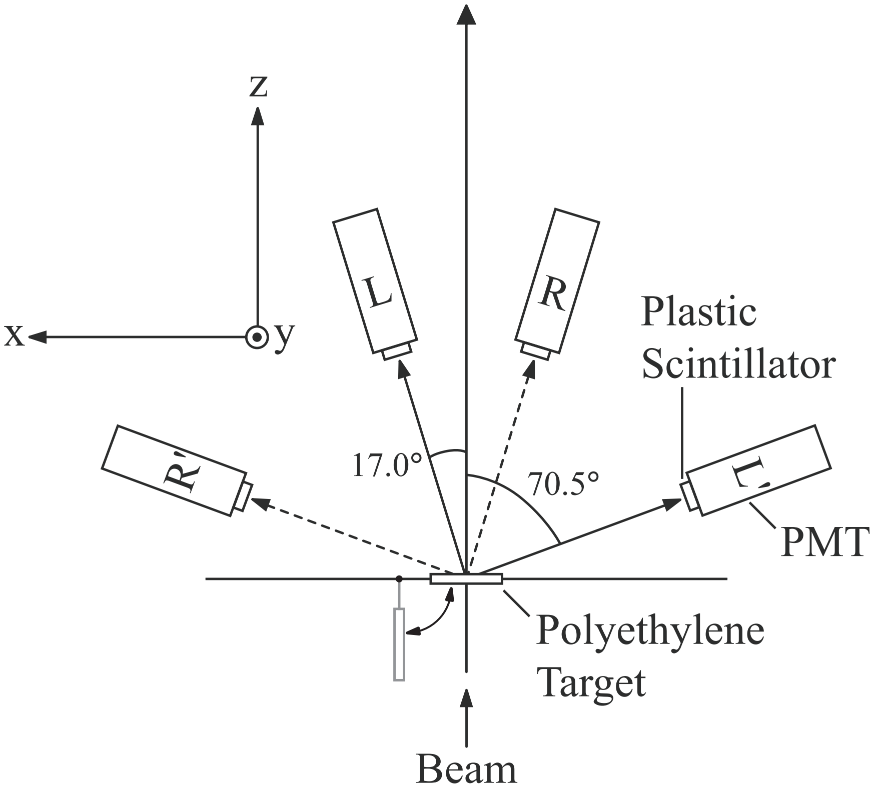

Fig. 3.2: Setup of the BLP (top view).

at scattering and recoil angles of 17.0° and 70.5°, respectively, where p-p scattering at E_p=295 MeV shows a large effective analyzing power A_y=0.40±0.01 [148]. By using two BLPs one is able to determine all three-dimensional beam polarization components. The polyethylene target was periodically (1 s out of 10 s) put into the beam only for the polarization measurements, in order not to produce additional background during collection of focal plane events.

3.3 The 0° setup

Figure 3.3 shows the experimental setup of the spectrometers and their detector systems in the 0° measurements. A two-arm spectrometer system, which consist of the Grand Raiden [143] and Large Acceptance spectrometer [146, 149] was employed. The proton beam with an energy of about 295 MeV hit a target placed at the center of the scattering chamber. Typically, the beam intensity was 1-10 nA and a target with density of about 5 mg/cm^2 were used. The LAS measured quasi-free scattering protons to monitor the beam position at the target in the vertical direction. It was placed at Θ_{lab} = 60°, the most forward possible angle when the GR spectrometer is placed under 0°, throughout the experiment. For measurements at 0°, the primary beam was transported inside the Grand Raiden through focal plane detectors and then stopped in the Faraday cup (0°-FC). The 0°-FC was placed 12 m downstream of the focal plane of the Grand Raiden and surrounded by concrete, lead and iron blocks to suppress background events. A doublet of quadrupole magnets (Dump-Q) was installed for a better beam transmission to the beam dump. An electron sweeper was placed inside the concrete block, to bend electrons which were created upstream and to allow a precise measurement of the collected charge. To restrain electrons produced inside the Faraday cup a permanent magnet is placed at the entrance of the Faraday cup. For the better beam tuning at the focal plane, beam viewers are installed in front of the 0°-FC and Dump-Q magnets.

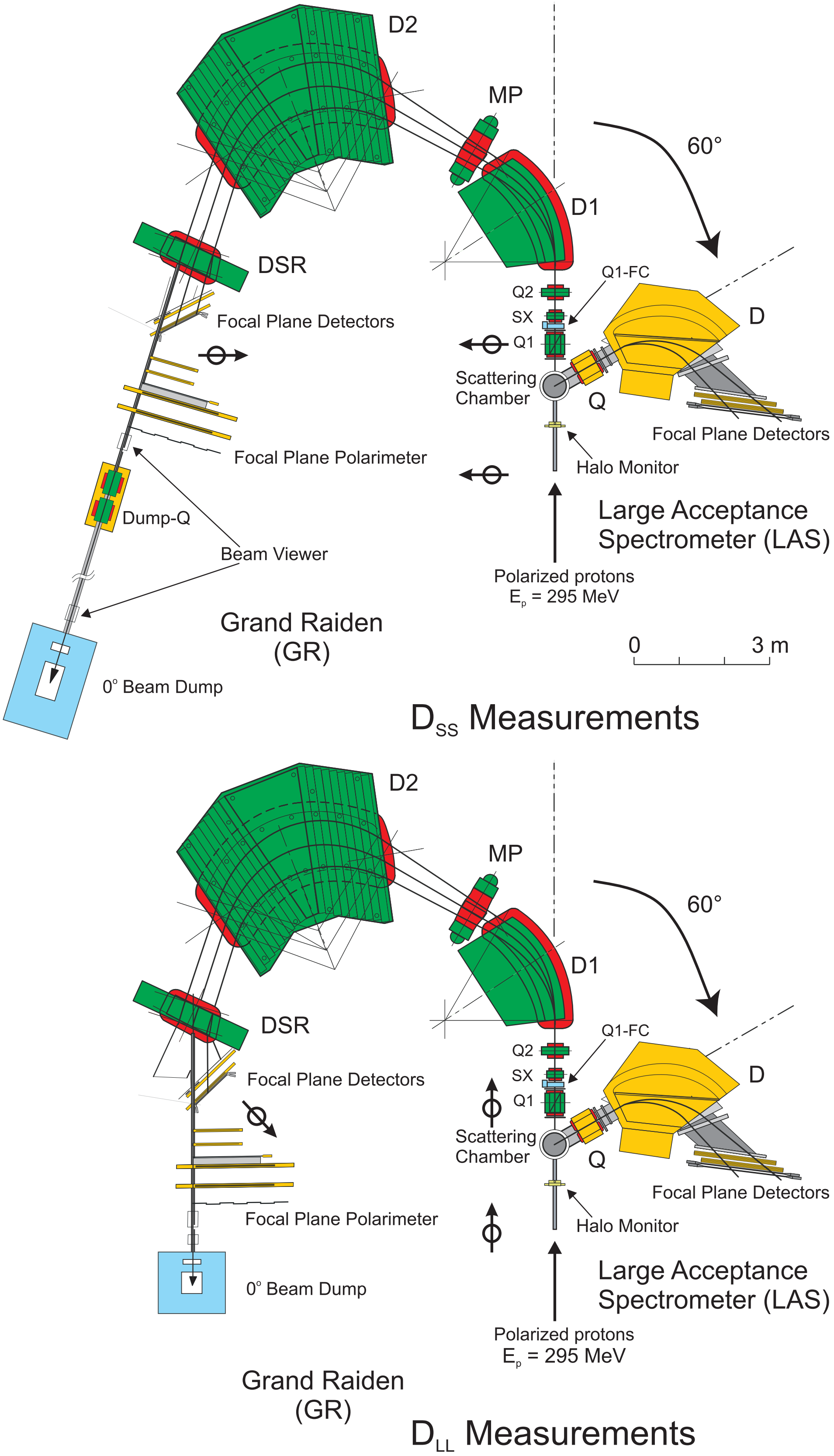

Fig. 3.3: Experimental setup of 0° proton inelastic scattering measurements with sideways (top) and longitudinally (bottom) polarized proton beam.

3.3.1 Grand Raiden

The GR spectrometer has a Q-SX-Q-D-MP-D-D configuration, where D indicates dipole magnets (D1, D2 and DSR), Q stands for quadrupoles (Q1 and Q2) and SX and MP denote sextupole and multipole magnets, respectively. Grand Raiden has a high momentum resolving power of $p/\Delta p \approx 3.7{\cdot}10^4$ and a momentum acceptance of 5%. Design specifications of the spectrometer are summarized in Table 3.1. The multipole magnet is served to minimize higher-order aberrations. The third dipole magnet is called the dipole magnet for spin rotation (DSR). A so-called DSR+ mode (shown in Fig. 3.3 bottom), is used for the measurement of the longitudinal polarization of the scattered protons. It is able to bend protons additionally by +18° or -17° without degrading the resolving power of Grand Raiden. The focal plane detector system of the GR spectrometer consists of two parts: the vertical drift chambers (VDCs) with plastic scintillators and the focal plane polarimeter. The GR was placed at 0°, 2.5°, 4°, 6°, 8°and 10° in the inelastic scattering measurement to observe angular distributions of the differential cross section.

Tab. 3.1: Parameters of the GR and LAS spectrometers

	Grand Raiden	Large Acceptance Spectrometer
Configuration	Q1-SX-Q2-D1(-MP)-D2(-DSR)	QD
Mean orbit radius	3 m	1.5 m
Total deflection angle	162°	70°
Focal plane tilting angle	45°	57°
Maximum magnetic rigidity	5.4 T·m	3.2 T·m
Momentum range	5%	30%
Momentum resolution	37076	4980
Horizontal magnification	-0.417	-0.4
Vertical magnification	5.98	-7.3
Horizontal angle acceptance	±20 mr	±60 mr
Vertical angle acceptance	±70 mr	±100 mr

3.3.2 Large acceptance spectrometer

The LAS [32] is a QD type spectrometer with a large momentum acceptance of $\Delta p/p = 30\%$ and a solid angle of 20 msr. In Table 3.1 the specifications of the LAS are summarized. The spectrometer was placed at 60° throughout the experiment to monitor the beam position in the vertical direction at the target by mainly measuring the quasi-free scattered protons from the target. Since the vertical magnification of the LAS is as large as 7.3, the vertical position at the focal plane detector was sensitive to the vertical beam position. The vertical angular acceptance of the LAS was reduced to ±6 mr by an entrance collimator for improving the beam position resolution such that a ±0.01 mm shift of the center of the vertical beam position can be detected. The precision corresponded to less than ±0.02° in the systematic uncertainty of the vertical scattering angle. Pairs of multiwire drift chambers and two planes of plastic trigger scintillation counters form the focal plane detector system [149]. The detailed description of the parameters of the LAS detectors can be found in Tab. 3.2.

3.4 Detector systems

The detector system of Grand Raiden consists of two major parts: the Focal Plane Detector System (FPDS) [144] and the Focal Plane Polarimeter (FPP) [145]. To reconstruct the most important parameters of the reaction such as the scattering angle of the particles and the excitation energy, the FPDS was used. The FPP was utilized to determine polarization of scattered protons. A schematic layout of the detector system of the Grand Raiden is presented in Fig. 3.4.

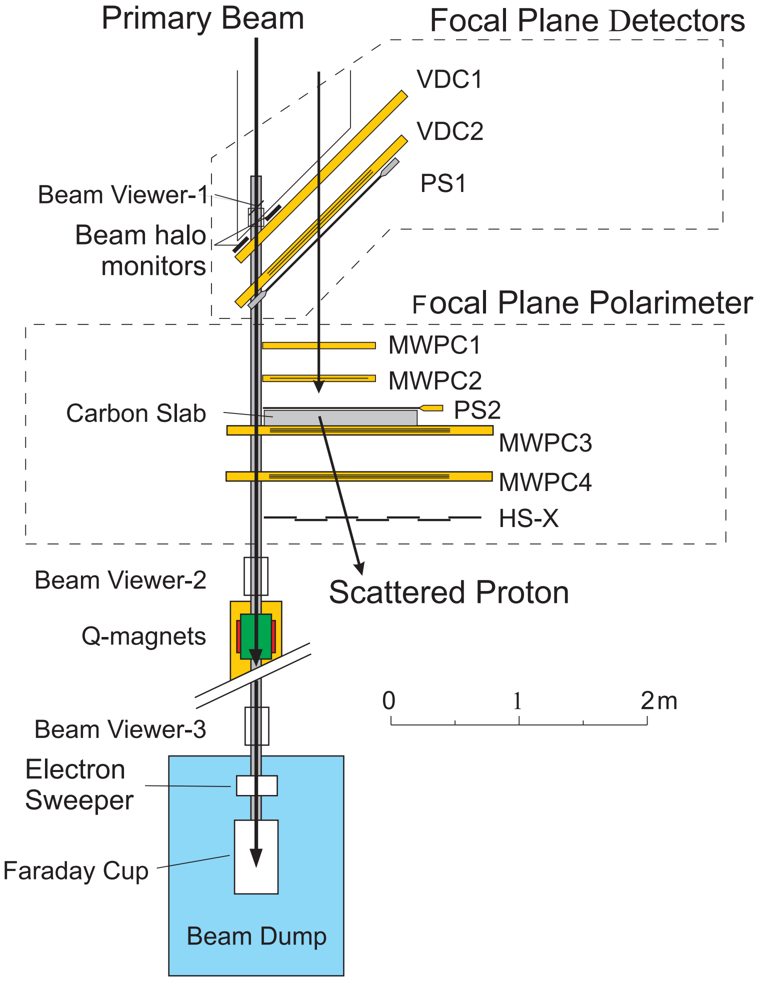

Fig. 3.4: Layout of the Grand Raiden detector system. It consists of two major parts: focal plane detector system and focal plane polarimeter.

3.4.1 Focal plane detector system

The FPDS contains two multiwire drift chambers of the vertical type, so-called Vertical Drift Chambers (VDC), and a plastic scintillator. VDCs are especially suited for the reconstruction of particle trajectories and sensitive to the position and scattering angle of the particles. Specifications of the Grand Raiden and LAS VDCs are summarized in Table 3.2. Four parameters, x_{fp}, θ_{fp}, y_{fp}, ϕ_{fp}, are measured by using two sets of VDCs, where x_{fp} and θ_{fp} are intersection point and intersection angle of the particle in the focal plane, respectively, the y_{fp} and ϕ_{fp} denote those in the non-dispersive plane of the system.

Passing through the chamber, scattered particles ionize the working gas and produce ion-electron pairs. By measuring the drift times of the electrons in the electric field of the chamber,

Tab. 3.2: Parameters of the vertical drift chambers of GR and LAS

	Grand Raiden	Large Acceptance Spectrometer
Wire configuration	X(0°), U(-48.2°)	X(0°), U(-31°), V(+31°)
Active area, mm2	$1150^{W} \times 120^{H}$	$1700^{W} \times 350^{H}$
Number of sense wires	192(X), 208(U)	272(X), 256(U,V)
Anode-cathode gap	10 mm	10 mm
Anode wire spacing	2 mm	2 mm(X), 2.33 mm(U,V)
Sense wire spacing	6 mm(X), 4 mm(U)	6 mm(X), 7 mm(U,V)
Applied voltage	-5.6 kV (cath.), -0.3 kV (pot.)	-5.5 kV (cath.), -0.3 kV (pot.)
Entrance and exit window	12.5 μm aramid film	25 μm aramid film
Sense wires	20 μm ∅ gold-plated tungsten wire	
Potential wires	50 μm ∅ gold-plated beryllium-copper wire	
Cathode	10 μm-thick carbon-aramid film	
Gas mixture	Argon (70%) + Iso-butane (30%) + Isopropyl-alcohol	
Pre-amplifier	LeCroy 2735DC	
Digitizer	LeCroy 3377 TDC	

it is possible to reconstruct particle rays in the plane perpendicular to the wires. The wire configurations of the GR drift chambers is illustrated in Fig. 3.5. Each VDC consists of two sets of anode wire planes (X and U), sandwiched between three cathode planes. In the X plane 192

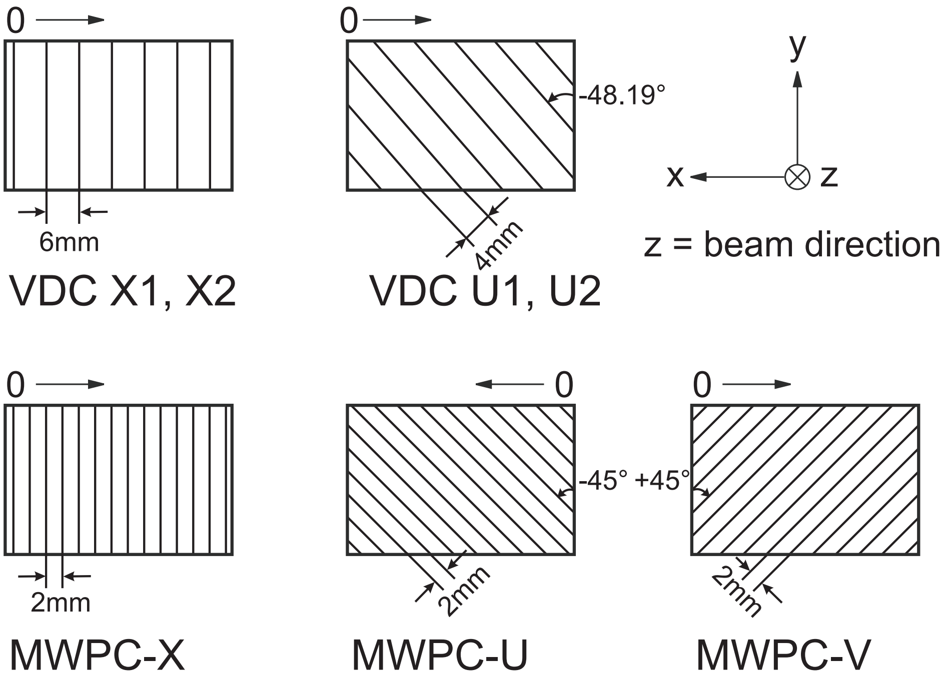

Fig. 3.5: Wires configurations of the VDCs and MWPCs. The arrows show the numbering order of wires.

wires are stretched perpendicular to the dispersion direction of the GR, while in the U plane, 208 wires are used tilted to an angle of ±48.19° relative to the X plane wires. Therefore, the X1 and X2 planes are responsible for the determination of x_{fp} and θ_{fp}, while the U1 and U2 planes provide the information about the intersection point and intersection angle in the non-dispersive plane. Combining data from X and U plane one is able to extract y_{fp}, ϕ_{fp}. The cathode planes of VDCs were set to a negative potential of -5.6 kV, and a high voltage of -0.3 kV was applied to the the potential wires, while the sense wires remained at ground level. Drift chambers were filled with argon (71%), iso-butane (29%) and iso-propyl-alcohol gas mixture. Signals from the sense wires were amplified and discriminated with LeCroy 2735DC cards and timing information was digitized with the LeCroy 3377 drift chamber TDC.

In order to reach an excitation energy as low as possible in the measurements at 0°, each chamber had a hole to place a beam duct guiding a primary protons to the beam dump. The distance between the center of the hole and the edge of the sense area was 20 cm making the available minimum energy as low as 4 MeV at 295 MeV. Lead blocks were placed between the two MWDCs close to the beam duct to reduce background particles. A plastic scintillator (PS1) with thickness of about 3 mm was used to determine the energy loss of scattered protons for the particle identification (see Sec. 4.1). The thickness of the detector PS1 is chosen, so that second scattering angle in the carbon slab can be measured with sufficient accuracy.

3.4.2 Focal plane polarimeter

The second part of the detector system, the focal plane polarimeter, served to measure the polarization of the scattered protons. The measurement is based on the inclusive elastic, inelastic and quasi-free scattering of polarized protons from a carbon analyzer slab. If a polarized particle passes through the carbon analyzer, it causes an azimuthal asymmetry in the scattering due to the spin-orbit interaction between the projectile and the ^{12}C nucleus. The measured asymmetry in the focal plane along with the spin-transfer matrix of the spectrometer is used to determine the polarization of the protons at the initial reaction vertex. As seen from Fig. 3.4, the FPP contains four multiwire proportional chambers (MWPC), a carbon block as a second scatterer, a plastic scintillator (PS2) and a hodoscope (HS) from plastic scintillator detectors. Two of the four MWPCs are placed before the C-analyzer and two behind it to determine the tracking rays of the particles. The MWPC1 and MWPC2 reproduce only the x trajectory of the incoming particles and are utilized as a second level trigger. MWPC3 and MWPC4 determine both x and y rays of secondly scattered protons. The specifications of the proportional chambers is listed in the Table 3.3. As analyzer a 9 mm thick carbon slab with a density of 1.7 g/cm^3 was applied. MWPC1 and MWPC2 consist only of one X plane, while MWPC3 and MWPC4 additionally include two more anode wire planes: U and V, tilted by -45° and +45° relative to the X plane, respectively. The wire configuration is shown in Fig. 3.5. High voltage of -4.9 kV and -4.7 kV was applied to MWPC1,2 and MWPC3,4, respectively. The chambers were filled with the mixture of argon (66%), iso-butane (33%) and freon (0.3%) gas. The hodoscope contained two parts: HS-X which includes eight plastic scintillation detectors and HS-Y which consists of five plastic scintillators. For 0° measurements HS-Y and one detector from the high-momentum side of the HS-X were removed in order to enable the installation of the beam duct. The PS2 scintillator was placed in front of the carbon analyzer and used as a trigger.

3.5 Readout electronics

The trigger signals of the GR spectrometer were generated by signals from the plastic scintillator at the focal plane. For the polarization measurements using FPP, triggers were generated by

Tab. 3.3: Specifications of the multiwire proportional chambers of FPP

	MWPC1,2	MWPC3	MWPC4
Active area, mm^2	$760^W \times 200^H$	$1400^W \times 418^H$	$1400^W \times 600^H$
Number of wires	384	704(X), 640(U,V)	704(X,U,V)
Cathode	10 μm carbon-aramid		6 μm aluminized mylar
Wire configuration	X(0°)	X(0°), U(-45°), V(+45°)	
Applied voltage	-4.9 kV	-4.7 kV	
Anode-cathode gap	6 mm		
Sense wire spacing	2 mm		
Sense wires	25 μm ∅ gold-plated tungsten wire		
Gas mixture	Argon(66%)+Iso-butane(33%)+Freon(0.3%)+Isopropyl-alcohol		
Pre-amplifier	LeCroy 2735DC and Nanometric N277-C3		
Digitizer	LeCroy PCOS III		

coincidence signals from the PS1 at the focal plane and PS2 in front of the carbon slab. For the efficient data acquisition during polarization coefficients measurements the second-level trigger was employed [150]. It selected events with a second scattering angle at the analyzer block larger than 5°, because the analyzing power at very forward angles is small. The trigger system was applied in four universal logic modules units (LeCroy 2366), which used field-programmable gate arrays (FPGA). Data acquisition system based on memory modules in a VME crate was used for events collection. The block diagram of the data acquisition (DAQ) system [151] for the focal plane detectors of the GR spectrometer is illustrated in Fig. 3.6. Data taken in the present

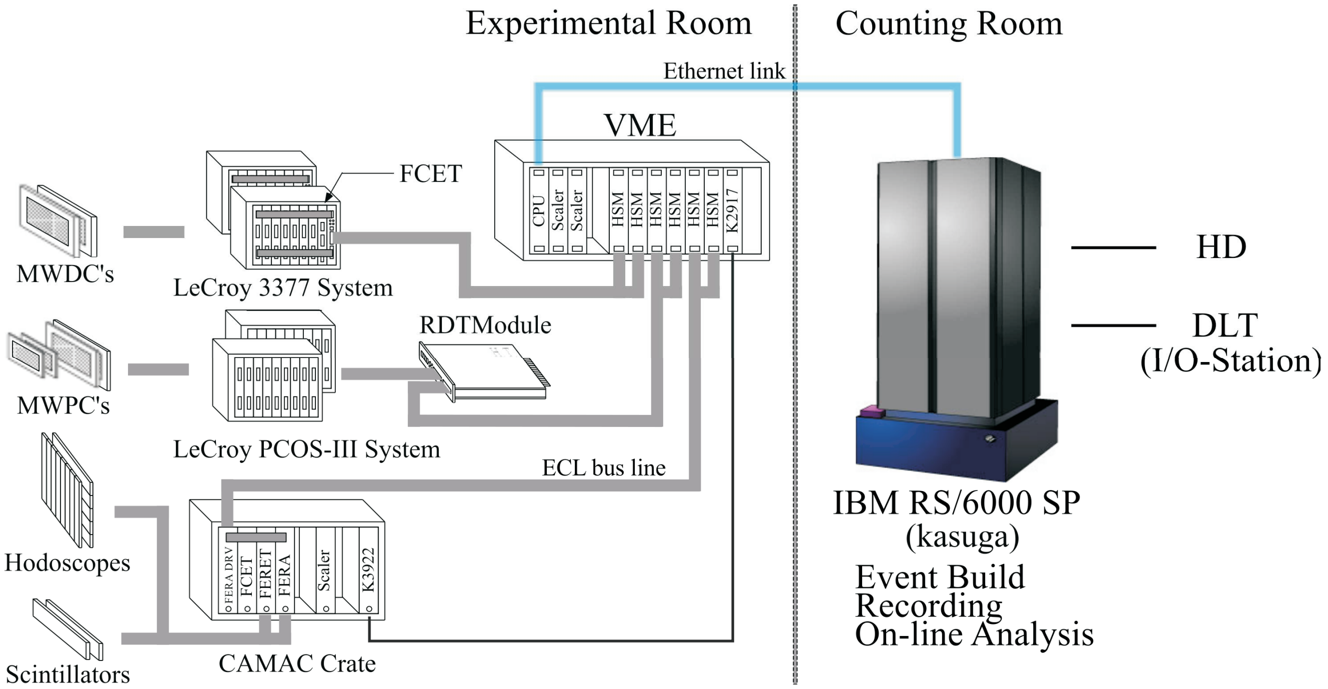

Fig. 3.6: Schematic view of the data acquisition system.

experiment consisted of electron drift time from the MWDC and MWPC chambers and charge and timing signals from the scintillators and hodoscope. For the consistency of data flow, an event header, an event number, and input register words were added to every event by the Flow Controlling Event Tagger (FCET) [152]. The digitized data from each detector were transferred in parallel via an ECL bus to a high speed memory module (HSM) in the VME crate (Lecroy 1191 Dual Port Memory) without any management by a software. To reduce dead time to be caused by the data transfer, a pair of the memory modules were used as a double buffer. The typical live time fraction of the DAQ system was 90% for the GR detectors in the 0° measurement. The data stored in the HSM′ s were moved via a gigabit Ethernet to an IBM RS/6000SP work station.

3.6 Targets

A thin lead foil with an areal density of 5.2 mg/cm^2 and an isotopical enrichment ^{208}Pb larger than 99% was used during both periods of experiment in 2006 and 2008. A metallic gold foil with a thickness of 1.68 mg/cm^2 was utilized for the beam tuning and beam energy-spread check in the achromatic transport mode. For tests of a possible beam halo faint beam measurements with an empty target frame was used. The calibration of the focal plane polarimeter was performed with a ^{12}C target with a thickness of 30 mg/cm^2. Also during the second part of the experiment in November of 2008, independent measurements with a ^{120}Sn target ($t = 6.5$ mg/cm^2) were performed. A ^{208}Pb target with thickness 60.4 mg/cm^2 and a ^{58}Ni one with thickness 100.1 mg/cm^2 were used for the GR optics calibration, by sieve-slit measurements in 2006 and 2008, respectively.

3.7 Beam tuning

For the inelastic scattering experiments at forward angles including 0°, a high quality beam is mandatory, since beam halo causes a huge amount of the background events in the detectors. One of the major requirements for high quality of the beam is a stable single-turn beam extraction from both AVF and ring cyclotrons. A detailed description of the cyclotron system optimization procedure can be found elsewhere [74]. In the experiments after single-turn extraction from the ring cyclotron the beam was delivered to the target via the WS beam line. First, the polarization axis was adjusted to the requested direction (sideways or longitudinal) by changing magnetic fields of SOL1 and SOL2. This process was controlled by the beam line polarimeters. In the beginning, an achromatic transport mode was used by looking at the elastic scattering on ^{197}Au at 8°. The proton beam was tuned to achieve the smallest energy spread. An optimum energy resolution of about 35 keV(FWHM) was realized, as illustrated in the left panel in Fig. 3.7. Typically an energy resolution of 40-60 keV is sufficient, corresponding to a horizontal beam size of 3 - 5 mm in the dispersive transportation mode. A small energy spread of the beam is necessary for low-background measurements. As a next step, halo-free tuning of the beam was performed. After delivering the beam to the 0° beam dump, accelerator elements were adjusted to achieve trigger counting rate on the PS1 without a target in the beam as small as possible. In the beam line from ring cyclotron to the target no slits were used to avoid any additional source of background events. After a receiving halo-free beam, the mode of transportation was changed to dispersive. The faint beam method [147] was utilized to achieve the dispersion matching conditions. A faint beam with an intensity of about 10^3 particles/s passed along the central orbit of the Grand Raiden. At such a rate the full profile of the beam can be seen in the focal plane detectors. Angular and lateral dispersion matching conditions were realized by changing quadrupole fields in the WS beam course to minimize the spatial and angular spread of the primary beam at the focal plane. An energy resolution better than 10 keV could be achieved. During the experiment 14 keV at FWHM in the elastic scattering on ^{197}Au at 0° were

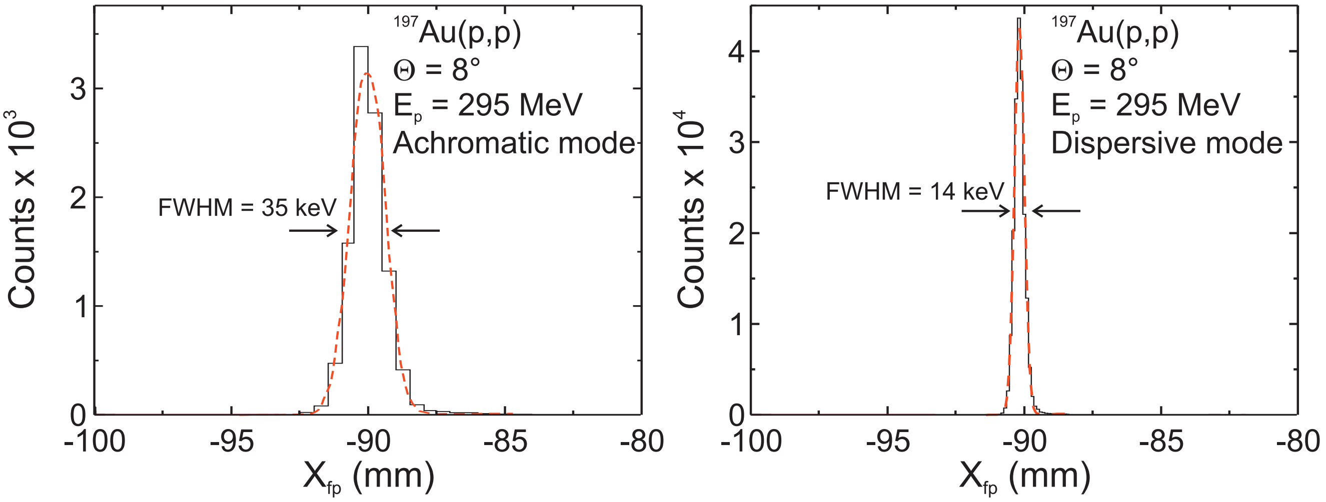

Fig. 3.7: Elastic scattering from a ^{197}Au target in the achromatic mode (l.h.s) at 8° and in the dispersive mode (r.h.s.) at 8°. The best energy resolution of 35 keV and 14 keV in the achromatic and dispersive mode, respectively, is achieved.

obtained, as shown on the right plot in Fig. 3.7. After setting the matching conditions, fields of all magnets, except the dipoles, in the WS beam line were fixed during the experiment to keep the matching conditions. It took about two days to perform the successful tuning of the proton beam to be able to perform high resolution measurements at 0°.

3.8 Calibration of Faraday cups

In order to assure correct charge collection during the experiment, the beam transmission from the target to the 0° beam dump was checked. For this purpose, collected charge at the 0° and at the scattering chamber Faraday cups (SC-FC) were compared, as the absolute efficiency for the charge collection by the SC-FC has been calibrated [153]. Due to impossibility of simultaneous measurements, an indirect test was made. It was based on the proportionality of the BLPs trigger rate to the beam charge, and the factor of the proportionality was compared to that of the SC-FC. After the SC-FC was removed, the similar proportionality between BLP and 0°-FC was established. The difference in the factors for both Faraday cups was due to the beam loss between them. The same procedure was also done between Faraday cups at the scattering chamber and Q1 magnet.

3.9 Ion optics of the Grand Raiden

3.9.1 Underfocus mode

In order to avoid additional production of the background events, no entrance collimator for a determination of the solid angle was used in the measurements at forward angles smaller than 6°. Thus, the track reconstruction of the scattered particles from the focal plane back to target position plays a crucial role for obtaining an angular resolution better than 1°. In 0° measurements the scattering angle resolution in both horizontal (dispersive) and vertical (non-dispersive) planes plays an important role. Their relationship at 0° can be written as $\Theta_{fp} = \sqrt{\Theta_t^2 + \phi_t^2}$, where Θ_{fp} is a total scattering angle at the focal plane and Θ_t and ϕ_t are horizontal and vertical scattering angles at the target place, respectively. With normal field settings of the

GR magnets, vertical and horizontal trajectories of the scattered particles were focused at the focal plane. But due to the small vertical magnification factor of the Grand Raiden (see. Tab. 3.1) of 5.98, the vertical scattering angle resolution becomes worse than 20 mrad. In order not to lose large vertical angle acceptance of the spectrometer a vertically off-focus mode (overfocus or underfocus) was applied by changing the magnetic field of the quadrupole Q1 of the Grand Raiden. Schemes of the possible focusing modes are shown in Fig. 3.8. During the present experiment a mild underfocus mode was chosen because of the larger horizontal and vertical scattering angle correlation at the focal plane in an overfocus mode. Thus, the magnetic field of Q1 quadrupole was decreased by 5% relative to the normally-focus mode. The underfocus mode also provides a method for background subtraction as will be discussed in Sec. 4.6.

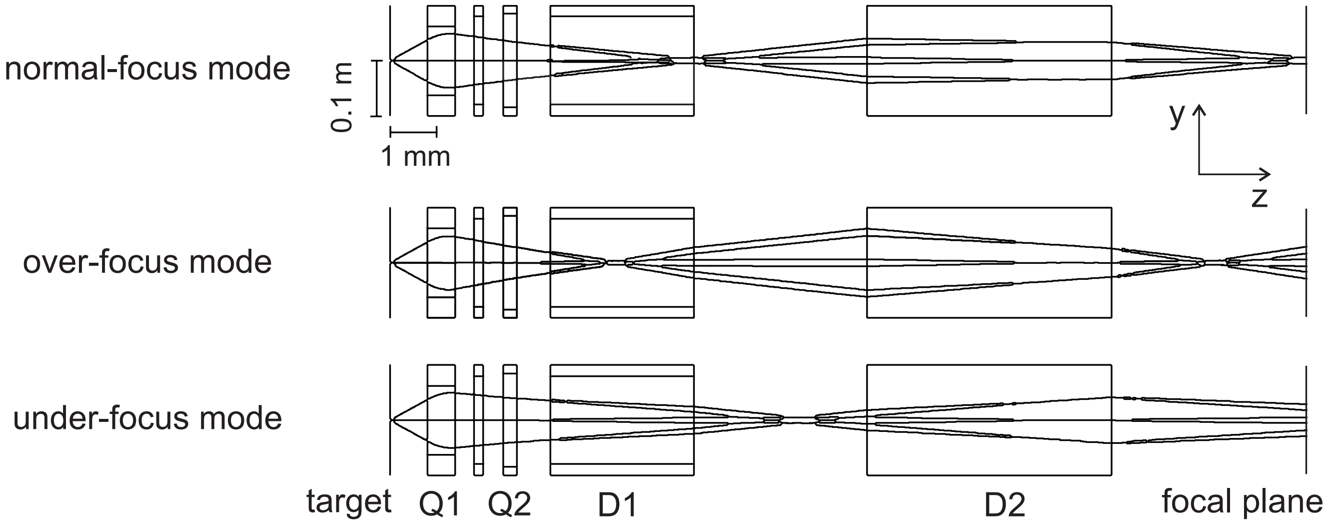

Fig. 3.8: The vertical beam trajectories in the y-z plane for scattered particles with ϕ_{tgt}=0,±46 mrad and y_{tgt}=±1 mm in three different focus modes of GR optics.

3.9.2 Sieve slit measurements

In order to reconstruct scattering angles at the target position from the scattering information gathered by the focal plane detectors one has to perform a calibration of the ion optics of the Grand Raiden spectrometer. So-called sieve slit measurements were done for this purpose. A 5 mm thick brass plate with 25 holes was placed at the entrance of the Grand Raiden. All holes in the brass plate were aligned as 5 (horizonal) x 5 (vertical) as shown in Fig. 3.9. For a better positioning the central hole had a diameter of 3 mm, which corresponds to 4.7 mrad in the scattering angle, while all other were 2 mm (3.1 mrad) in diameter. The distance between two horizontal holes was of 4.5 mm (7 mrad) and the distance between two vertical holes – 12 mm (19 mrad). The slit was placed 638 mm downstream of the target position. As targets, thick foils of ^{208}Pb with areal density 60.4 mg/cm^2 and ^{58}Ni with 100 mg/cm^2 were used in October of 2006 and November of 2008, respectively. For the measurements, Grand Raiden was rotated to 12° in 2006 or 16° in 2008. The protons scattered through a slit were detected at the focal plane. So, the vertical position and the scattering angle at the focal plane can be associated with the scattering angle at the target position based on the distance between holes and the target. During the measurements an achromatic transport mode of the beam was used. In order to investigate the dependence of the scattering angles on the horizontal position at the focal plane, the magnetic fields of all magnets were changed by +1.2%, +1.8%, 2.6%, 3.4% and +4.2% relative to the standard underfocus setting of the ion optics. It corresponds to the excitation

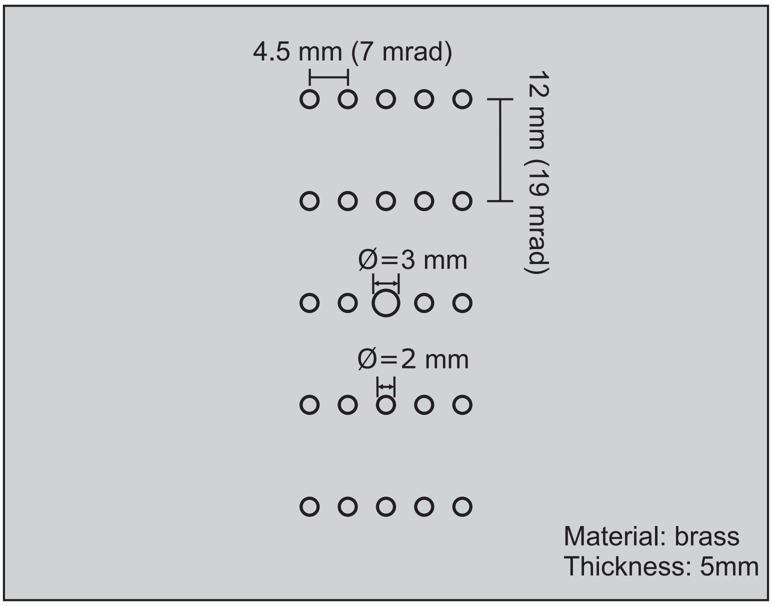

Fig. 3.9: Schematic layout of the sieve slit plate

energies of about 6, 10, 14, 18, 22 MeV in (p,p′) at 0°. So, the full excitation energy range of the experiment could be covered. To analyze the dependence on the beam position on the target, the beam spot was intentionally vertically shifted by 1 mm in both directions. In total, fifteen sets of data were taken during the measurements with the sieve slit. The analysis of the sieve slit measurements is presented in Sec. 4.3.

4 Data analysis

The program code ANALYZER [150, 154], was used to perform the data analysis. It was developed at the RCNP for the processing, of data taken by GR and LAS spectrometers, utilizing HBOOK and PAW++ program packages from CERN libraries [155]. The data reduction procedure includes the following important parts

- particle identification,
- reconstruction of the particle track information and drift time correction,
- determination of the detector efficiency,
- reconstruction of the scattering angle,
- beam polarization determination,
- correction of high-order abberations of the GR spectrometer,
- background subtraction,
- excitation energy calibration, and
- normalization of the excitation energy spectrum.

These topics will be discussed in this section step-by-step.

4.1 Particle identification

In the proton induced experiments at very forward angles inelastic scattering dominates but transfer reactions leading to other light ions are possible in principle. The particle identification was performed using time-of-flight (TOF) data and information about particle energy loss ΔE in the plastic scintillator counter PS1. The most like particles contributing to the background events were deuterons. As expressed in Bethe-Bloch formula (see e.g. [156]), the energy loss of a particle in material depends on its charge and velocity. In a scintillator, the pulse-height signal of a photomultiplier (PM) is dependent on the intersection point of the particle with the scintillator, as the light attenuates while passaging the detector to the photomultiplier. A readout at both ends of the scintillator provides a mean ΔE value independent of the position. The two-dimensional plot in the ΔE(PS1) - TOF plane is shown in Fig. 4.1. Scattered protons are clearly seen and marked with a solid line, predicted positions of the deuterons are illustrated with a dashed line. Background events caused by deuterons were not seen in the present measurement.

4.2 VDC data reconstruction

4.2.1 Drift time to length conversion

In Fig. 4.2 the wire configuration and working principle of the reconstruction of the intersection point is schematically illustrated. All dimensions correspond to the parameters of the VDC chambers at the GR spectrometer. The VDC includes two cathode foils and many anode-plane wires. There are two different types of anode wires, viz. sense or signal wires and field or potential wires. The potential wires provide the required field shaping and hinder possible cross talk between different channels. Field lines for the sense wires are also shown in Fig. 4.2. Charged

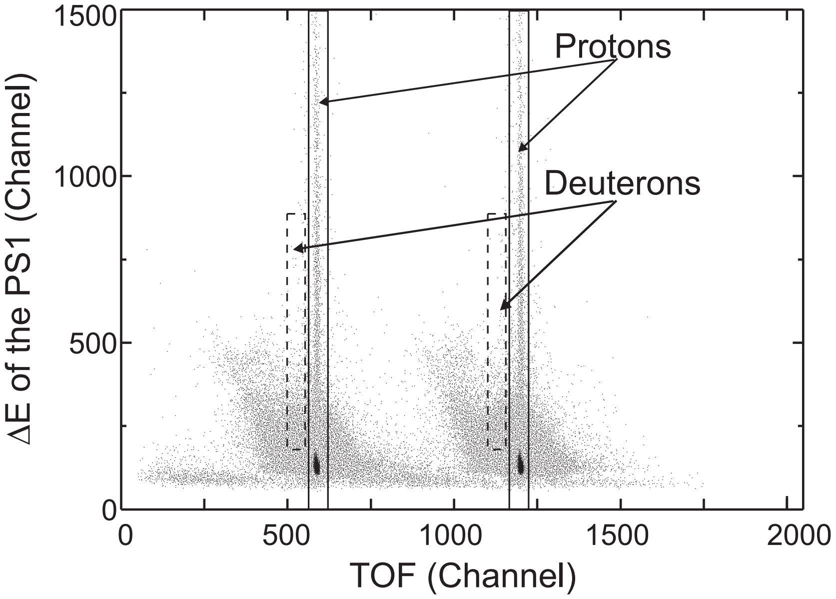

Fig. 4.1: A typical scatter plot of the particle selection for protons enclosed by the solid line. The deuterons are not seen in the predicted region. Predicted area for deuterons are shown with dashed line.

particles passing through the detector collide with atoms and molecules of the working gas and ionize them. The created ion-electron pairs drift in the electric field. The electrons are accelerated toward the anode plane. The electron drift velocity remains almost constant at the applied high voltage and amount to ≈5cm/μs for the chosen gas mixture. Hence, the electron drift time is proportional to the distance from the point of ionization to the the wire and it is possible to rebuild the trajectory if enough wires provide a signal. Time difference between the wire signal and the delayed trigger signal from PS1 is measured by Time-to-Digital Convertors (TDCs). In order to reconstruct particle rays one has to convert the TDC values into the distances between corresponding sense wires and the track measured along the arrow, as indicated in Fig. 4.2. In order to perform this drift time conversion to a drift length, a white spectrum with homogenously distributed events was measured. The conversion of the drift time to distance is illustrated in

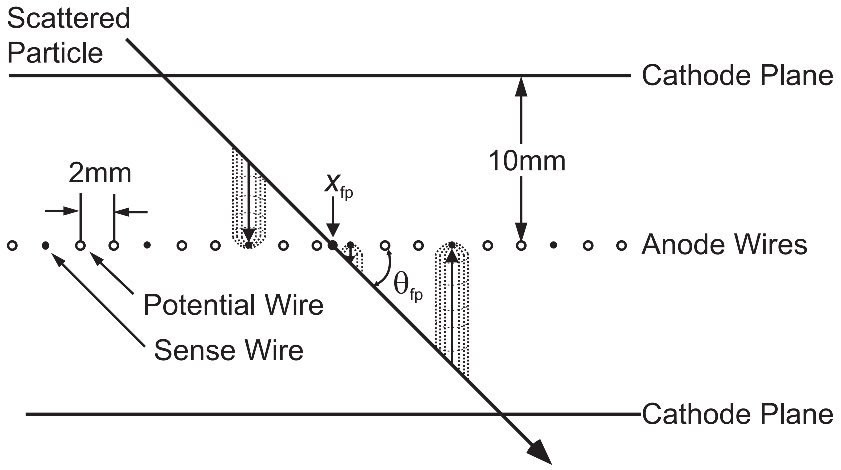

Fig. 4.2: Grand Raiden wires configuration. Drift lines are shown for sense wires, arrows inside demonstrate corrected drift distances.

Fig. 4.3. For the white spectrum the drift length spectrum (l.h.s.) has a flat distribution. Right panel shows the proportionality between TDC channels and the drift length. Due to the field inhomogeneity close to the wires the proportionality is broken. Usually particles cross the chamber under an angle of 45° and provide signal from three sense wires at a time. Neighboring events were grouped as clusters, and clusters with only one hit were neglected. The signal from the wire with the shortest signal (the shortest drift time) was omitted, due to electric field properties in the vicinity of the sense wires that cause uncertainty in the drift length determination. It was assumed that each plane has only one cluster. The intersection point of the trajectory at the wire plane was calculated by a least-square fitting from the drift length of hit wires. Combining information from all wire planes one is able to determine the full track and the scattering angle of the particles.

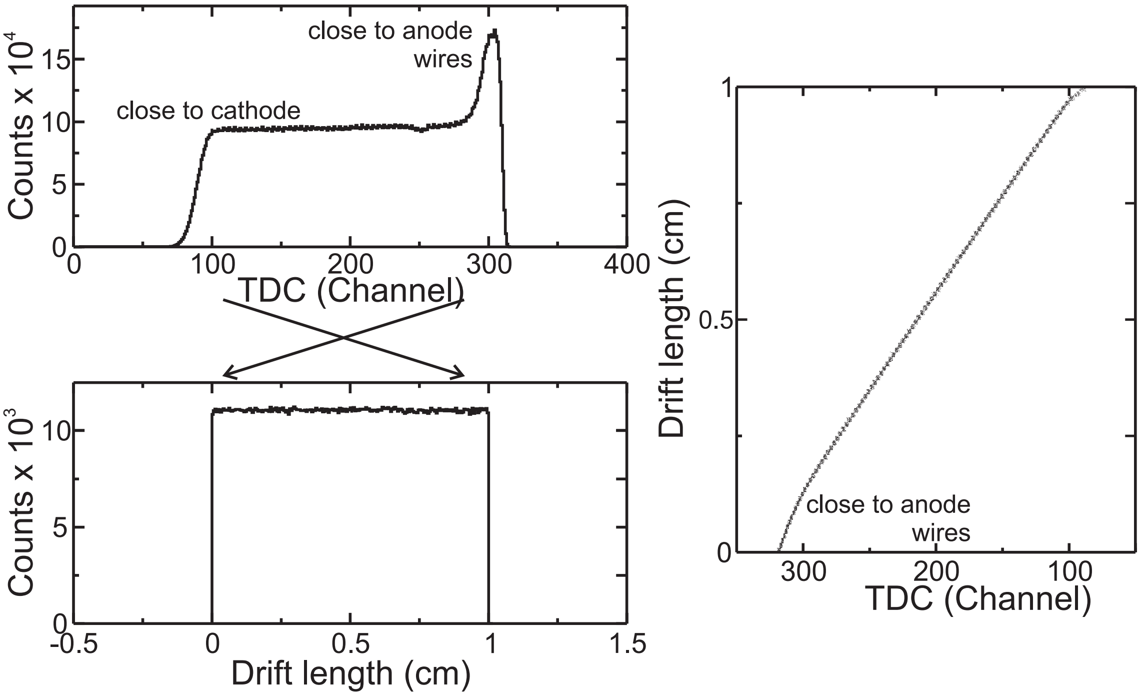

Fig. 4.3: Conversion of the TDC signals to drift length. As an example a spectrum from the X1 plane is shown.

4.2.2 Efficiency of the MWDCs

The detection efficiency of each wire plane was obtained as the ratio between the number of events, for which intersection positions were successfully determined for four wire planes, and the number of events for the other three planes as shown in Eq. (4.1) for the example of the X1 plane

$$\epsilon_{X1} = \frac{N_{X1X2U1U2}}{N_{X1X2U1U2} + N_{\overline{X1}X2U1U2}}, \tag{4.1}$$

where $N_{X1X2U1U2}$ stands for the number of events where the intersection position was determined for all four planes and $N_{\overline{X1}X2U1U2}$ is the number where intersection position was determined in all planes except X1. The efficiencies for all four wire planes were calculated to be in the order 95-98%. The full tracking efficiency was calculated as a product of efficiencies of all four planes:

$$\epsilon_{total} = \epsilon_{X1} \cdot \epsilon_{X2} \cdot \epsilon_{U1} \cdot \epsilon_{U2} \tag{4.2}$$

The total efficiency was about 90% during the whole experiment.

4.3 Calibration of the scattering angle

Using the data from the sieve slit measurements (see Sec. 3.9.2) horizontal and vertical scattering angles in the acceptance of the GR spectrometer were calibrated. The horizontal scattering angle Θ_t at the target position was mainly determined from the horizontal incident angle θ_{fp} at the focal plane. As has been shown in the Sec. 3.9.1 the off-focus mode provides conditions conditions such that the vertical scattering angle Φ_t can be defined mainly from the vertical position y_{fp} at the focal plane. A similar correlation between Θ_t and the horizontal position at the focal plane x_{fp} and the vertical beam spot position y_{LAS} on the target exists. Using the sieve slit measurements one is able to establish these dependencies. The elastic scattering events can be seen in Fig. 4.4(a). The shadowed area highlights the gate on the x_{fp} used for the analysis. The vertical position of the beam monitored by LAS is illustrated in Fig. 4.4(b). Figure 4.5(a) shows two-dimensional images of the sieve slit data in the y_{fp}-θ_{fp} plane after applying the gate shown in Fig. 4.4(a). The aim is to determine two coordinates of the center of all spots. For this purpose, all events were projected on the y_{fp} axis and then on the θ_{fp} axis. Utilizing Gaussian fits all central positions were obtained, assuming a round shape of the hole images. In order to determine ϕ_{fp}, as shown in Fig. 4.5(b), the two-dimensional plot y_{fp}-ϕ_{fp} was analyzed. It was gated on elastic events and on the specific θ_{fp} regions. As an example, the gate $|\ \theta_{fp}\ | \ \leq 8$ mrad was applied to the plot Fig. 4.5(b). To obtaine the central positions, events were projected on the ϕ_{fp} axes, and Gaussian fits were applied. Finally, Θ_t and Φ_t are determined with the following relations

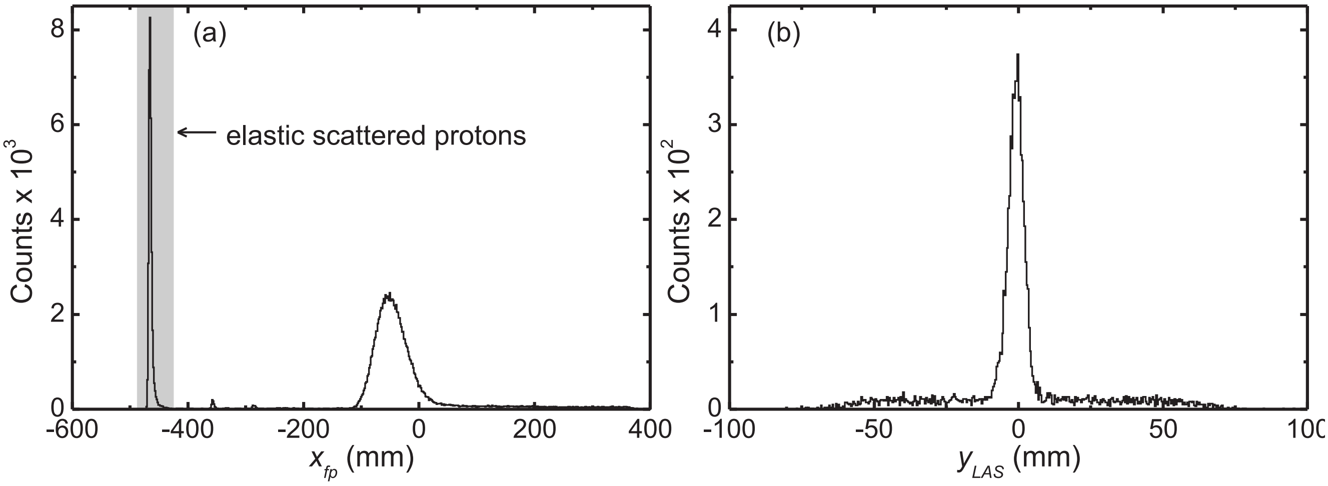

Fig. 4.4: (a) Gate on the elastically scattered proton events. (b) Vertical beam position on the target controlled by LAS.

$$\Theta_t(x_{fp}, \theta_{fp}) = \sum_{i=0}^{1}\sum_{j=0}^{1} a_{ij} \cdot x_{fp}^i \theta_{fp}^j, \tag{4.3}$$

$$\Phi_t(x_{fp}\theta_{fp}, y_{fp}, \phi_{fp}, y_{LAS}) = \sum_{i=0}^{1}\sum_{j=0}^{1}\sum_{k=0}^{1}\sum_{l=0}^{1} b_{ijkl} \cdot x_{fp}^i \theta_{fp}^j y_{fp}^k \phi_{fp}^l + \sum_{l=0}^{1} c_l \cdot x_{fp}^l y_{LAS}, \tag{4.4}$$

where y_{LAS} is the vertical position of the beam measured by the LAS and the coefficients a_{ij}, b_{ijkl}, c_l results from a multi-dimensional least-square fit routine of the sieve slit data utilizing the GNU science library [157]. Results of the fitting procedure are presented in Tab. 4.1. The scattering

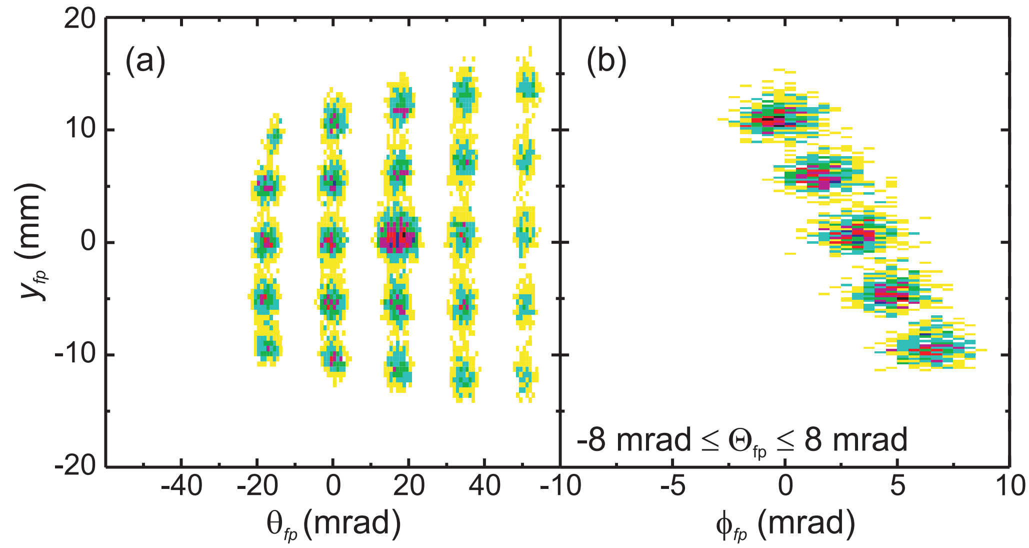

Fig. 4.5: (a) Two-dimensional plots of the elastic scattering events in the (a) y_{fp}-θ_{fp} plane and (b) in the y_{fp}-ϕ_{fp} plane gated on θ_{fp}.

angle calibration is presented in Fig. 4.6, which shows the reconstruction of the sieve slit holes after employing the calibration functions from Eqs. (4.3) and (4.4) for different magnetic field values corresponding to excitation energies $E_x \approx 6$, 9 and 16 MeV. Clearly the reconstruction of the scattering angle works well over the whole momentum acceptance range. The horizontal and vertical scattering angle resolution was estimated from the fitting results for each hole of the sieve slit. The horizontal angular resolution was 0.15° (FWHM), while the vertical angular resolution was of about 0.5° - 0.6° (FWHM) depending on x_{fp}. Systematic uncertainties in the

Tab. 4.1: Coefficients table for Eqs. (4.3) and (4.4).

ij	a_{ij} for mag1	a_{ij} for mag2
00	$1.344 \cdot 10^{-3}$	$1.731 \cdot 10^{-3}$
01	$-3.328 \cdot 10^{-1}$	$-4.180 \cdot 10^{-1}$
10	$5.132 \cdot 10^{-6}$	$2.393 \cdot 10^{-5}$
$ijkl$	b_{ijkl} for mag1	b_{ijkl} for mag.2
0000	$-8.093 \cdot 10^{-3}$	$-6.505 \cdot 10^{-3}$
0001	4.518	3.827
0010	$-1.546 \cdot 10^{-4}$	$-2.159 \cdot 10^{-3}$
1000	$3.154 \cdot 10^{-5}$	$1.227 \cdot 10^{-5}$
l	c_l for mag1	c_l for mag2
0	$-6.744 \cdot 10^{-4} \cdot y_{LAS}$	$-1.239 \cdot 10^{-3} \cdot y_{LAS}$
1	$-8.083 \cdot 10^{-7} \cdot y_{LAS}$	$6.652 \cdot 10^{-7} \cdot y_{LAS}$

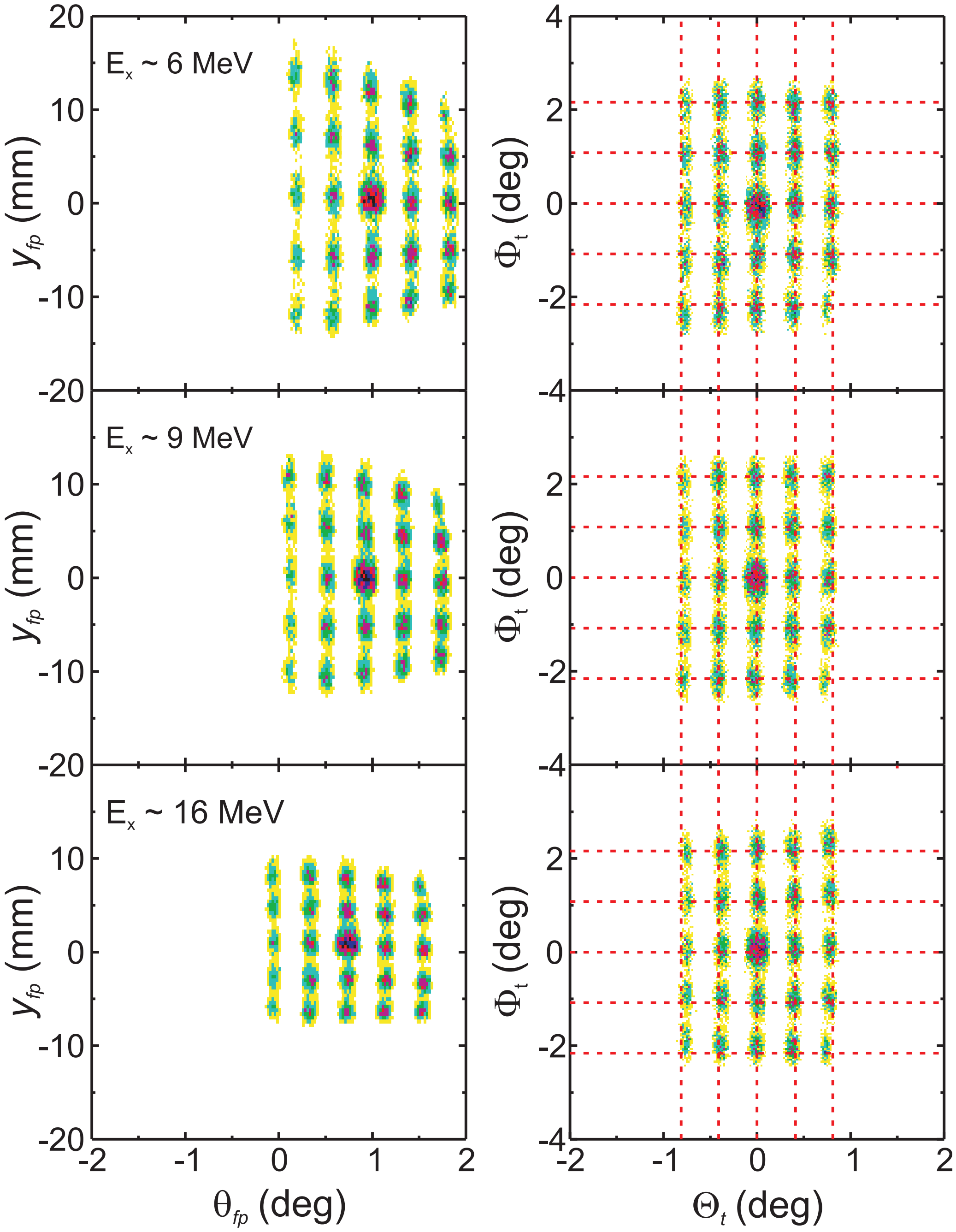

Fig. 4.6: Two dimensional plots in the $y - \theta$ plane before (l.h.s.) and after corrections (r.h.s.). Data are shown for three different excitation energy regions: 6 MeV, 9 MeV, 16 MeV in the top, middle and bottom panels, respectively. The intersections of the dashed lines in the right plots correspond to the geometric position of the sieve slit holes.

determination of the scattering angles were calculated from the average deviation from the correct values for all spot centers. They were less than 0.1° and 0.3° for horizontal and vertical scattering angles, respectively.

4.4 Beam polarization

All three p_S, p_N and p_L components of the beam polarization vector were extracted from the BLP data. In order to remove the instrumental asymmetries, the beam polarization was periodically flipped between spin-up (↑) and spin-down (↓). Thus, the beam polarization at the BLP can be extracted using equations

$$p_{\mathrm{N}}^{\uparrow(\downarrow)} = \frac{1}{A_y^{BLP}} \cdot \frac{N_{\mathrm{L}}^{\uparrow(\downarrow)} - N_{\mathrm{R}}^{\uparrow(\downarrow)}}{N_{\mathrm{L}}^{\uparrow(\downarrow)} + N_{\mathrm{R}}^{\uparrow(\downarrow)}}, \tag{4.5}$$

$$p_{\mathrm{S}}^{\uparrow(\downarrow)} = \frac{1}{A_y^{BLP}} \cdot \frac{N_{\mathrm{D}}^{\uparrow(\downarrow)} - N_{\mathrm{U}}^{\uparrow(\downarrow)}}{N_{\mathrm{D}}^{\uparrow(\downarrow)} + N_{\mathrm{U}}^{\uparrow(\downarrow)}}, \tag{4.6}$$

where $\mathrm{N}_{\mathrm{L(R)}}^{\uparrow(\downarrow)}$ are numbers of coincident events collected by the L-L′ (R-R′) detector pairs with spin-up (spin-down) beam polarization, $\mathrm{N}_{\mathrm{D(U)}}^{\uparrow(\downarrow)}$ is the same but for D-D′ (U-U′) detector pairs and A_y^{BLP} is the analyzing power of proton elastic scattering on the BLP target. With the assumption p↑=-p↓ Eqs. (4.5) and (4.6) can be rewritten as

$$p_{\mathrm{N(S)}} = \frac{1}{A_y^{BLP}} \cdot \frac{X_{\mathrm{N(S)}} - 1}{X_{\mathrm{N(S)}} + 1}, \tag{4.7}$$

where

$$X_{\mathrm{N(S)}} = \sqrt{\frac{N_{\mathrm{L(U)}}^{\uparrow} N_{\mathrm{R(D)}}^{\downarrow}}{N_{\mathrm{L(U)}}^{\downarrow} N_{\mathrm{R(D)}}^{\uparrow}}}. \tag{4.8}$$

The three components of the beam polarization vector at the target can be determined from the polarizations measured by BLP1 ($\mathrm{p}_{\mathrm{N}}^{1}$, $\mathrm{p}_{\mathrm{S}}^{1}$)) and BLP2 ($\mathrm{p}_{\mathrm{N}}^{2}$, $\mathrm{p}_{\mathrm{S}}^{2}$) by the relation

$$p_{\mathrm{N}} = p_{\mathrm{N}}^{1} = p_{\mathrm{N}}^{2}, \tag{4.9}$$

$$p_{\mathrm{S}} = p_{\mathrm{S}}^{1}, \tag{4.10}$$

$$p_{\mathrm{L}} = (p_{\mathrm{S}}^{1} \cos\chi - p_{\mathrm{S}}^{2}) / \sin\chi, \tag{4.11}$$

where χ is the spin precession angle at the bending section between two BLPs and determined from

$$\chi = \gamma \cdot (\frac{g_p}{2} - 1) \cdot \theta_{BLP}. \tag{4.12}$$

Here, γ is the proton Lorentz factor, g_p the proton g-factor and θ_{BLP} (=115°) is the relative angle between BLP1 and BLP2. The values of the beam polarization components from the measurements in 2006 and 2008 are summarized in Tab. 4.2. In Fig. 4.7 the dependence of the extracted total beam polarization for the two periods of the experiment, in October 2006 (l.h.s.) and in November 2008 (r.h.s.) is illustrated. On average a polarization of about 73% and 67% was reached during the first and second period, respectively.

Tab. 4.2: Beam polarization components.

Year	p_S	p_L
2006	0.682	0.042
2008	0.026	-0.659

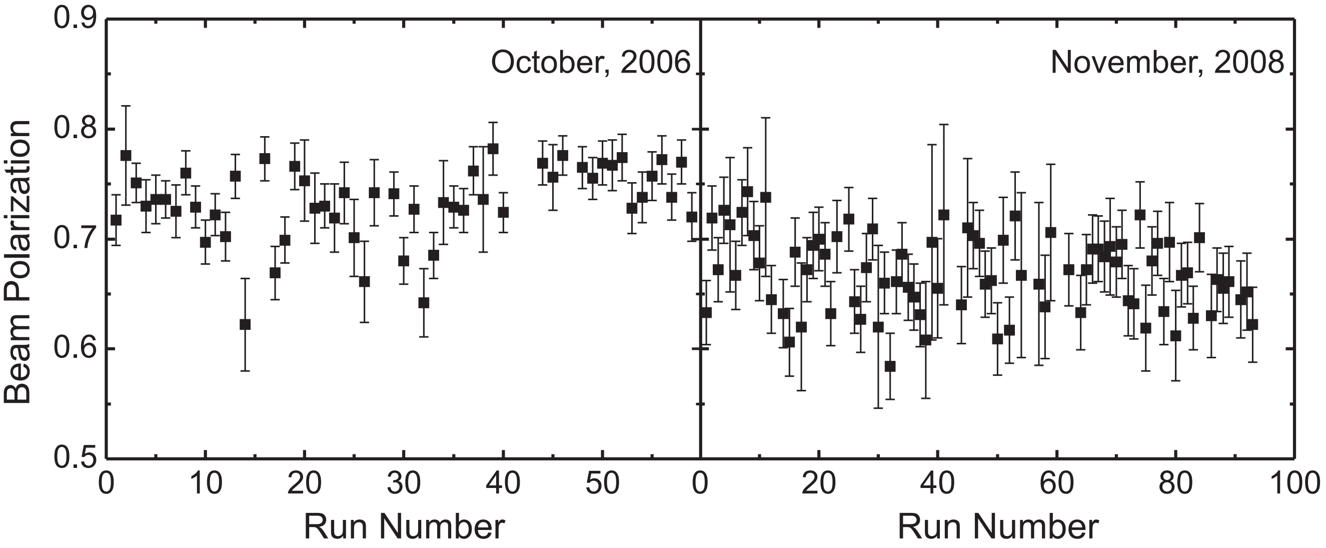

Fig. 4.7: Time dependence of the total beam polarization in the measurements at 0°in October, 2006 (left plot) and in the November, 2008 (right plot).

4.5 Correction of the higher-order aberrations

Even though matching conditions between the beam transport line and the Grand Raiden spectrometer were set up, some additional off-line corrections were necessary to obtain optimum energy resolution. There are two different reasons for these corrections: a kinematical dependence of the proton momentum on the scattering angle and ion-optics properties of the spectrometer. Because of the latter, the reconstruction of the proton momentum from x_{fp} has a small dependence on the values of θ_{fp} and y_{fp}. From the very beginning the proton momentum was corrected on the kinematic recoil effects. The remaining dependencies were eliminated as follows. A measurements with a ^{28}Si target at 0° was performed exciting several strong well-known discrete transitions in the excitation energy region from 5 MeV to 15 MeV. The upper part of Fig. 4.8 displays typical line shapes of these transitions in the x_{fp}-θ_{fp} plane, where the reason for the limited energy resolution is obvious. The dependence on y_{fp} was found to be negligible as expected from the optical design of the Grand Raiden. Corrected positions x_c were obtained from

$$x_c = \sum_{i=0}^{1} \sum_{j=0}^{4} d_{ij} \cdot x_{fp}^{i} \theta_{fp}^{j}. \tag{4.13}$$

The indices i and j corresponds to the order of the polynomial used in the fit and d_{ij} coefficients result from the least-square fit procedure. The results of the transformation are shown in the lower panel of Fig. 4.8. Clearly, the resolution in x_{fp} and thus the energy resolution is improved.

4.6 Background subtraction

Even with optimum experimental conditions and beam tuning, instrumental background events could still exist in the measured spectrum. They result mainly from multiple scattering of the protons in the target material. Because of the statistical origin of the multiple scattering, they show a flat distribution in the non-dispersive focal plane. In the normal magnetic field mode of the Grand Raiden, *true* events are focused in the y direction of the focal plane. Thus, it is easy to distinguish between true and background events. In the underfocus mode, such a focusing is

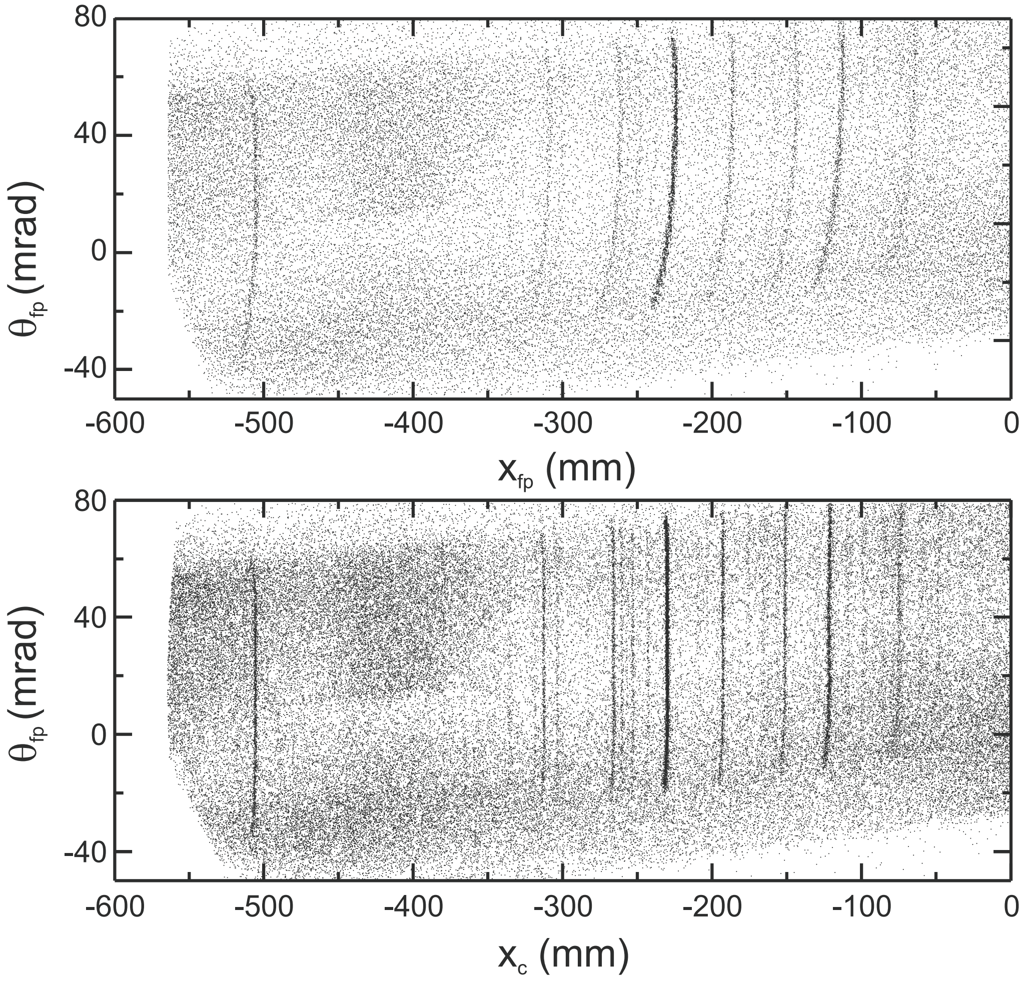

Fig. 4.8: Two-dimensional histograms of the x_{fp} and the horizontal scattering angle θ_{fp} for the ^{28}Si(p,p′) reaction at 0°before (top) and after (bottom) the software corrections.

lost. Therefore, a differentiation of the true and background events, requires a transformation of the coordinates in the non-dispersive plane to regain the correlation of the events with a y_{fp} value. The correction was performed utilizing the least-square method in the ϕ_{fp} - y_{fp} plane, including dependencies on x_{fp}, θ_{fp} and vertical position of the beam. For the fit procedure data obtained during the sieve slit measurements were used. The final relation to obtain corrected values is

$$y_c = y_{fp} + \sum_{i=0}^{1}\sum_{j=0}^{1}\sum_{k=0}^{1} f_{ijk} \cdot x^i_{fp}\theta^j_{fp}\phi^k_{fp} + f_l y_{LAS}, \tag{4.14}$$

where y_c is the corrected vertical coordinate, and f_{ijk} and f_l are fit parameters. The coefficients f_{ijk} and f_l are listed in Tab. 4.3. The results of the transformation in comparison with uncorrected histograms are illustrated in Fig. 4.9. True events are concentrated at y_c=0 while the distribution of background events is almost flat. Thus, one is able to remove the most part of the background events by setting a narrow y_c-gate around $y_c = 0$ (black hatched area in Fig. 4.10(a)). The contribution of the background can be estimated from the counts in the pure background regions on both sides of the peak (red hatched areas in Fig. 4.10(a). The spectra corresponding to the prompt and background gates in Fig. 4.10(a) are shown in Fig. 4.10(b). But if one looks in details, for example in small Φ_t cuts, one still finds correlations with y_c.

Tab. 4.3: Coefficients table for Eq. (4.14).

ijk	f_{ijk} for mag1	f_{ijk} for mag2
000	-4.34	$-9.12 \cdot 10^{-1}$
001	$1.36 \cdot 10^{3}$	$9.20 \cdot 10^{2}$
010	$1.88 \cdot 10^{1}$	$-3.53 \cdot 10^{1}$
011	$-1.16 \cdot 10^{3}$	$6.46 \cdot 10^{3}$
100	$4.30 \cdot 10^{-3}$	$1.12 \cdot 10^{-2}$
101	$-2.84 \cdot 10^{-1}$	-2.65
111	-6.56	$-1.03 \cdot 10^{1}$

l	f_l for mag1	f_l for mag2
0	$7.15 \cdot 10^{-1}$	$9.91 \cdot 10^{-1}$

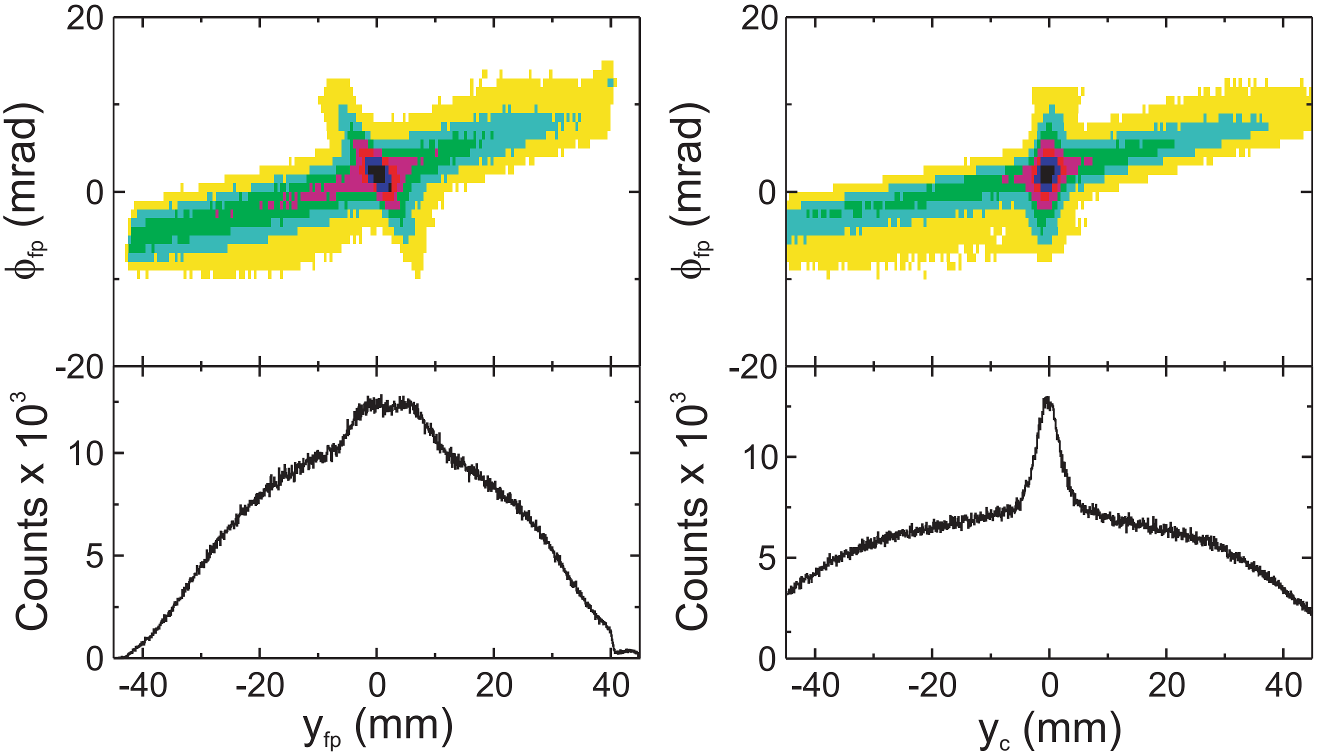

Fig. 4.9: Vertical scattering angle ϕ_{fp} versus vertical position y_{fp} and vertical position before (left panel) and after (right panel) the transformation performed by Eq. (4.14).

Taking into account the dependence of the Φ_t on y_{fp}, x_{fp} and on θ_{fp} from Eq. (4.4) one has to estimate the background as a function of the excitation energy for an angle cut in Θ_t. A new method of the background subtraction was developed, in order to eliminate this dependence on

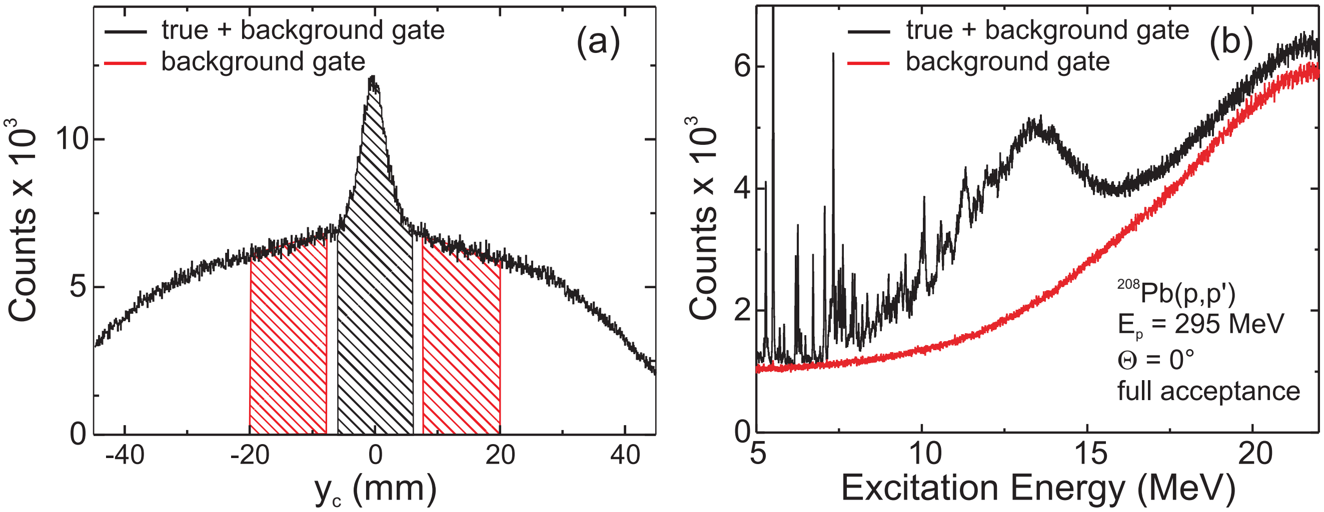

Fig. 4.10: (a) Corrected vertical position y_c with gates on prompt true + background signals (black hatched) and pure background (red hatched). (b) Excitation energy spectra that correspond to the gates from the plot (a).

the scattering angle. Firstly, the similar focusing transformation as for y_{fp} was performed for the ϕ_{fp}

$$\phi_c = \phi_{fp} + \sum_{i=0}^{1} e_i \cdot y_{fp}^{i} \,, \tag{4.15}$$

where e$_i$ are fitting parameters. The main idea of the new method is to utilize the homogeneity of background events in the ϕ_c - y_c plane in order to avoid ambiguities in the background estimation caused by complex correlations among all software gates. For that purpose, a set of data was created, with an artificial displacement of y$_{fp}$, simply adding a constant to y_{fp}, so that y$_c$ was shifted without changing ϕ_c. A second data set was created shifting y_c in the opposite direction as illustrated in Fig. 4.11. The optimum value of the displacement depends on the excitation energy. A criterion is that obtained background should be independent of the shift direction. A background spectrum was then created taking the average of two shifted data sets. An energy spectrum in the scattering angle region from 0° to 0.5° with the background estimated using the

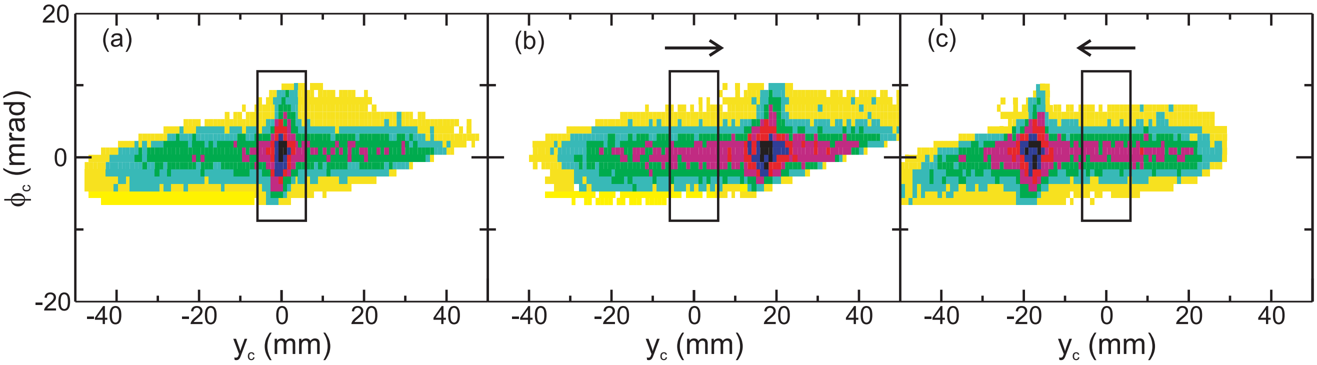

Fig. 4.11: Correlation of the corrected vertical position y_c and vertical incident scattering angle ϕ_c. Events selected by the gate are displayed with a box. The arrows show the direction of the shift.

second subtraction method is presented in Fig. 4.12. Spectra resulting after the background subtraction are illustrated in Fig. 4.13. In the left plot a spectrum collected in the full acceptance of

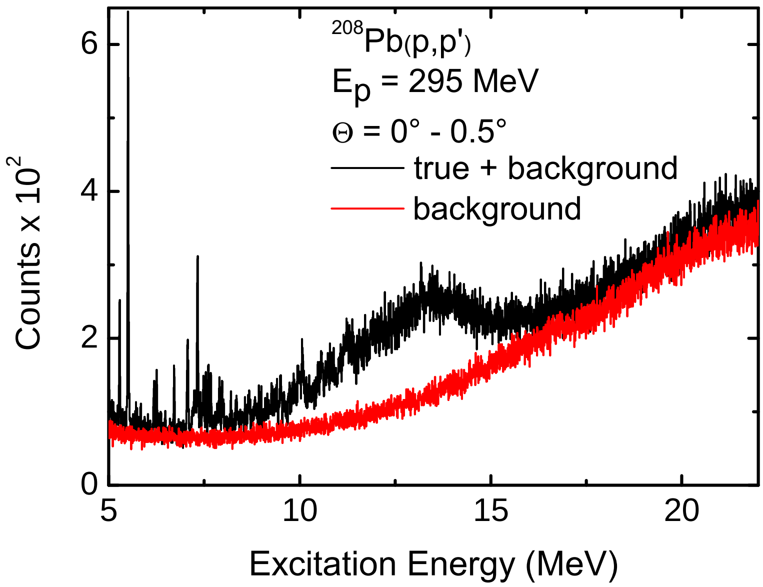

Fig. 4.12: Excitation energy spectrum created after the second correction in the scattering angle gate Θ=0° - 0.5° .

the Grand Raiden is presented and on the r.h.s. a spectrum gated on the scattering angle region from 0° to 0.5° can be seen. In the giant resonance region in both spectra a prominent bump coming from the Coulomb excitation of the GDR is observed. Because of the excellent energy resolution ΔE = 25 - 30 keV (FWHM), pronounced fine structure of the resonance is visible, a phenomenon now established as a global feature of giant resonances [82, 89].

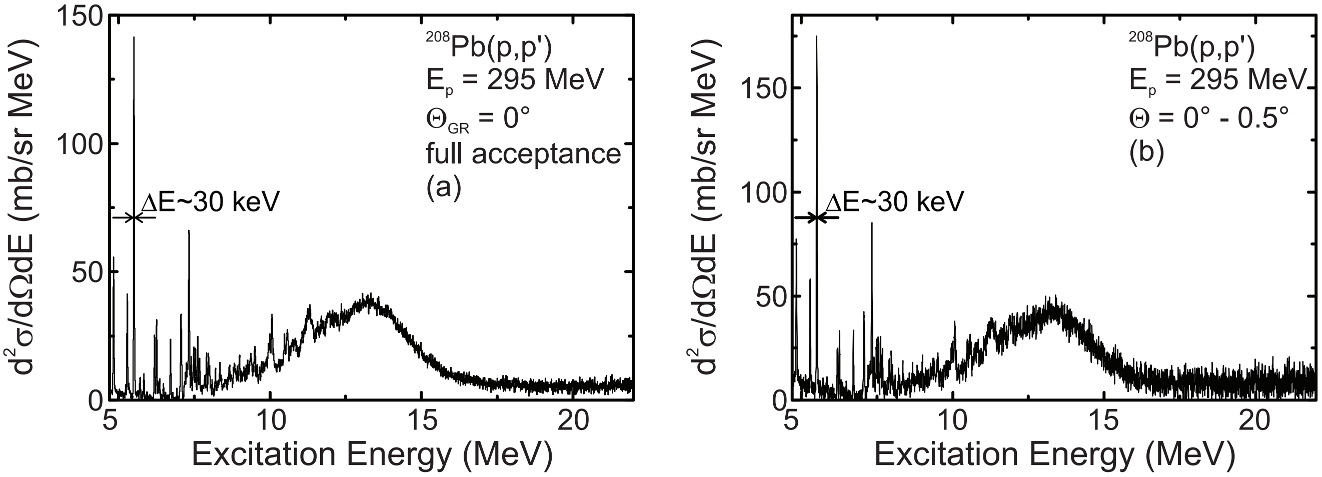

Fig. 4.13: Measured spectrum versus excitation energy created after background subtraction using two different subtraction procedures (a) in the full acceptance, (b) in the scattering angle cut Θ = 0° - 0.5°.

4.7 Excitation energy calibration

After all software corrections, the absolute excitation energy calibration can be performed. It is based on measurements of states with known excitation energies in ^{12}C, ^{26}Mg, ^{28}Si and

^{208}Pb [158]. The difference in the reaction kinematics for these nuclei was taken into account using the program KINMAT [159]. A polynomial dependence of the E$_x$ on x_c was assumed. The best fit results are achieved using a second-order polynomial function. Because of the slight shift in the beam energy or position from run to run, the energy calibration has to be performed for each run individually. The data sets were normalized to each other by requiring the position of the strongest peak in each ^{208}Pb spectrum at 5.512 MeV to coincide. The reference values from the known transitions are reconstructed with an accuracy of ±5 keV in the excitation energy region from 5 MeV to 12 MeV.

4.8 Cross section extraction

Double differential cross sections were calculated by the following equation

$$\frac{d^2\sigma}{d\Omega dE} = N_{counts}\frac{1}{\Omega_{lab}}\frac{1}{L\epsilon}\frac{e}{Q}\frac{A}{N_A t\eta}J, \tag{4.16}$$

where

N_{counts}	[counts/MeV]	- yield for the specific energy bin,
Ω_{lab}	[sr]	- solid angle in the laboratory frame,
L		- DAQ live time ratio,
ϵ		- detector efficiency,
e=1.6·10^{-19}	[C]	- elementary charge,
Q	[C]	- collected charge,
A	[g/mol]	- target atomic weight,
N_A=6.023·10^{23}	[1/mol]	- Avogadro number,
t	[g/cm^2]	- target thickness,
η		- target enrichment,
J		- Jacoby transformation from laboratory to the center of mass system.

In Fig. 4.14 double differential cross sections measured using the full acceptance of the Grand Raiden spectrometer in October, 2006 (a) and in November, 2008 (b) are plotted. In the top panels spectra collected with Grand Raiden placed at 0° are shown and in the bottom panels, with GR placed at 2.5°. There is generally very good agreement between the two data sets such that they can be combined for an analysis of cross sections. The difference in the spectra normalization between both runs is less than 3 %. The typical energy resolution of the spectra was between 25 - 30 keV. Present peaks at about 15 MeV are due to carbon contamination of the target (it corresponds to the well known 1$^+$ state at 15.11 MeV. in ^{12}C). Its contribution was estimated by smooth function and after that subtracted. The statistical and systematical uncertainties are deduced by the equations

$$\Delta\frac{d^2\sigma}{d\Omega dE}\bigg|_{stat} = \frac{1}{\sqrt{N_{counts}}}\frac{d^2\sigma}{d\Omega dE}, \tag{4.17}$$

$$\Delta\frac{d^2\sigma}{d\Omega dE}\bigg|_{sys} = \sqrt{\frac{\Delta\epsilon}{\epsilon}^2 + \frac{\Delta L}{L}^2 + \frac{\Delta t}{t}^2 + \frac{\Delta\Omega}{\Omega}^2 + \frac{\Delta Q}{Q}^2}\,\frac{d^2\sigma}{d\Omega dE}, \tag{4.18}$$

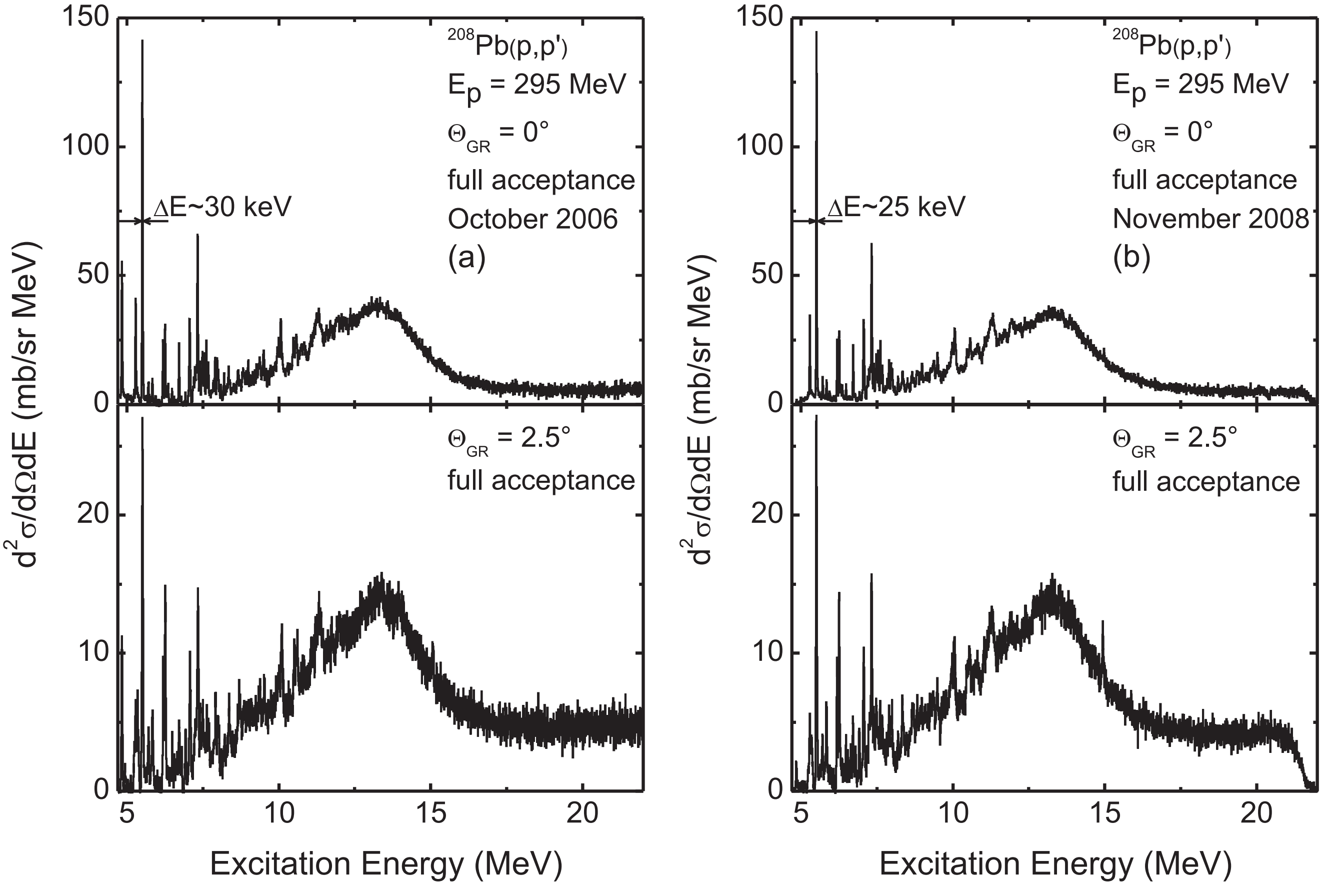

Fig. 4.14: Excitation energy spectra measured in October, 2006 (a) and in November, 2008 (b) using full acceptance of the Grand Raiden. Top panels: 0° setting of the spectrometer, bottom panels: 2.5° setting.

respectively. The major contribution to the systematic errors comes from the determination of the solid angle (≈ 5 - 8 %), collected charge (3 - 5 %) and target inhomogeneity (≈ 5 %). Thus, the systematic uncertainties are not larger than 10 %.

4.9 Spectrum decomposition

For a determination of the cross section of specific excitations, the energy spectrum was divided in two major parts. For excitation energies up to ∼7 MeV individual transitions could be resolved and the total number of events for each individual state was obtained with a peak fitting code HDTV [160], assuming a Gaussian peak function and a polynomial background.

$$f(x) = y_0 e^{-\frac{(x-E_0)^2}{2\sigma^2}} + \sum_i^n a_i x^n, \tag{4.19}$$

where y_0 denotes the peak height, σ represents the peak width, and E_0 is the centroid of the state. The order of the polynomial function and its coefficients are indicated by $n \leq 2$ and a_i, respectively. In the second region, above 7 MeV where the high level density did not allow an appropriate peak fitting, the number of events was calculated by integrating the spectrum in specific energy bins. The energy bin width and position were selected to follow structures in the spectrum. In Fig. 4.15 an example of the spectrum decomposition is illustrated. The boundaries

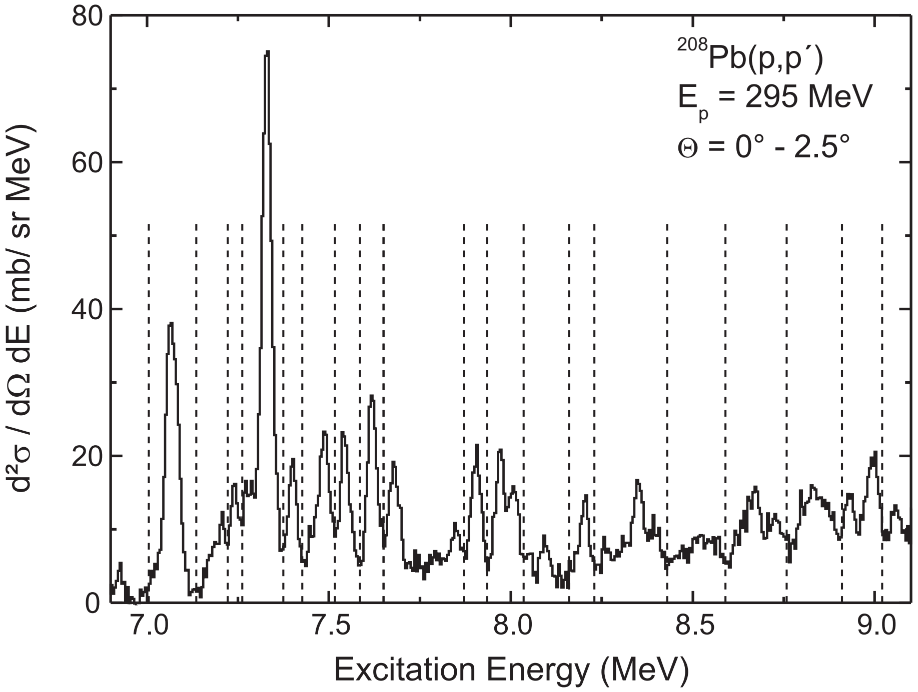

Fig. 4.15: Excitation energy spectrum of the ^{208}Pb reaction above 7 MeV divided in specific energy bins, which follow spectrum structure. Dashed lines correspond to the edges of each specific excitation energy bin.

of each energy bin are shown with dashed lines. For $E_x > 9$ MeV, in the GDR region, 200 keV bins were analyzed.

4.10 Polarization analysis

Using the information on the beam polarization and the polarization of the scattered protons at the focal plane, one is able to compute the polarization transfer observables at 0°.

$$\begin{aligned} p_S^{\prime\prime t} &= D_{SS} p_S \cos\chi_p + D_{LL} p_L \sin\chi_p, \\ p_S^{\prime\prime b} &= p_S \cos\chi_p + p_L \sin\chi_p. \end{aligned} \tag{4.20}$$

Here, $p_S^{\prime\prime t(b)}$ denotes the sideways polarization of scattered protons at the detector position for true(background) events, respectively. The sideways(logitudinal) components of the beam polarization (see Sec. 4.4) is presented with $p_{S(L)}$, respectively , and χ_p is the spin precession angle in the spectrometer given by

$$\chi_p = \gamma \cdot (\frac{g}{2} - 1) \cdot \chi_b. \tag{4.21}$$

Here, the χ_b is the bending angle of the spectrometer (162° and 180° for the measurements in October 2006 and November 2008, respectively), γ is the proton Lorentz factor, g is a Lande-factor. The polarization of the doubly scattered protons was calculated using the estimator method [161]. It is based on an unbiased effective estimator

$$\hat{\varepsilon} = \begin{pmatrix} \hat{\varepsilon}_N \\ \hat{\varepsilon}_S \end{pmatrix}, \tag{4.22}$$

which can be displayed in matrix form as

$$\hat{\varepsilon} \equiv \mathbf{F}^{-1}\mathbf{B}, \text{ with} \tag{4.23}$$

$$\mathbf{F} \equiv \begin{pmatrix} \sum_N \cos^2\phi_{fpp} & \sum_N \cos\phi_{fpp}\sin\phi_{fpp} \\ \sum_N \cos\phi_{fpp}\sin\phi_{fpp} & \sum_N \sin^2\phi_{fpp} \end{pmatrix}, \quad \mathbf{B} \equiv \begin{pmatrix} \sum\limits_N \cos\phi_{fpp} \\ \sum\limits_N \sin\phi_{fpp}, \end{pmatrix}. \tag{4.24}$$

The summation $\sum_N$ runs over all events. Taking into account the symmetry of the system at the beam orientation flipping, one gets

$$\begin{aligned} \hat{\varepsilon}_N &\cong \varepsilon_N = p''_N\langle A_y\rangle, \\ \hat{\varepsilon}_S &\cong \varepsilon_S = -p''_S\langle A_y\rangle, \end{aligned} \tag{4.25}$$

where $\langle A_y\rangle$ is the effective analyzing power of the FPP. The sideways estimators for true and background events are given by

$$\begin{aligned} \varepsilon_S^t &= -p_S''^t\langle A_y\rangle, \\ \varepsilon_S^b &= -p_S''^b\langle A_y\rangle, \\ \varepsilon_S^{t+b} &= \frac{N_t\varepsilon_S^t + N_b\varepsilon_S^b}{N_t + N_b}. \end{aligned} \tag{4.26}$$

Assuming that background events do not contribute to the depolarization, i.e. polarization observables for the background are equal to unity $D_{SS}^b = D_{LL}^b = D_{NN}^b = 1$ and using data with two different beam polarizations, the $\langle A_y\rangle$ value can be calibrated [154]. The region of N_{t+b} events is selected in the corrected y or y_c histogram (see Fig. 4.10 and Fig. 4.11). In the analysis, the signal to noise (N_t/N_b) ratio can be determined with good statistical accuracy. Then the figure of merit (FOM) can be defined by the number of signals N_t and noise N_b events

$$FOM = \sqrt{N_t}\frac{N_t}{N_t + N_b}. \tag{4.27}$$

According to a simple calculation the FOM has a maximum at 1.2 - 2.0σ for ratios N_t/N_b=0.2 - 10 in the y_c histogram. In the present analysis, a value of $\pm 1.3\sigma$ was chosen, which corresponds to ± 3 mm on the y_c axis, defining the gate for the event collection during the polarization data analysis. The estimators ε_S^b and ε_S^{t+b} are measured by the asymmetry in the FPP. Using Eqs. (4.26) and (4.20) one gets

$$\frac{N_t + N_b}{N_t}\frac{\varepsilon_S^{t+b}}{\varepsilon_S^b} - \frac{N_b}{N_t} = \frac{D_{SS} + \frac{p_L}{p_S}\tan\chi_p D_{LL}}{1 + \frac{p_L}{p_S}\tan\chi_p} \equiv \frac{D_{SS} + c_S D_{LL}}{1 + c_S} \equiv D_{SS}^{mix} \tag{4.28}$$

$$= \frac{D_{LL} + \frac{p_S}{p_L}\tan^{-1}\chi_p D_{SS}}{1 + \frac{p_S}{p_L}\tan^{-1}\chi_p} \equiv \frac{D_{LL} + c_L D_{SS}}{1 + c_L} \equiv D_{LL}^{mix}. \tag{4.29}$$

These equations are used for the data from October, 2006 and November, 2008, respectively. Combining them one is able to determine the matrix of the polarization transfer coefficients D_{SS} and D_{LL}

$$\begin{aligned} &\begin{pmatrix} (1+c_S)D_{SS}^{mix} \\ (1+c_L)D_{LL}^{mix} \end{pmatrix} = \begin{pmatrix} 1 & c_S \\ c_L & 1 \end{pmatrix} \begin{pmatrix} D_{SS} \\ D_{LL} \end{pmatrix} \Rightarrow \\ &\begin{pmatrix} D_{SS} \\ D_{LL} \end{pmatrix} = \frac{1}{1-c_S c_L} \begin{pmatrix} 1 & -c_S \\ -c_L & 1 \end{pmatrix} \begin{pmatrix} (1+c_S)D_{SS}^{mix} \\ (1+c_L)D_{LL}^{mix} \end{pmatrix} . \end{aligned} \tag{4.30}$$

The coefficients c_S and c_L are of the order of 0.02 for the ^{208}Pb data, thus the difference between mixed and pure polarization transfer observables is small.

5 Results and discussions

5.1 Coulomb excitation of the E1 transitions

A spectrum of the ^{208}Pb(p,p′) reaction with the spectrometer set at 0° is shown in Fig. 5.1. The arrows indicate transitions which are also identified in a (γ,γ') experiment [29]. Essentially all prominent dipole transitions observed in the latter experiment are also excited in the present measurements. An estimate for these transitions based on the semiclassical theory of Coulomb excitation, described in Sec. 2.2, was performed. It demonstrates that the observed cross sections at 0° are indeed due to virtual photon interaction. As examples, the results for the prominent transitions to 1^- states at E_x = 5.512 MeV and 6.720 MeV are shown in Fig. 5.2. The corresponding angular distributions of the differential cross sections are presented. The dashed lines are predictions of Coulomb excitation cross sections using the semiclassical approach [99], which reproduce the data very well. Because of the finite angular resolution of the Grand Raiden spectrometer, the calculated angular distributions were convoluted with Gaussian functions. Their widths correspond to the vertical and horizontal angular resolutions of the detector system. The deviation between calculated and experimentally obtained cross sections at scattering angles larger than 2° is mostly due to the Coulomb-nuclear interference and contributions from unresolved transitions with higher multipolarities. In order to determine these contributions, a multipole decomposition analysis was performed, as described in Sec. 5.2.

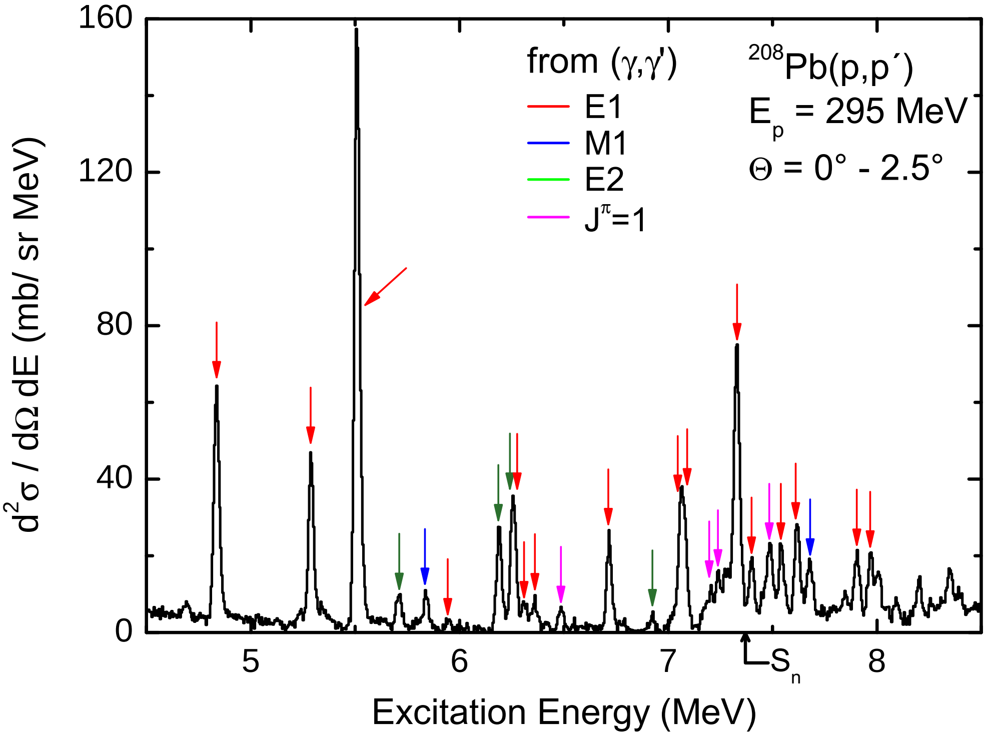

Fig. 5.1: Low-energy part of the spectrum of the ^{208}Pb(p,p') reaction at E_p = 295 MeV and Θ_{lab} = 0°. The arrows indicate transitions which are also observed in the ^{208}Pb(γ,γ') experiment [29].

5.2 Decomposition of measured cross sections

In order to assign the spin and parity of excitated states in the spectrum, two independent methods were used in the present analysis. The first one is a multipole decomposition analysis

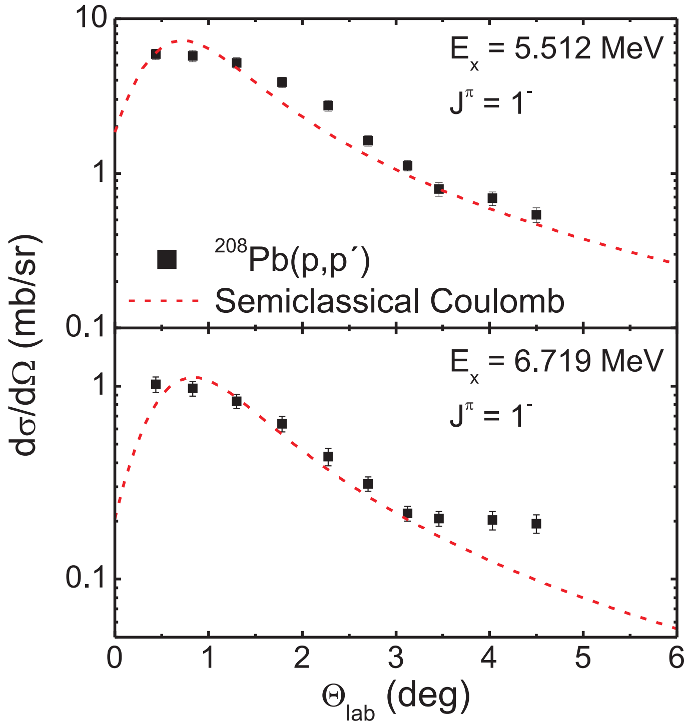

Fig. 5.2: Angular distributions of the excitation of prominent 1^- states at E_x = 5.512 MeV and 6.720 MeV in ^{208}Pb. The dashed lines are predictions of Coulomb excitation cross sections based on the semiclassical approach [99].

(MDA) which is based on predictions of the shape of the cross sections angular distributions. This technique is commonly used in the analysis e.g. of the charge-exchange reactions for B(GT) strength determination [162, 163] or in the investigation of the isoscalar giant resonances with inelastic α-particle scattering [164, 165]. The second method is based on the analysis of the polarization transfer coefficients. It allows a model-independent [106] distinction between spinflip and non-spinflip transitions. Such kind of decomposition was successfully applied for the investigation of the spinflip transitions in ^{12}C [150].

5.2.1 Multipole decomposition analysis

The theoretical proton scattering cross sections were calculated using the code DWBA07 [95] with the RPA amplitudes and single-particle wave functions calculated within the QPM model [29]. The t-matrix parametrization of Franey and Love [91] at 325 MeV was used as effective projectile-target interaction. For each discrete transition below 7 MeV and each excitation energy bin above 7 MeV, the experimentally obtained angular distributions $\frac{d\sigma}{d\Omega}(\theta_{lab}, E_x)\big|_{data}$ were fitted by means of the least-square method with a superposition of the calculated angular distributions $\frac{d\sigma}{d\Omega}(\theta_{lab}, E_x, J^\pi)\big|_{DWBA}$ weighted with fitting coefficients a^{J^π} as

$$\frac{d\sigma}{d\Omega}(\theta_{lab}, E_x)\big|_{data} = \sum_{J^\pi} a^{J^\pi} \frac{d\sigma}{d\Omega}(\theta_{lab}, E_x, J^\pi)\big|_{DWBA} . \tag{5.1}$$

For the MDA of the proton scattering data the following assumptions were made:

- angular distributions were restricted to $\Theta_{lab} \leq 4°$. Although data were measured up to $\Theta_{lab} = 10°$, the complexity of the nuclear interaction and strongly increasing level density at higher momentum transfers prevent the use of such data.

- The following theoretical curves were related:
  - spin M1 excitations represented by a single characteristic curve. This is justified by the similar angular dependence of the cross section in the calculated Θ_{lab} range for all transitions of this type
  - E1 transitions with a model B(E1) strength larger than 0.01 e^2fm^2. The corresponding angular distributions do show sensitivity on the Coulomb-nuclear interaction
  - E2 or E3 angular distributions which substitute all contributions of transitions with $\Delta L > 1$. Representative shapes were taken from collective transitions
- all a^{J^π} coefficients are positive.

Thus, in the analysis the following J^π values are included: 1^+, 1^-, 2^+ (or alternatively 3^-). Other multipolarities of potential relevance like M2 or E4 were neglected because of the similarity of the angular distributions to either E2 or E3, respectively. Examples of the angular distributions normalized to one are presented in Fig. 5.3. The red, blue, green, cyan, brown and orange lines correspond to the prominent excitations of 1^-, 1^+, 2^+, 2^-, 3^-, and 4^+ states, respectively.

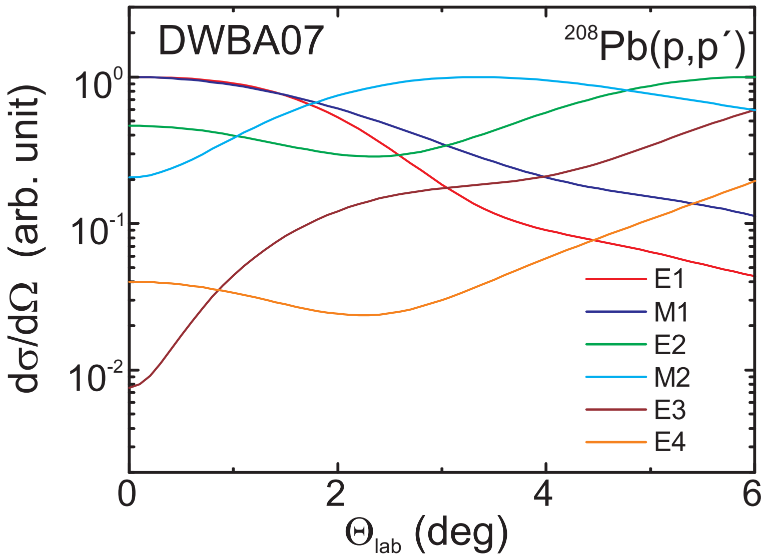

Fig. 5.3: DWBA calculations of ^{208}Pb(p,p) cross sections for the excitation of 1^+, 1^-, 2^+, 3^-, 2^- or 4^+ states at E_p = 295 MeV using the code DWBA07 [95].

In the fitting procedure all possible combinations of transitions from the considered multipolarities are included. After the whole set of the fitting parameters has been computed, weighted mean values of the partial cross sections are obtained using the χ^2 values as a weighting parameter

$$\langle\frac{d\sigma}{d\Omega}\rangle_{weighted} = \frac{\sum_i \omega_i \frac{d\sigma}{d\Omega i}}{\sum_i \omega_i}. \tag{5.2}$$

The weighted variance for the set of data can be determined as

$$\sigma^2_{weighted} = \frac{\sum_i \omega_i \left(\frac{d\sigma}{d\Omega i} - \langle\frac{d\sigma}{d\Omega}\rangle_{weighted}\right)^2}{\sum_i \omega_i}, \tag{5.3}$$

with weights given by $\omega_i = 1/\chi_i^2$.

In the excitation energy region below 7.1 MeV, where all 1^- transitions are known, the fitting procedure was simplified by including only those configurations that correspond to the low-lying E1 transitions from QPM and E2 (alternatively E3) angular distributions. For the only 1^+ state below 7 MeV, known to have isoscalar character, the M1 angular distribution with the corresponding shape and E2/E3 ones were used. In Fig. 5.4 examples of the least-square fit with the best χ^2 values are shown for two selected 1^- states at E_x=5.512 MeV and 6.720 MeV and for the 1^+ state at E_x=5.844 MeV. The combination of included states in these examples is based on the experimental information about close-lying states [158, 166]. For instance, it is known that a strongly excited 3^- state at 5.516 MeV exists. This explains the E3 contribution to the angular distribution of the 5.512 MeV state as seen from Fig. 5.4 (left plot). Also more than two 3^- states and possible 2^+ transition are located around 1^+ state at E_x=5.84 MeV [158, 166]. Thus, they may contribute to the angular dependence of the cross section. As shown in Fig. 5.4 (right plot), this agrees with the results of the fit.

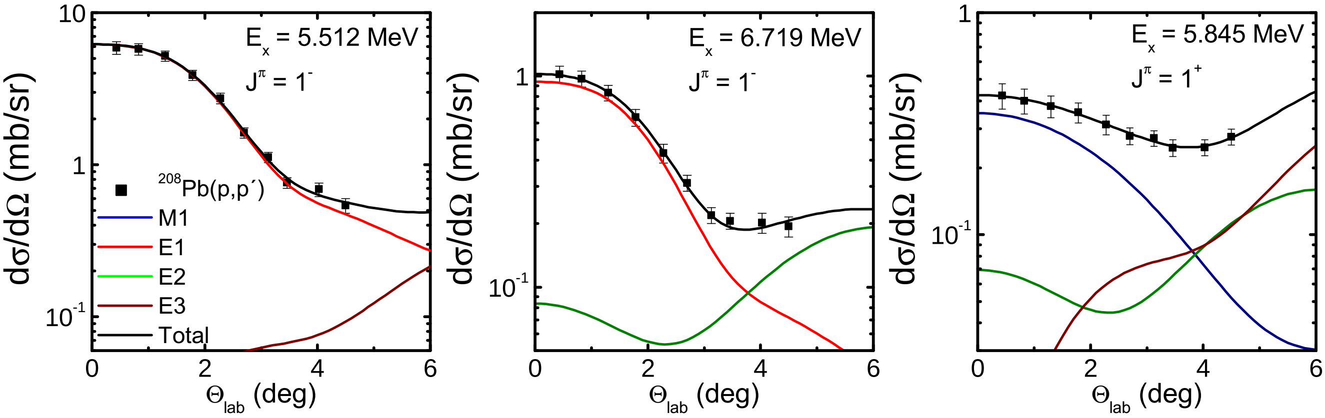

Fig. 5.4: Decomposition of cross sections for two low-lying 1^- states at E_x = 5.51 MeV and 6.72 MeV and for the 1^+ state at E_x = 5.84 MeV.

In the excitation energy region from 7 MeV to 9 MeV more than 500 possible combinations of different configurations were concidered. In Fig. 5.5 examples with best χ^2 values for two selected excitation energy bins around the particle separation threshold centered at E_x=7.31 MeV and E_x=7.39 MeV are presented. The results clearly show the sensitivity of the method for a dis-

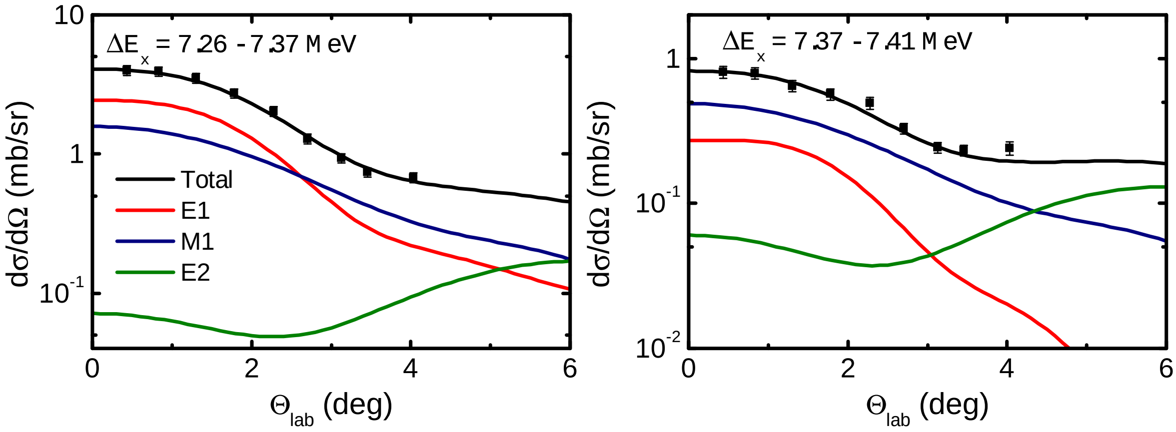

Fig. 5.5: Decomposition of cross sections for two excitation energy bins around neutron emission threshold at E_x=7.3 MeV (l.h.s.) and 7.4 MeV (r.h.s.).

tribution of E1 and M1 transitions with comparable cross sections in one case (l.h.s. in Fig. 5.5) and dominance of the M1 in the second one (r.h.s. in Fig. 5.5). As theoretical curves calculated with the PDR wave functions led to poor χ^2 values in the excitation energy region from 8.2 MeV to 9 MeV, E1 angular distributions were replaced by those calculated for the GDR region.

The multipole decomposition of the spectrum in the giant dipole resonance region was performed similar to those described above. But some important changes were applied, because all possible combinations of theoretical curves led to a vanishing spin M1 contribution. The same results were received for E3 angular distributions. Thus, in order to describe the behavior of the differential cross section at higher excitation energies and include all unknown contributions from other multipolarities and quasi-free scattering, a so-called phenomenological background was introduced. For this purpose, the spectrum in the energy region from 20.5 MeV to 22.5 MeV was divided into four bins, each 500 keV wide, and the angular distributions of the differential cross sections in the scattering angle range from 0° to 10° were extracted. They were fitted with a polynomial of the third order, as shown in Fig. 5.6. The resulting function is identical for all four energy bins and given by

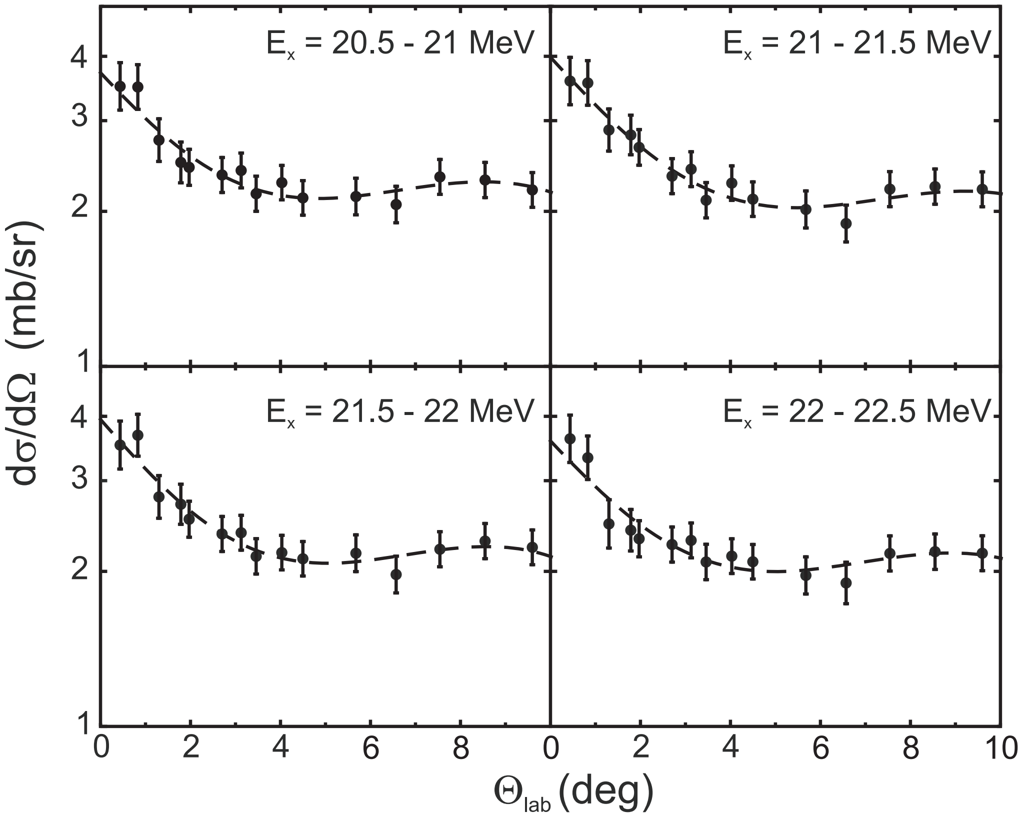

Fig. 5.6: Angular distributions of the cross sections at excitation energies from 20.5 MeV to 22.5 MeV in 500 keV bins fitted by a polynomial function of third order Eq. (5.4).

$$\frac{d\sigma}{d\Omega}(\theta_{lab})\Big|_{bg} = 3.72 - 0.81 \cdot \theta_{lab} + 0.13 \cdot \theta_{lab}^2 - 0.007 \cdot \theta_{lab}^3. \tag{5.4}$$

The dashed curves illustrate the results of the fit. Summarizing, for the cross section decomposition in the GDR region the following DWBA angular distributions were used: E1 and E2 as in previous case and the polynomial described by Eq. (5.4). Results of the analysis are depicted in Fig. 5.7, which shows the full spectrum for a small angular cut from 0° to 0.94°. The solid curve

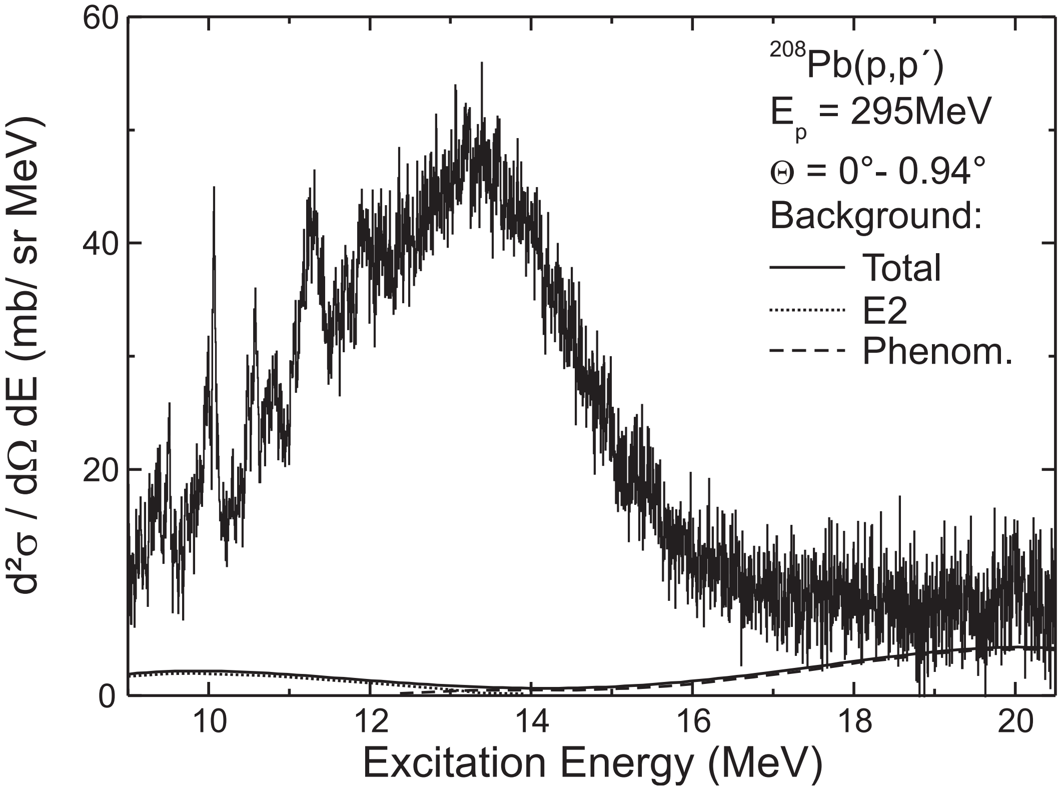

Fig. 5.7: Decomposition of the spectrum in the GDR region on E1, E2 cross sections and a phenomenological background. The histogram shows the excitation energy spectrum from 9 MeV to 21 MeV in a small scattering angle cut Θ_{lab} = 0° - 0.94°. The dotted curve corresponds to the E2 contribution, while the dashed one shows the phenomenological background, and the solid curve illustrates the sum of these contributions.

represents the total background containing the contributions from E2 transition, shown with the dotted black curve and the empirically obtained background, illustrated by the dashed line. The fraction of the cross section under the dotted line corresponds to the excitation of the 2^+ states. It is in a good agreement with a calculation assuming exhaustion of the EWSR for giant quadrupole resonances (GQR) [1]. In Tab. 5.1 results of the multipole decomposition analysis for the excitation energy range from 4.8 MeV up to 9 MeV are presented. The E1 and M1 cross sections, listed in the table, are integrated over a scattering angle range from 0° to 0.94°.

5.2.2 Decomposition based on total spin transfer

With the D_{SS} and D_{LL} polarization observables, extracted by a polarization analysis as described in Sec. 4.10, one is able to decompose the total doubly differential cross section into spinflip and non-spinflip parts using the total spin transfer Σ introduced in Eq. (2.47) and applying Eqs. (2.48, 2.49). In the top panel of the Fig. 5.8 the extracted cross section is plotted. The second and third rows display the D_{SS} and D_{LL} polarization transfer coefficients, respectively, while the bottom panel shows the total spin transfer deduced. The main contributions to the uncertainties in the determination of the spin observables stem from the limited statistics in a secondary scattering experiment. Clearly, there is a concentration of a spinflip cross sections between 7 and 9 MeV, which arises from the spinflip M1 resonance. In the GDR region Σ is equal to 0, as expected, underlining the non-spinflip character of the electric dipole transitions. In the excitation energy region $E_x \geq 16$ MeV, the total spin transfer shows deviations from zero,

Tab. 5.1: Dipole transitions observed in ^{208}Pb(p,p') reaction at 0° below 9 MeV.

E_x, MeV	ΔL	σ_{E1}, mb	σ_{M1}, mb	B(E1), $\mathrm{e^2fm^2}$
4.8420(22)	1	2.21(33)		0.118(17)
5.2949(22)	1	1.63(12)		0.112(8)
5.5128(11)	1	5.71(30)		0.397(21)
5.8417(50)	0		0.35(2)	
5.9463(59)	1	0.16(1)		0.013(1)
6.2642(26)	1	0.62(8)		0.057(17)
6.3131(59)	1	0.32(2)		0.032(2)
6.3585(65)	1	0.21(3)		0.020(3)
6.4835(49)	1	0.15(2)		0.015(2)
6.7184(26)	1	0.88(6)		0.095(6)
7.005 - 7.135	0, 1	2.06(3)	0.22(1)	0.206(14)
7.135 - 7.225	0, 1	0.48(10)	0.28(8)	0.015(2)
7.225 - 7.265	0, 1	0.41(9)	0.25(7)	0.028(4)
7.265 - 7.375	0, 1	2.47(39)	1.52(30)	0.254(23)
7.375 - 7.425	0, 1	0.24(4)	0.57(6)	0.021(3)
7.425 - 7.515	0, 1	0.71(13)	0.95(15)	0.053(12)
7.515 - 7.585	0, 1	0.72(15)	0.63(14)	0.061(13)
7.590 - 7.650	0, 1	0.83(21)	0.39(15)	0.109(25)
7.655 - 7.725	0, 1	0.87(5)	0.14(2)	0.104(6)
7.730 - 7.860	0, 1	0.68(11)	0.30(8)	0.072(18)
7.865 - 7.935	0, 1	0.95(2)	0.09(1)	0.120(18)
7.935 - 8.035	0, 1	1.23(15)	0.26(7)	0.167(18)
8.040 - 8.160	0, 1	0.51(10)	0.27(7)	0.055(13)
8.160 - 8.230	0, 1	0.36(8)	0.25(7)	0.052(12)
8.230 - 8.430	0, 1	1.65(5)	0.20(2)	0.242(15)
8.430 - 8.590	0, 1	1.05(9)	0.27(4)	0.145(20)
8.595 - 8.745	0, 1	1.24(12)	0.34(6)	0.191(25)
8.750 - 8.910	0, 1	1.60(6)	0.19(2)	0.277(23)
8.910 - 9.000	0, 1	1.24(2)	0.06(0)	0.215(24)

which might result from the spinflip part of quasielastic scattering processes [167] or spin-dipole excitations.

5.2.3 Comparison of both methods

In Fig. 5.9 a comparison of the cross sections obtained by the two methods described above, is shown in panels (a) and (b) for the low excitation energy part of the spectrum and the GDR region, respectively. The figures show from top to bottom the total cross sections and their

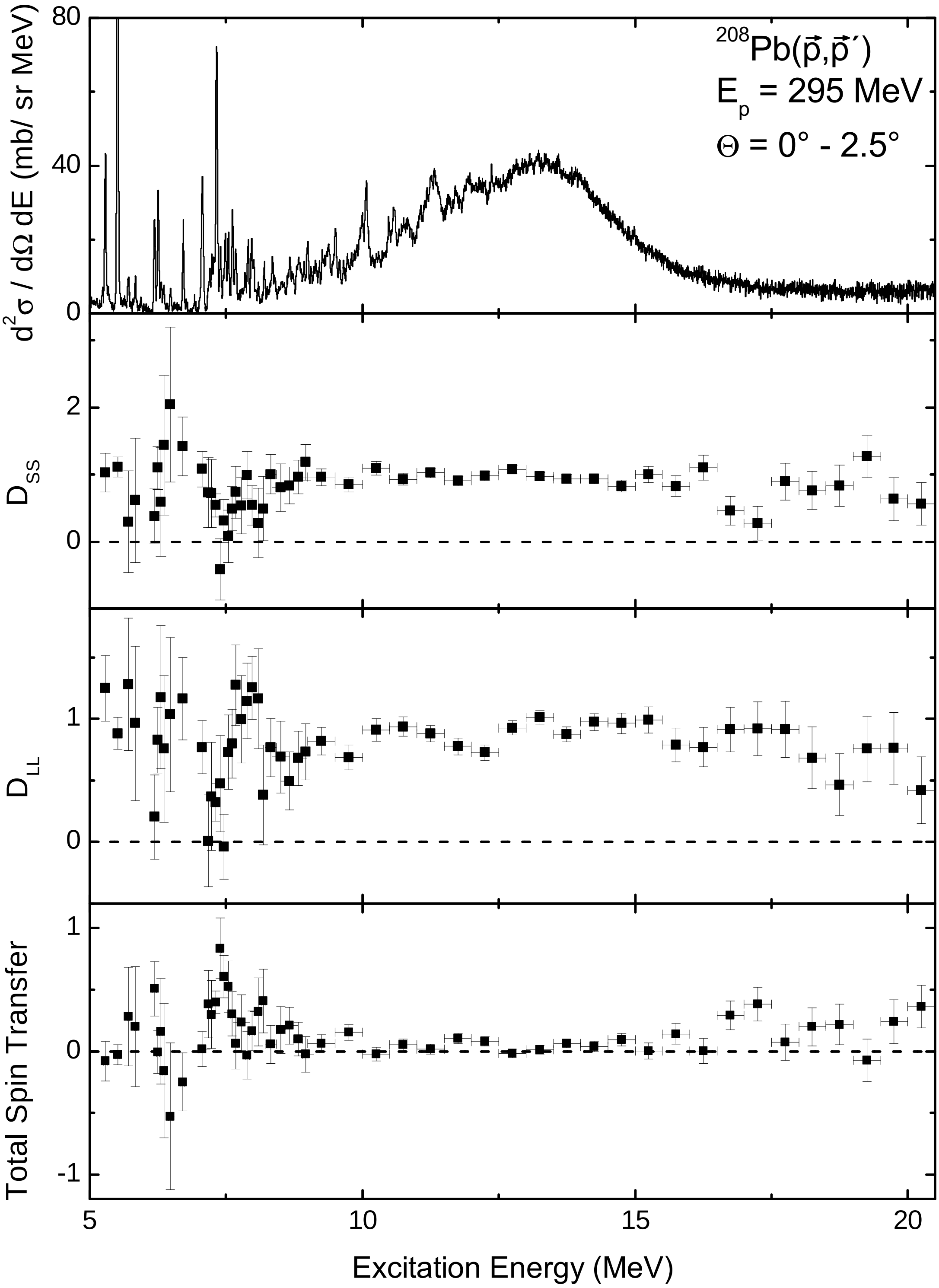

Fig. 5.8: Polarization transfer coefficients D_{SS} and D_{LL} and the total spin transfer Σ from the ^{208}Pb($\vec{p}, \vec{p}'$) scattering at 0° spectrometer setting. Note the difference in the scales on the plots.

decomposition into spinflip (ΔS =1) and non-spinflip (ΔS =0) parts. The diagonally hatched (⁄⁄⁄) area shown in red represents the results of the multipole decomposition analysis. The diagonally hatched (\\\) area in blue corresponds to the cross section decomposition, obtained from the polarization transfer observables. Thus, the doubly hatched area indicates the region

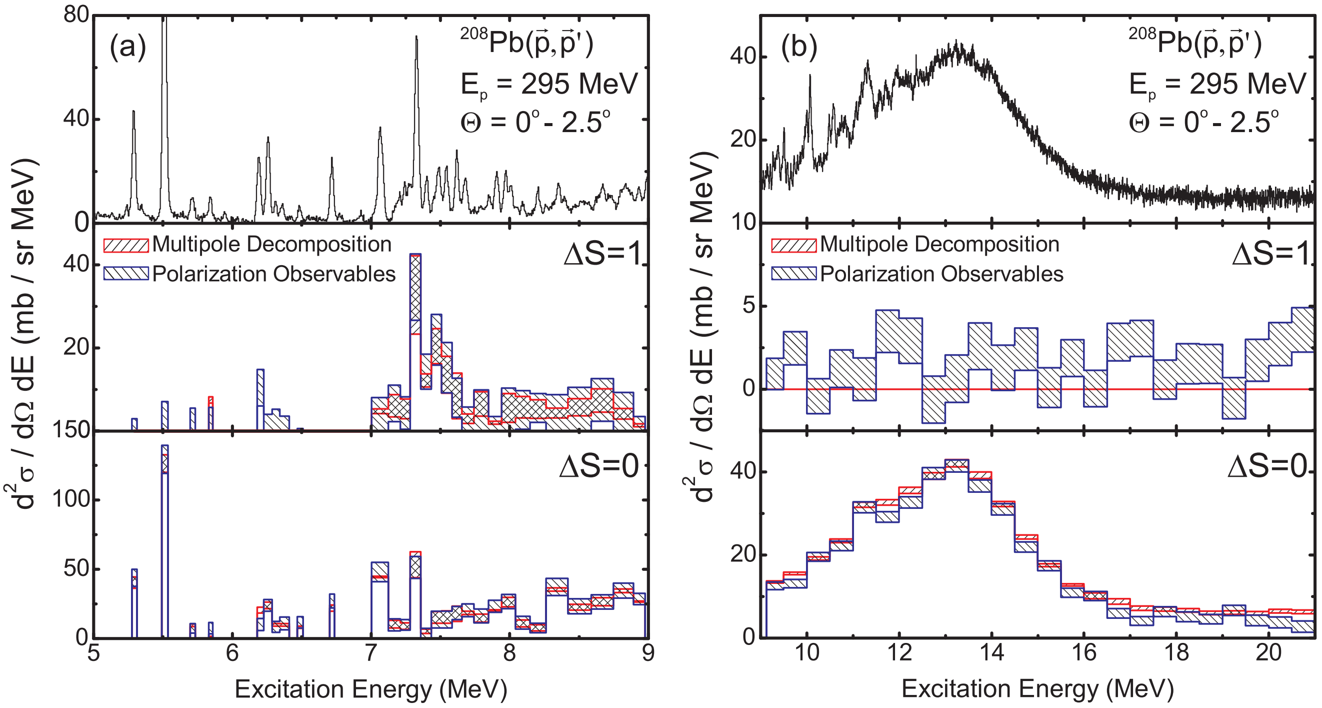

Fig. 5.9: Decomposition of non-spinflip (ΔS = 0) and spinflip (ΔS = 1) cross section parts based on the MDA and polarization transfer, respectively, in the excitation energy region between 5 and 9 MeV (a) and in the GDR region (b).

where both methods give the same results within error bars. Clearly, these two independent methods based on very different properties of the proton-nucleus interaction agree extremely well, in particular for excitation energies up to 9 MeV. In the GDR region, the MDA method does not allow a reliable extraction of possible small $\Delta S = 1$ cross section parts.

5.3 Extraction of the complete electric dipole strength

5.3.1 B(E1) strength at excitation energies below 9 MeV

The complete electric dipole strength distribution was extracted using the virtual photon method and the direct proportionality between the reduced transition probability B(E1) and the Coulomb excitation cross section. Electric dipole strengths were calculated converting the E1 cross section part using Eqs. (2.28) and (2.29) for the double differential cross section and the virtual photon flux. The B(E1) transition strengths, deduced from the present experiment (see Fig. 5.10) show an excellent correspondence with the NRF results of Refs. [28,29,30,31] below the neutron separation energy (S_n = 7.367 MeV). In the top part of Fig. 5.10 the weighted mean values from four (γ,γ') experiments, listed in Tab. A.1, and the data from the ^{207}Pb(n,γ) reaction [158] are plotted, while in the bottom part B(E1) values from the present ^{208}Pb(p,p′) measurements are presented. In Tab. 5.1, the B(E1) values extracted from the present work, using semiclassical Coulomb excitation [99] for transitions up to 9 MeV are listed. The low-energy strength seen in (γ,γ') experiments has been attributed to the PDR. The MDA analysis of the present work indicates a structural change of E1 transitions below and above 8.2 MeV, where the former is described by theoretical angular distributions calculated for the PDR and the latter for the GDR. Thus, one may extract global PDR properties by summing between 6.2 and 8.2 MeV. Transitions at lower energies have been shown to be of single-particle nature [29].

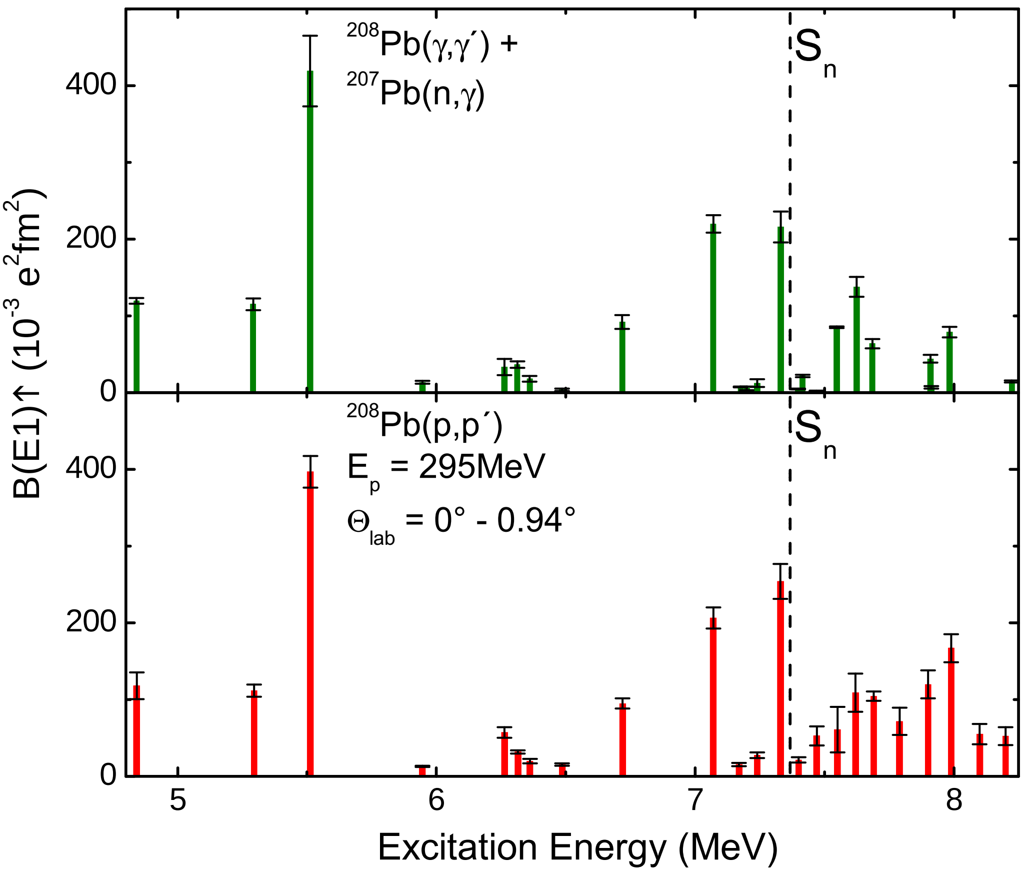

Fig. 5.10: B(E1) strength distribution in ^{208}Pb below the GDR extracted from the present work (bottom) in comparison to the (γ,γ') results from [28, 29, 30, 31] and ^{207}Pb(n,γ) data from [158] (top).

The comparison of the summed B(E1) strength in the PDR region and its centroid deduced in the present work with data from NRF experiments are summarized in Tab. 5.2. Due to the additional strength found in the present experiment, the centroid energy of the PDR is shifted to the higher energy relative to the photon scattering experiments.

Tab. 5.2: PDR properties in ^{208}Pb compared to the model predictions.

	Present work	(γ,γ')	QPM	RQTBA
E_c, MeV	7.43(2)	7.3(3)	6.51	6.80
$\sum_{6.2MeV}^{8.2MeV}$ B(E1), e^2fm^2	1.54(16)	1.10(11)	1.29	3.93

Combining the data above the neutron separation energy from the present work with those from photon scattering [29, 31] one is able in principle to extract the neutron decay width. The total transition width above the threshold is given by

$$\Gamma = \Gamma_\gamma + \Gamma_n. \tag{5.5}$$

Here, Γ_γ is the partial γ-width and Γ_n denotes the neutron decay width. The difference between strengths deduced from the present and the NRF experiments results from the fact, that Γ_n becomes dominating very fast in the total transition width Γ. As an example, the neutron width for the transition at E_x = 7.55 MeV was extracted and is equal to Γ_n = 89.8±18.7 eV, in good agreement with the value of 92 eV (with unknown experimental uncertainties) from [158]. However, the extraction of neutron widths is based on the assumption that only a single transition is excited in the analyzed energy bin. Thus, in order to perform further accurate analysis a reduction of the width of energy bins in the present analysis is required.

5.3.2 The total absorption cross section in the giant dipole resonance region.

In the giant dipole resonance region total photoabsorption cross sections are given rather than the B(E1) values in order to facilitate direct comparison with other experiments. In order to minimize statistics contribution to the error bars, the spectrum was analyzed in 200 keV steps. The total gamma absorption cross section for the GDR deduced in the present analysis is shown in Fig. 5.11 as full red circles. Our data are compared to a measurement of the ^{208}Pb(γ,xn) reaction [168, 169] plotted as solid black line and to the total nuclear absorption cross section data measured with a tagger system [170]. All three sets of data are in a very good agreement. The complete table with data used, can be found in Tab. A.2.

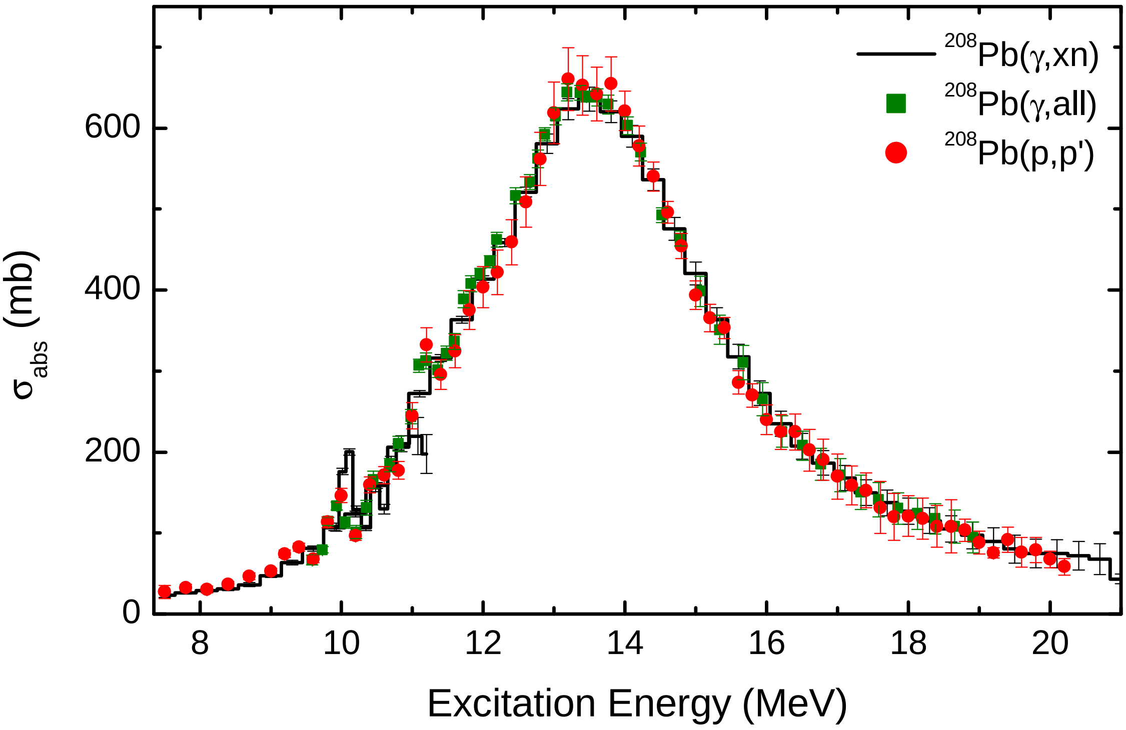

Fig. 5.11: Total absorption cross sections for the GDR region. Red circles denote σ_{abs} obtained in the present work, green squares are the results from [170] and black histogram represents the (γ,xn) data from [168, 169].

5.3.3 E1 response in ^{208}Pb: experiment vs. theory

The present data provide a unique test of models aiming at a microscopic description of the PDR. Examples are the QPM and RQTBA approaches described in Sec. 2.4. Models cannot be judged solely by comparing the predictions in the low-energy region but they should be able to reproduce the E1 response over the full excitation spectrum. The strength distributions calculated with QPM and RQTBA are plotted in Fig. 5.12. In the top panel, $B(E1)$ strengths in the PDR

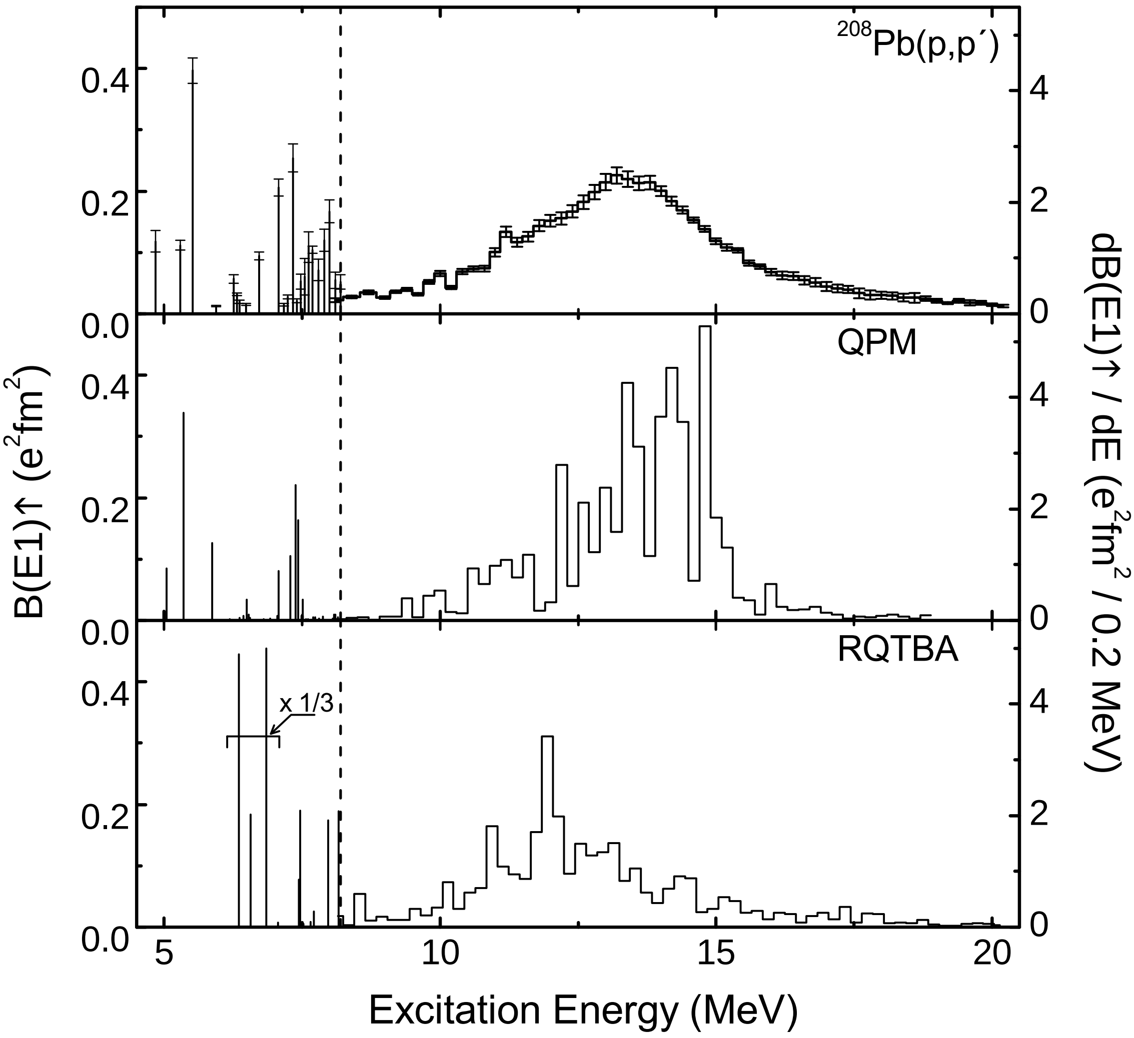

Fig. 5.12: E1 response in ^{208}Pb between 5 MeV and 20 MeV from the present experiment in comparison with theoretical calculations within the QPM and RQTBA models. From top to bottom: experiment, QPM, RQTBA. Note the difference in the scales for the low-lying part (below 8.2 MeV) and the GDR region (above 8.2 MeV).

region (left scale) and $dB(E1)$ per 200 keV (scale on the right) in the GDR are shown. The middle plot represents the QPM model predictions, and the bottom one corresponds to the RQTBA calculations. QPM configurations up to $3p-3h$ in the PDR region and up to $2p-2h$ ones in the GDR one were included. The relativistic time blocking approximation includes $1p-1h$⊗phonon coupling between 2-quasiparticles configurations up to 25 MeV and phonons up to 10 MeV. In the PDR region QPM gives a reasonable fragmentation compared to the experiment, in contrast to the RQTBA result. Thus, the inclusion of the $3p-3h$ configurations is important for realistic description of fine structure in the PDR region. In Tab. 5.2 the properties of the pygmy dipole resonance extracted in the present work are compared to those from the model predictions. The centroid energy and the summed B(E1) strengths are deduced in the energy range from 6.2 MeV to 8.2 MeV. The QPM results slightly underpredict the total strength, while the value from RQTBA is three times larger. The PDR centroid energies predicted from both model are too low. For the comparison the same excitation energy region from 6.2 to 8.2 MeV was used. This is justified because calculations do show a minimum in the B(E1) distribution around 8 - 8.5 MeV comparable to the experiment. The GDR total width is somewhat underpredicted, originating from the model space limitation. The resonance centroid is correctly reproduced by QPM, while the one calculated in RQTBA is too low.

5.3.4 Electric dipole polarizability

As discussed in Sec. 1, knowledge of the neutron radius or neutron skin thickness of ^{208}Pb is of crucial importance to nuclear structure physics and astrophysics. In a recent paper, Reinhard and Nazarewicz [38] explore the correlations between the neutron skin thickness and the electric dipole polarizability (α_D) in models using Skyrme-type forces and suggest that the neutron skin is strongly correlated with it, but rather weakly correlated with the low-energy electric dipole strength, attributed to the pygmy dipole resonance. Subsequent investigations made by Piekarewicz [39] confirm the strong correlation between α_D and neutron skin for relativistic mean-field models, but in contrast he claims the same for the PDR strength. In any case, it is suggested that α_D is a key quantity to be determined with precision. This is achieved in the present experiment. The conversion of the complete B(E1) strength to the dipole polarizability can be performed using [171]

$$\alpha_{\mathrm{D}} \equiv \frac{\sigma_{-2}}{2\pi^2} \cdot \frac{\hbar c}{e^2} = \sum \frac{\sigma_{\mathrm{abs}}(E_x)}{E_x^2} \cdot \frac{\hbar c}{2\pi^2 e^2}. \tag{5.6}$$

From Eq. (5.6) follows that the high-energy strength component beyond the region explored in the present work gives a rather small contribution, but the fraction coming from the low-lying states may play a role for the determination of α_D. In order to constrain the models and determine the neutron skin, the experimental uncertainties of α_D should be well below 10% [38]. The value known before, determined from the $(\gamma$,xn) reaction data in [168] is (19.2±2) fm^3/e^2, with insufficient precision. In the present experiment, it is possible to extract the polarizability of the nucleus in the energy range up to 20 MeV. In order to perform a proper comparison with available theoretical calculations shown above, which are limited to 19 MeV, the same boundary was placed for the experimental data. The value deduced from the present data is α_D = 18.7±1.3 fm^3/e^2. Inclusion the (γ,γ') data [28, 29, 30, 31] for the low-energy region and photoabsorption experiments [168,169,170] in the GDR region allows to improve the uncertainties even further. In Fig. 5.13 the experimentally obtained dipole polarizability from the present data (top) and the weighted mean value from the above mentioned experiments including proton scattering data (second row) are shown in a comparison with results from the theoretical calculations presented earlier in Sec. 5.3.3. Also, a decomposition into the low-energy and GDR regions is given. As expected, the low energy region contributes with about 7% to the total polarizability. Estimations of the high-energy electric dipole strength to the total dipole polarizability were made using the data of [168]. The excitation energy region from 20 to 35 MeV contributes at most 4%. It allows to assume that inclusion of the even higher-lying part of the E1 strength does not change the value of the dipole polarizability much.

The theoretical predictions for the α_D values are different. The QPM results are too small and the RQTBA predictions are too large, also individually for the low and high-energy parts. The predicted neutron skin radius from QPM is somewhat smaller and RQTBA larger than present experimental estimates based on measurements of the mass transition radius from hadronic scattering [172] and antiproton annihilation [173]. The experimentally obtained dipole polarizability thus suggests a value intermediate between the two theoretical predictions, although it is not clear whether one would find a same correlation between the α_D and the neutron skin as in Refs. [38, 39].

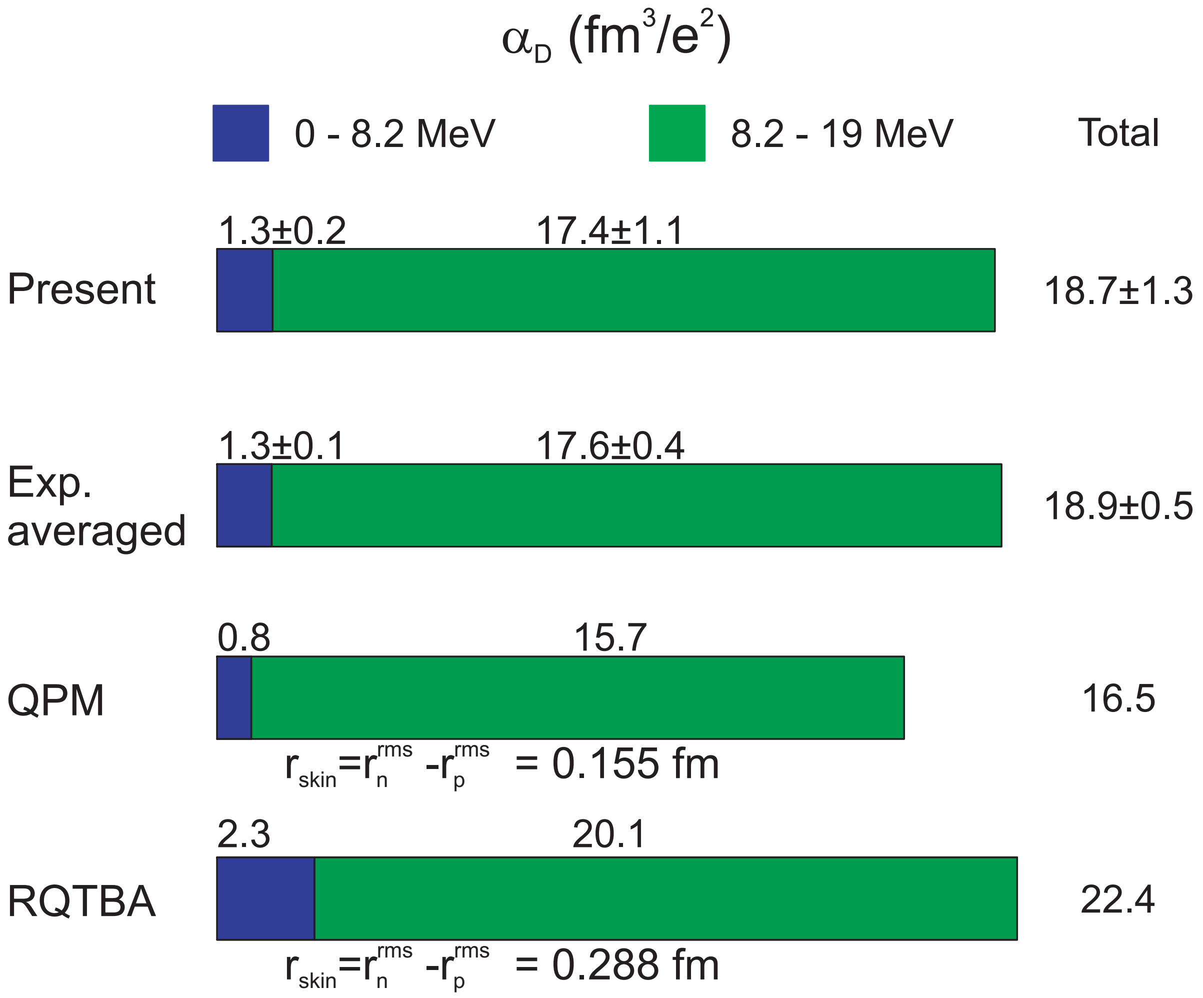

Fig. 5.13: Static dipole polarizability of ^{208}Pb. From top to bottom: α_D extracted in the present thesis; average value for α_D from the available experimental data (see text for details); polarizability and neutron skin radius extracted from the QPM calculations. Bottom: the same for RQTBA predictions. All numerical values for α_D are given in the fm^3/e^2 units. Blue bars correspond to the dipole polarizability in the pygmy dipole resonance region, green ones to the giant resonance region, from 8.2 MeV to 19 MeV.

5.4 Photon strength function

Experimentally, the photon (also often gamma-ray or radiative) strength function (PSF) $f^{X\lambda}$(E,J) [45] in a region of excitation energy E and spin J is connected to average ground state photon width $\overline{\Gamma}_0$ and average photoabsorption cross section $\overline{\sigma}_{abs}$. This relation can be expressed as

$$f^{X\lambda}(E,J)=\frac{\overline{\Gamma}_0(E,\lambda)}{E^{2\lambda+1}}\cdot\rho_(E,J)=\frac{2J_0+1}{(\pi\hbar c)^2(2J+1)}\cdot\frac{\overline{\sigma}_{abs}}{E^{2\lambda-1}}. \qquad (5.7)$$

The average is taken over many levels over a certain energy bin excited by photons with multipolarity λ from the ground state with spin J_0. Radiation with multipolarity $\lambda > 1$ contributes to the absorption only weakly such that $f^{X\lambda=1}$(E) + $f^{X\lambda=2}$(E) + ... $\approx f^{X\lambda=1}$(E). Close to the particle separation energies level density $\rho(E,J)$ is large as compared to the experimental resolution resulting in a smooth energy dependence of the absorption [46, 174]. The photon strength function extracted from the absorption cross sections of the present experiment is shown in Fig. 5.14 (full black squares) in comparison with data measured using the ^{208}Pb($^{3}He,^{3}He'\gamma$) reaction [175]. Here, the calculation of the PSF is based on the extraction of level densities and

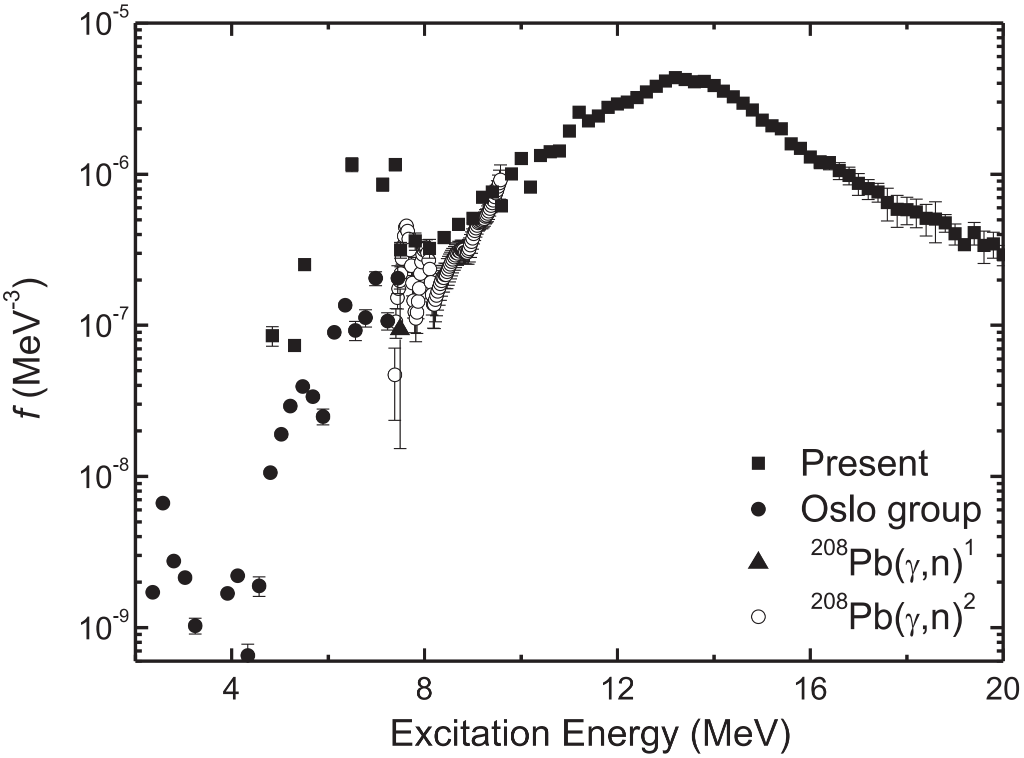

Fig. 5.14: Photon strength function extracted in the present work (full squares) in comparison with the data from [175] (full circles, normalized on ^{208}Pb(γ,n) data from [176] (full triangle) and [177] (empty circles).

corresponding transition widths in the decay to low-lying states [50]. The obtained γ-strength function depends on the normalization procedure chosen. The slope of the strength function is sensitive to the resonance data at the neutron threshold, which have been taken from the literature. The PSF extracted from Ref. [175] was normalized at the neutron separation energy using data of (γ,n) experiments [176] (indicated by full triangle in Fig. 5.14) and [177] (empty circles). The data of [176] provide an information on the M1 contribution to the PSF at the threshold, while data from [177] allow to determine the normalization of the total PSF. In the present results the contribution of M1 transitions to the photon strength function in the threshold region was not taken into account, so they show a lower limit of the PSF only. Clearly, the PSF deduced from the present results in the region around and below the neutron separation energy is about an order of magnitude larger. Such a big discrepancy between these two different methods can occur: one reason may be found in the normalization of the data from ($^{3}He,^{3}He'\gamma$) reaction to the (γ,n) cross sections. Another possible reason is a violation of the Axel-Brink hypothesis [46]. In order to check these two possibilities further analysis of the data in this and other nuclei is needed.

6 Fine structure of the giant electric dipole resonance in ^{208}Pb

The following chapter describes the analysis of the fine structure of the GDR based on wavelet techniques. It is organized as follows: Sec. 6.1 describes the wavelet analysis and its application to the nuclear spectra and the analysis of the characteristic scales in the GDR. The extraction of level densities from the cross section fluctuations with an autocorrelation method is discussed in Sec. 6.2.

6.1 Wavelet analysis

6.1.1 Wavelet transform

The wavelet transform is a new and promising tool to analyze different types of signals. It is used in diverse areas, such as image processing or data compression [178, 179], and also applied in meteorology [180], astrophysics [181] or accelerator physics [182]. The wavelet analysis can be regarded as an extension of the Fourier analysis. In the Fourier analysis one decomposes signals into a sum of harmonic functions of different frequencies, where the time-dependence of the signals is converted into a frequency dependence. A disadvantage of this method is the complete loss of the time information. The wavelet analysis offers the possibility to perform a local analysis conserving the correlation between time and frequency information.

A wavelet is an oscillating form with a finite duration and zero mean value. Thus, wavelet basis functions describe the local behavior more efficient because they are not affected by properties of the data far away from the location of interest. Examples of the widely used wavelet functions are illustrated in Fig. 6.1. The specific choice of the wavelet function depends on the properties of the signal. The coefficients of the wavelet transform, similarly to the Fourier transform, are defined as

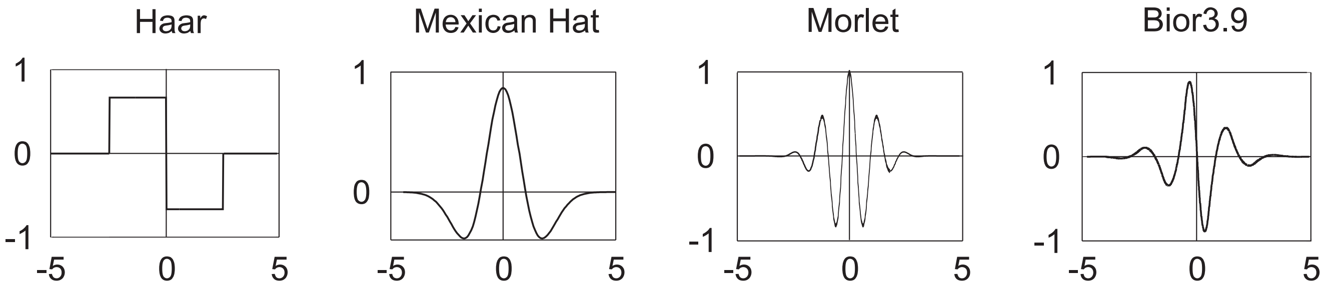

Fig. 6.1: Examples of some frequently used wavelet functions. The Haar wavelet is a combination of step functions, the Mexican hat corresponds to the second derivative of a Gaussian. The Morlet wavelet is a product of Gaussian and cosine functions, while the so-called Bior3.9 function has no analytical form.

$$C\left(\delta E, E_x\right) = \int_{-\infty}^{\infty} \sigma\left(E\right) \Psi\left(\delta E, E_x, E\right) dE\ . \tag{6.1}$$

They depend on two parameters: the scale δE, that stretches and compresses the wavelet Ψ(E), and the position E$_x$, shifting the wavelet in the spectrum σ(E). The variation of the variables can be carried out using continuous (CWT) or discrete (DWT) steps. For the application to nuclear spectra, characteristic scales are extracted using CWT, where the fit procedure can be adjusted to the required precision. It is also possible to reconstruct the original signal out of the wavelet coefficients by using the inverse wavelet transform

$$\sigma(E) = \frac{1}{K_\Psi} \int_{-\infty}^{\infty} \int_{-\infty}^{\infty} C(\delta E, E_x) \frac{1}{\sqrt{\delta E}} \Psi\left(\frac{E - E_x}{\delta E}\right) \frac{d(\delta E)\, dE_x}{\delta E^2}\,, \tag{6.2}$$

where K_Ψ is a normalization factor, depending on Ψ. The reconstruction is exact only if the wavelet functions are orthogonal

$$\int_{-\infty}^{\infty} \Psi_{j,k}(E)\, \Psi^*_{m,n}(E)\, dE = \delta_{jm}\delta_{kn}\,. \tag{6.3}$$

Obviously, a CWT wavelet functions can never fulfill this requirement. One of the possible solutions is to use DWT varying the scales and the positions by powers of two. This leads to an iterative decomposition of the spectrum, by filtering and decomposing it into two signals: approximation (A_i) and details (D_i). The approximation is the large-scale or low-frequency component of the signal, and the detail corresponds to the small-scale or high-frequency part for a given scale region analogue to the effect of the high- and lowpass filters in an electric circuit. This process is schematically shown in Fig. 6.2. In each step of the decomposition, the initial signal σ(E) can be reconstructed as

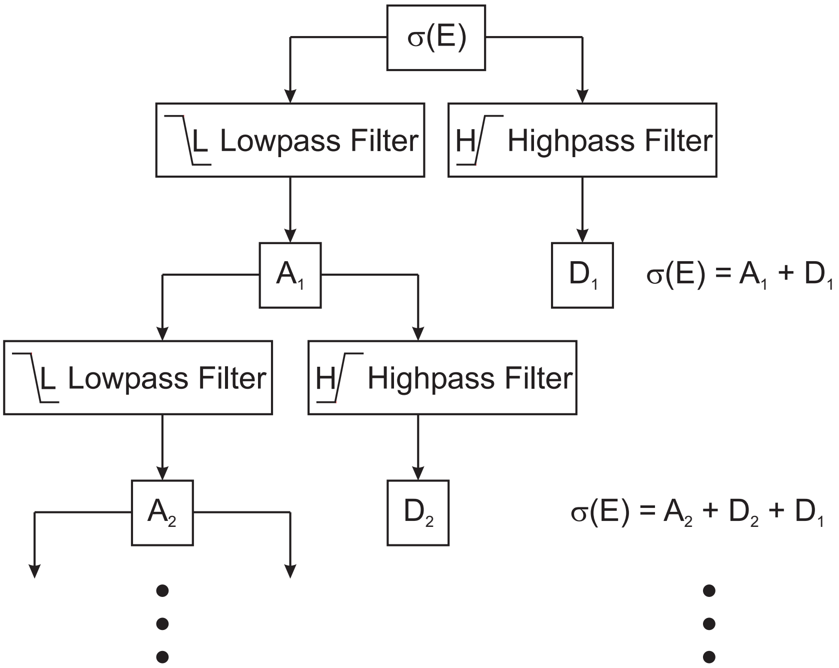

Fig. 6.2: Decomposition of the original signal σ into approximations and details obtained by using the discrete wavelet transform.

$$\sigma(E) = A_i + \sum D_i\,. \tag{6.4}$$

This operation can proceed until the individual detail consists of a single bin. The wavelet function Ψ is determined by the highpass filter which produces the details. There is an additional function associated with some but not all wavelets. This is the so-called scaling function Φ [179].

It is determined by the lowpass filter and is responsible for the approximations. The existence of this function makes the DWT possible.

The choice of the wavelet function plays an important role in the analysis. In order to achieve an optimum representation of the signal using wavelet transformation, one has to select a function Ψ, which resembles the properties and features of the studied signal σ. In fact, the better the correspondence between the shape of Ψ and the signal σ is, the larger is the wavelet coefficient. A maximum of the wavelet coefficients at certain value δE indicates a correlation in the signal at the given scale often called characteristic scale.

The best resolution for the spectra analyzed in the present work can be obtained by using the so-called Morlet wavelet (see Fig. 6.1). Using the fact that the detector response is close to the Gaussian line shape and the Morlet wavelet is a product of Gaussian and cosine functions, one can precisely describe the local features of the spectra. Nevertheless, this function has also a drawback in the absence of the scaling function Φ that makes it impossible to perform the DWT and exactly reconstruct the original signal. As an alternative the Bior3.9 wavelet function can be used. It possesses a scaling function Φ and its form is very similar to one of the Morlet function, as can be seen from Fig. 6.1.

The Bior3.9 wavelet has another useful property which can be applied for a determination of background in the data. Each wavelet function can be characterized by the number of the vanishing moments,

$$\int_{-\infty}^{\infty} E^n \Psi(E)\, dE = 0, \;\; n = 0, 1 ... m. \tag{6.5}$$

For Bior3.9 the number is equal to three, i.e. any background in the spectrum, that can be approximated by a quadratic polynomial function, does not contribute to the wavelet coefficients. A detailed description of the application of wavelet to spectra of nuclear giant resonances can be found in [88].

6.1.2 Characteristic scales in the IVGDR in ^{208}Pb

In the following, we apply a CWT analysis to the ^{208}Pb(p,p′) excitation spectrum for scattering angles $\Theta = 0° - 0.94°$. The excitation energy region below 8 MeV is excluded from the analysis because of the influence of the strong peaks in the PDR region on the data analysis. In order to search for characteristic scales, it is helpful to construct the power spectrum of the signal, *i.e.* the projection of the absolute values of the wavelet coefficients on the scale axis. Aiming a better resolution, one can make such projections for different excitation energy intervals, so that different scales do not interfere with each other. In Fig. 6.3 the excitation energy spectrum (upper right) and corresponding wavelet transforms (middle and lower right) are plotted. For a better recognition of the characteristic scales that correspond to the maxima of the absolute values of the wavelet coefficients, power spectra are plotted (middle- and lower-left). The middle panel shows the scale region up to 3.5 MeV, while the lower panel gives an enlarged view of the region below 1 MeV. Characteristic scales are clearly visible in the power spectra indicated by arrows. It should be noted that the extracted scales are converted into the full width at half maximum of a Gaussian function, as described in [83]. The conversion factor for the Morlet wavelet have been empirically established from artificial spectra where all scales are known. White regions indicate the smallest values of the wavelet coefficients, while dark ones denote maxima, *i.e.* characteristic scales. Together with the dominating scales at 2.1 and 1.1 MeV, there is a prominent characteristic scale at 520 keV, visible over the whole resonance. Two scales at 100 and 320 keV are visible only between 9 and 12 MeV. The characteristic scale corresponding to the width of the resonance located at around 3.6 MeV is not shown for a better visibility of other scales. The smallest scale at 30 keV corresponds to the experimental energy resolution.

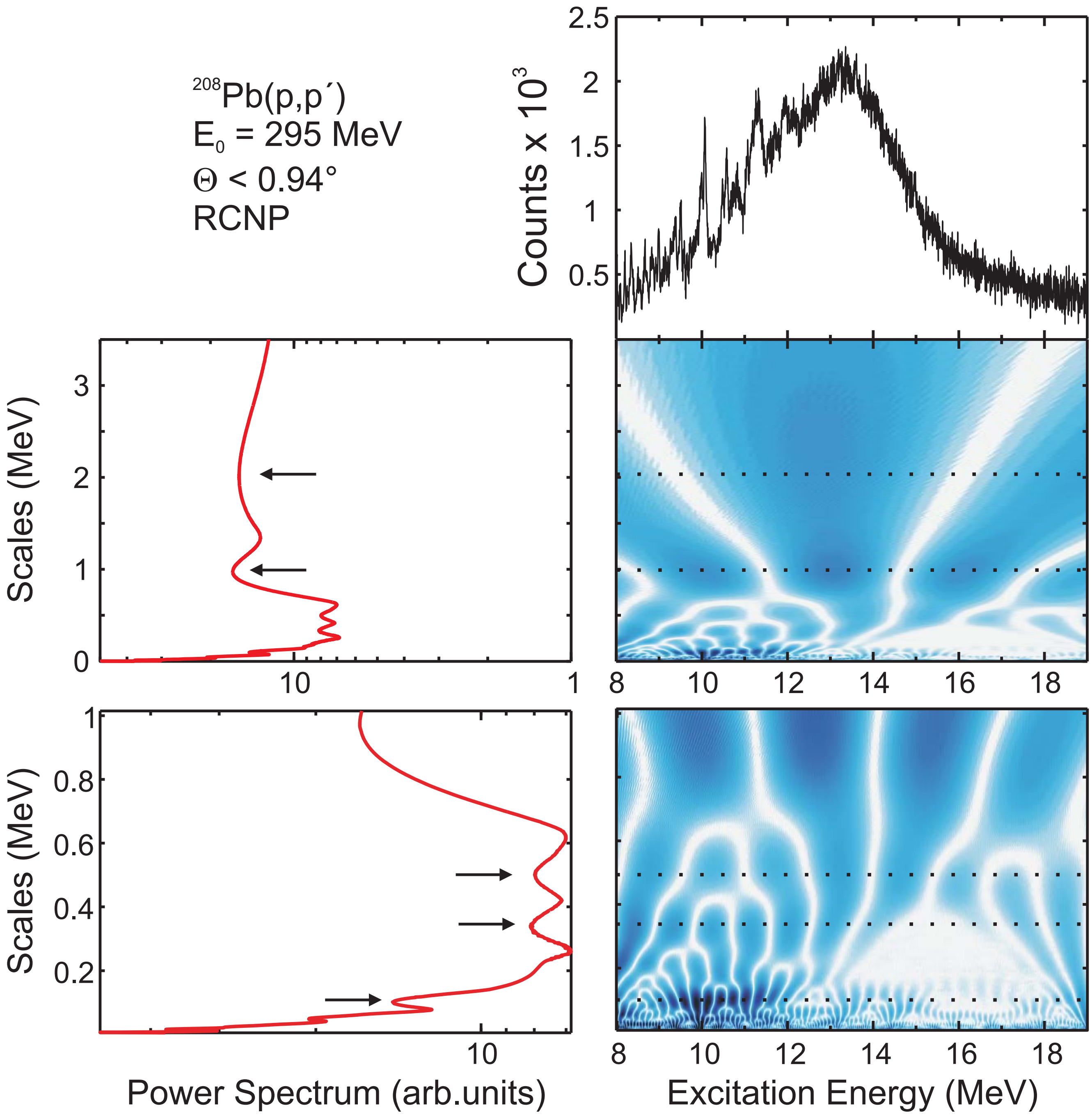

Fig. 6.3: CWT analysis of the excitation energy spectrum of the ^{208}Pb(p,p') reaction at E$_0$=295 MeV for Θ_{lab} <0.94°. Top-right: The spectrum of the reaction in the GDR region. Middle: Absolute values of the wavelet coefficients (right) and power spectrum (left). Bottom: Enlarged picture for the region of scales below 1 MeV. Characteristic scales are marked with arrows. White color corresponds to smallest wavelet coefficients, while dark regions indicate the largest values. Dotted lines are guides to the eye for the scales positions.

In order to understand the origin of the characteristic energy scales obtained from the experimental data one needs a comparison with the results from microscopic calculations. The

Tab. 6.1: Characteristic scales (in keV) of the GDR in ^{208}Pb extracted from the wavelet analysis of the experimental data, and the QPM and RQTBA calculations.

	I	II	III	IV	V
Exp.	100	340	550	1000	2100
QPM	100	270	580	1200	1800
RQTBA	170	450		1100	1850

results of the CWT analysis for the QPM and RQTBA calculations of the electric dipole response in ^{208}Pb are presented in Fig. 6.4(a) and Fig. 6.4(b), respectively. Five scales are observed in the QPM calculations and four in RQTBA. A summary of the extracted characteristic scales is given in Tab. 6.1. Clearly, both models reproduce the experimental data reasonably good. The RQTBA predictions rather overestimate lower scales and miss the scale at around 500 keV, while QPM reproduces the experimental data very well. A detailed comparison of the experimental power spectrum with those of QPM and RQTBA calculations is shown in Fig. 6.5. The region of scales is enlarged relative to the full range of the GDR, omitting the largest scale corresponding to the width of the resonance. It provides a quantitative measure for the ability of different models to describe fine structure and characteristic scales.

In order to extract information on the dominant damping mechanism, a CWT analysis of the QPM calculations including only 1-phonon transitions are performed (see Fig. 6.5(d)). The GDR strength is not concentrated in a single transitions, as observed e.g. in the case of the GQR. For ^{208}Pb it contains more than five states, so that the response function shows a fine structure already on the RPA level. Accordingly, the wavelet analysis of the RPA result does detect characteristic scales, beyond a trivial scale - a folding width of 30 keV, included for the comparison with experiment. Since the deduced characteristic scales are very similar to the QPM results including 2-phonon states, one can conclude that Landau damping is the most important mechanism leading to fine structure, while the coupling to low-lying collective vibrations identified as dominant mechanism in the GQR in heavy nuclei [183] seems to play a minor role only.

6.2 Extraction of the level densities

In this chapter the level density of 1^- states in ^{208}Pb is extracted by means of a self-consistent procedure based on a fluctuation analysis in the excitation energy interval between 8 and 19 MeV. The values obtained are compared with different parametrizations of the Back-Shifted Fermi Gas (BSFG) model [135, 184] and with predictions from the constant temperature model [185, 186], with the microscopic calculations performed in the framework of the Hartree-Fock-Bogoliuvov (HFB) [187], and the Hartree-Fock-BCS approach [128].

6.2.1 Fluctuation analysis

To extract level densities from high-resolution spectra, a fluctuation analysis can be utilized. It was originally proposed to analyze β-delayed particle emission spectra [188]. Detailed descriptions of the method can also be found in [90, 189]. Later it was successfully adopted for the study of electron scattering data [190, 191] and it can be used in general for high-resolution spectra for nuclear reactions [90]. The main idea of the analysis is to take advantage of the autocorrelation function in order to obtain a measure of the cross-section fluctuations with respect

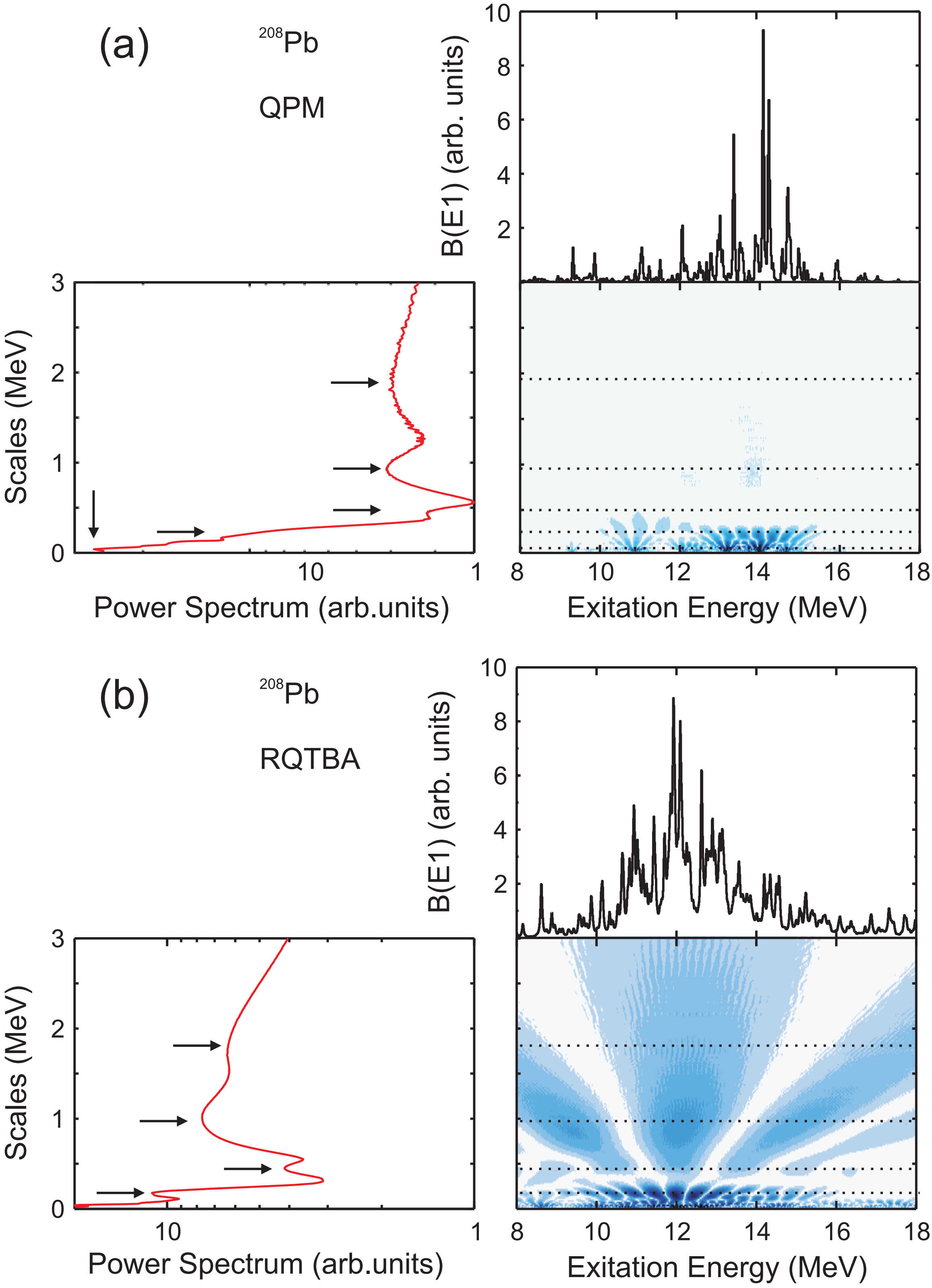

Fig. 6.4: CWT analysis of the GDR strength distribution from QPM (a) and RQTBA (b) calculations. White color corresponds to the smallest values of the wavelet coefficients, while dark one shows the maximum. Dashed lines guides the eye for a scale positions.

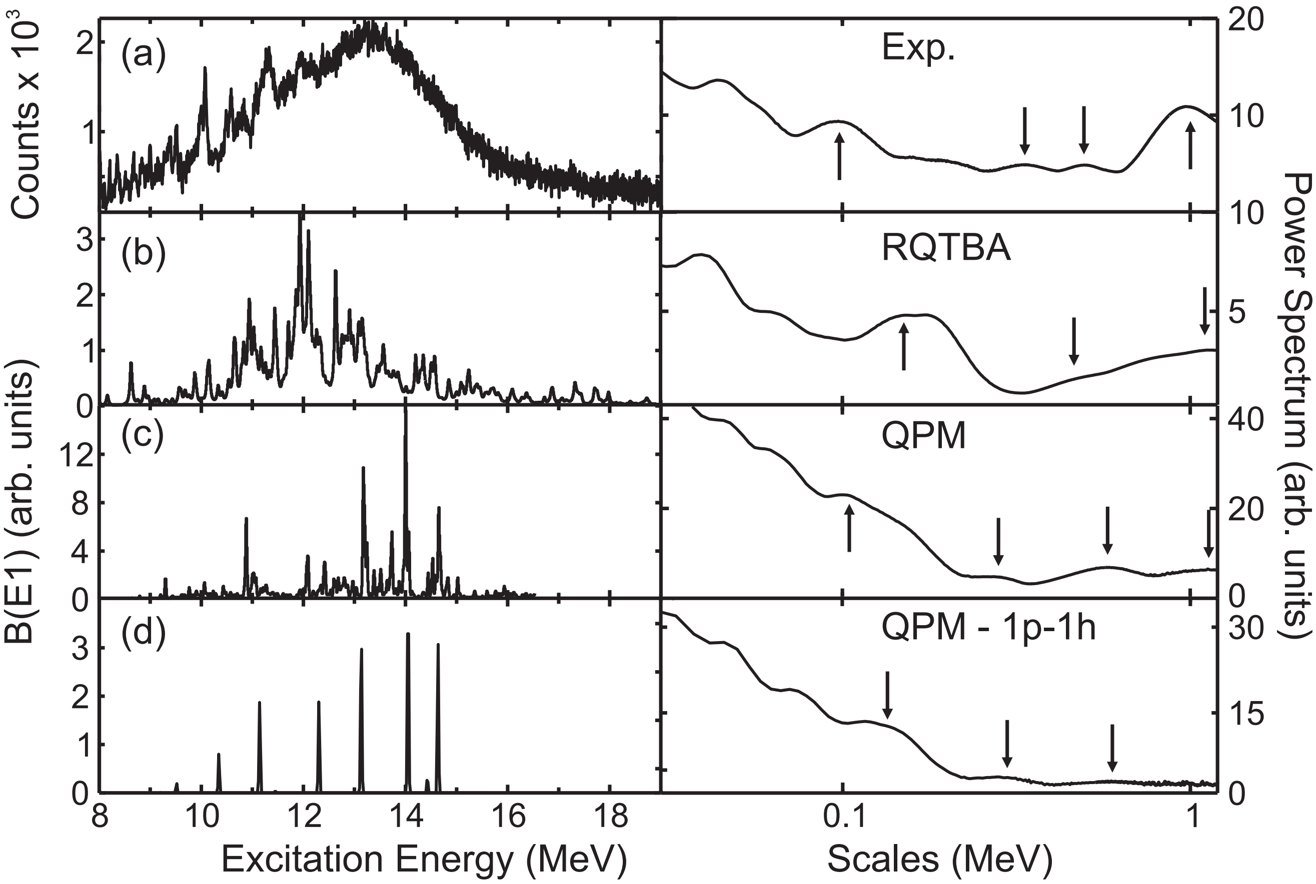

Fig. 6.5: The experimental spectrum together with the power spectrum from the CWT analysis (a) in comparison with RQTBA (b) and QPM predictions including 2-phonon configurations (c) and $1p - 1h$ ones (d). Characteristic scales are marked by arrows.

to a stationary mean value. In an energy region where the mean level spacing is smaller than the experimental energy resolution one has to distinguish between two possible cases:

- $\langle \Gamma \rangle \leq \langle D \rangle$, *i.e.* the mean level width $\langle \Gamma \rangle$ is smaller than the average distance between levels $\langle D \rangle$ and fluctuations result from the high density of non-resolved states and their incoherent overlap.
- $\langle \Gamma \rangle > \langle D \rangle$, so-called Ericson fluctuations [136], which result from the coherent overlapping of the states.

In principle, it is possible to utilize the method even in the Ericson regime, but the statistics has to be very high in this case [192]. Thus, in practice one is usually limited to the first region $\langle \Gamma \rangle \leq \langle D \rangle$. The application of the fluctuation analysis is based on the following two assumptions:

- In an highly-excited nucleus, the probability for a given spacing between states with the same spin and parity is given by the Wigner distribution [193]

$$P_W(s) = \frac{\pi s}{2} \exp\left(-\frac{\pi s^2}{4}\right), \tag{6.6}$$

with

$$s = \frac{D}{\langle D \rangle} . \tag{6.7}$$

This distribution has a maximum close to the mean value and shows a suppression of small distances between neighboring levels.

- The ground state decay widths or transition strengths obey a Porter-Thomas distribution [194]

$$P_{PT}(s) = \frac{1}{\sqrt{2\pi s}} \exp\left(-\frac{s}{2}\right), \quad \text{with } s = \frac{\Gamma_0}{\langle\Gamma_0\rangle}. \tag{6.8}$$

These assumptions are adopted from random matrix theory (RMT) [195] and based on the observation that they provide a good description of nuclear excitations in the vicinity of the neutron separation energy [196].

The procedure of the fluctuation analysis for the $^{208}\mathrm{Pb}(p,p')$ scattering data at 0° is schematically demonstrated in Fig. 6.6. It can be divided in four main steps. In order to obtain a spectrum

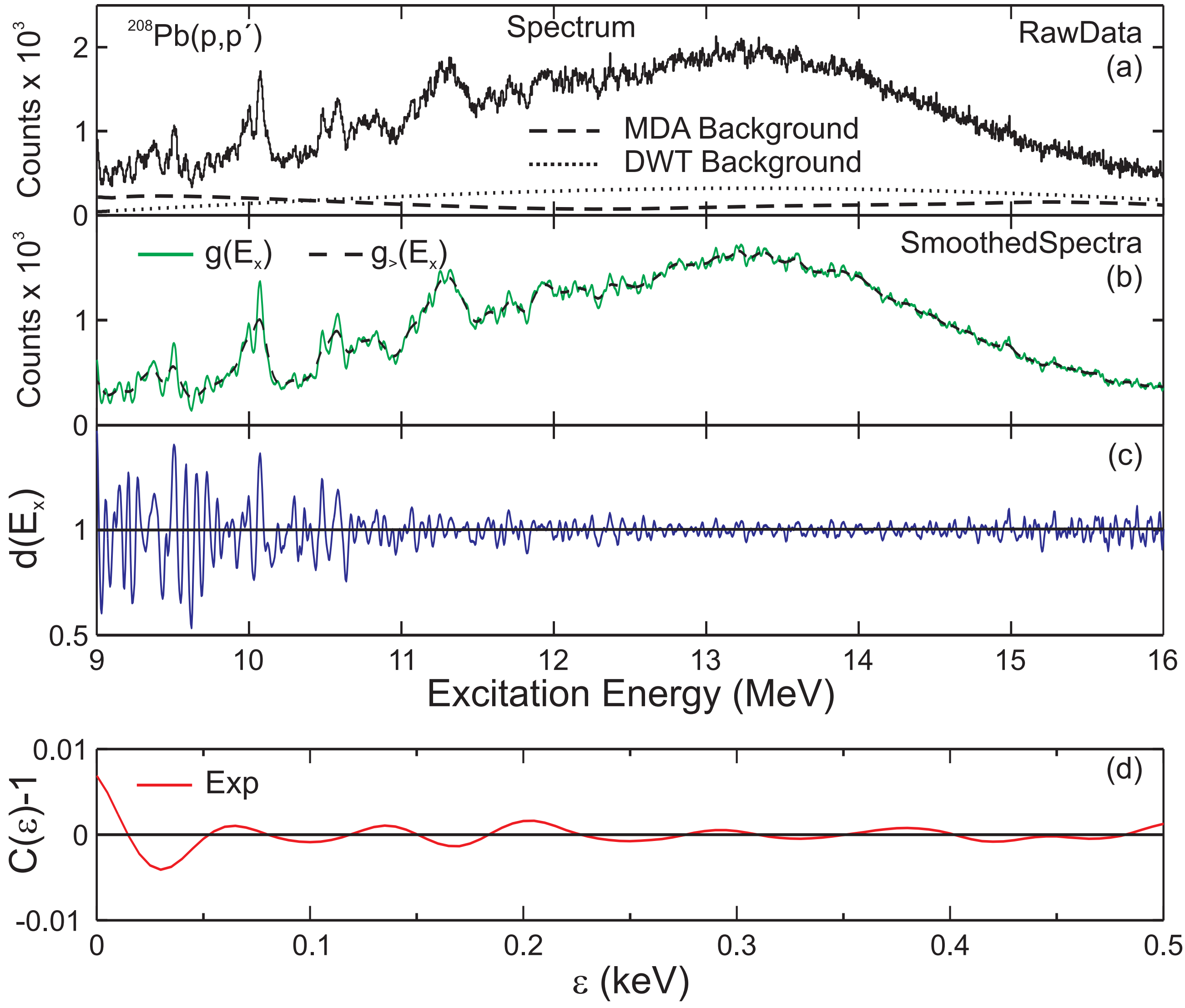

Fig. 6.6: From top to bottom: Spectrum of the $^{208}\mathrm{Pb}(p,p')$ reaction at E_p=295 MeV for Θ=0° - 0.94° and the background obtained from MDA (dashed line) and DWT (dotted line); background-subtracted smoothed spectra $g(E_x)$ and $g_>(E_x)$; stationary spectrum $d(E_x)$; experimental autocorrelation function.

containing only the information needed, one has to subtract any background not arising from excitations of the nuclear mode under investigation. Methods to determine this background are discussed in Sec. 6.2.2. After background subtraction, the spectrum contains the information on the nuclear excitation fluctuations. In order to eliminate the fluctuations arising from finite statistics, the spectrum is folded with a Gaussian function with the width σ chosen to be smaller than the experimental energy resolution. The resulting spectrum is called $g(E_x)$ hereafter. Similarly, a second spectrum $g_>(E_x)$ is created by the convolution with a Gaussian function, whose width $\sigma_>$ is at least two times larger than the energy resolution in the experiment in order to remove gross structures from the spectrum. The resulting spectra $g(E_x)$ and $g_>(E_x)$ are shown in in Fig. 6.6(b). The dimensionless stationary spectrum $d(E_x)$ defined as

$$d\left(E_x\right) = \frac{g\left(E_x\right)}{g_>\left(E_x\right)} \tag{6.9}$$

is shown in Fig. 6.6(c). As a result the normalization on the local mean value, the energy dependence of the cross sections vanishes. The value of $d(E_x)$ is sensitive to the fine structure of the spectrum and distributed around an average intensity $\langle d(E_x)\rangle = 1$. With increasing the excitation energy, the mean level spacing is decreasing, and in turn, the oscillations in $d(E_x)$ are damped. A quantitative description of the fluctuations is given by the autocorrelation function

$$C\left(\epsilon\right) = \frac{\left\langle d\left(E_x\right) \cdot d\left(E_x + \epsilon\right)\right\rangle}{\left\langle d\left(E_x\right)\right\rangle \cdot \left\langle d\left(E_x + \epsilon\right)\right\rangle} \, . \tag{6.10}$$

The value $C(\epsilon = 0) - 1$ is nothing but the variance, since

$$C\left(\epsilon = 0\right) - 1 = \frac{\left\langle d^2\left(E_x\right)\right\rangle - \left\langle d\left(E_x\right)\right\rangle^2}{\left\langle d\left(E_x\right)\right\rangle^2} \, . \tag{6.11}$$

According to [188], this experimental autocorrelation function shown in Fig. 6.6(d) can be approximated by the expression

$$\begin{aligned} C(\epsilon) - 1 \;=\; & \frac{\alpha \cdot \langle \mathrm{D} \rangle}{2\sigma\sqrt{\pi}} \times \left\{ \exp\left(-\frac{\epsilon^2}{4\sigma^2}\right) + \frac{1}{y} \cdot \exp\left(-\frac{\epsilon^2}{4\sigma^2 y^2}\right) - \right. \\ & \left. \sqrt{\frac{8}{1+y^2}} \cdot \exp\left(-\frac{\epsilon^2}{4\sigma^2(1+y^2)}\right) \right\} , \end{aligned} \tag{6.12}$$

with

$$y = \frac{\sigma_>}{\sigma} \, . \tag{6.13}$$

The value α is the sum of the normalized variances of the assumed spacing and transition width distributions

$$\alpha = \alpha_D + \alpha_I \, . \tag{6.14}$$

If only one type of the transitions J^π contributes to the spectrum, then α can be directly determined as the sum of the variances of the Wigner and Porter-Thomas distributions, $\alpha = \alpha_W + \alpha_{PT} = 0.273 + 2.0$. The mean level spacing $\langle D \rangle$ is proportional to the variance of $d(E_X)$ and can be extracted from the value $C(\epsilon = 0)$ - 1. The nuclear level density can be determined from the mean level spacing as $\rho(E) = 1/\langle D \rangle$.

Uncertainties in the extracted values of $\langle D \rangle$ result from the following sources:

- statistical errors,
- neglect of states of different J^π or inaccuracy in the background definition,
- the widths of the smoothing functions,
- the length of the energy interval.

Statistical errors are negligible because of the smearing of the spectra, as discussed above. Transitions of other multipolarities are supposed to be included into the background. The choice of σ and $\sigma_>$ gives rise to uncertainties in the mean level spacing which are about 5%. In preliminary investigations it has been found that the most stable results are obtained by setting $\sigma = 0.5 \cdot \Delta E$ and $\sigma_>/\sigma = 2.5 - 3.5$. This finding is in agreement with the results of [191]. The length of the interval is important, since too short intervals would result in errors in the autocorrelation functions because of the finite number of data points. On the other hand, the real exponential energy dependence of the level spacing is replaced by a linear one in the analysis that is a good approximation for sufficiently small ranges only. The value of 0.5 MeV chosen in this study seems to be a good compromise.

6.2.2 Background determination

In the further analysis background obtained by two independent ways was used. Firstly, the background resulting from the multipole decomposition analysis as described in Sec. 5.2.1, which includes a phenomenological part at higher excitation energies and the contributions from the GQR in the lower excitation energy region, was utilized. It is shown as dashed line in Fig. 6.6(a). The second method to eliminate the background is based on the features of the DWT. It was shown in [79], that the property of vanishing moments of the wavelets allows a model-independent background determination. If the wavelet function has a sufficient number of vanishing moments and the background can be described by a smooth polynomial function of low order, then all non-resonant components are always found in the approximations, while details include the information on the fluctuations. Therefore, at some stage of the decomposition the approximation corresponds to the background and does not carry any information on the fine structure.

In Fig. 6.7 the decomposition of the excitation energy spectrum of the ^{208}Pb(p,p') reaction into the approximations A_i and details D_i is shown. The largest extracted scale in the spectrum correspond to the total width of the GDR described by the approximation A_9. Thus, the next approximation A_{10} can be considered as a non-resonant contribution to the spectrum and the corresponding curve is shown in Fig. 6.6(a) as dotted line. The analysis is repeated independently for different angle bins. Since the background shows a different angular dependence than the electric dipole strength, the requirement of a constant level density in all spectra further constrains the analysis and confirms the validity of the chosen background shape. Figure 6.8 displays the background shapes determined by means of the DWT analysis for three different scattering angle cuts at the 0° setting of the Grand Raiden spectrometer.

6.2.3 Level densities of $J^\pi = 1^-$ states in the giant dipole resonance region

In Fig. 6.9 the experimentally observed level densities of 1^- states in ^{208}Pb determined with the two different approaches for the background subtraction are compared with values calculated within the different models described in Sec. 6.2. For the fluctuation analysis the interval between 8.5 MeV and 16 MeV has been split into subintervals of 0.5 MeV each. The mean level spacing has been determined in each bin. The experimentally obtained level densities are

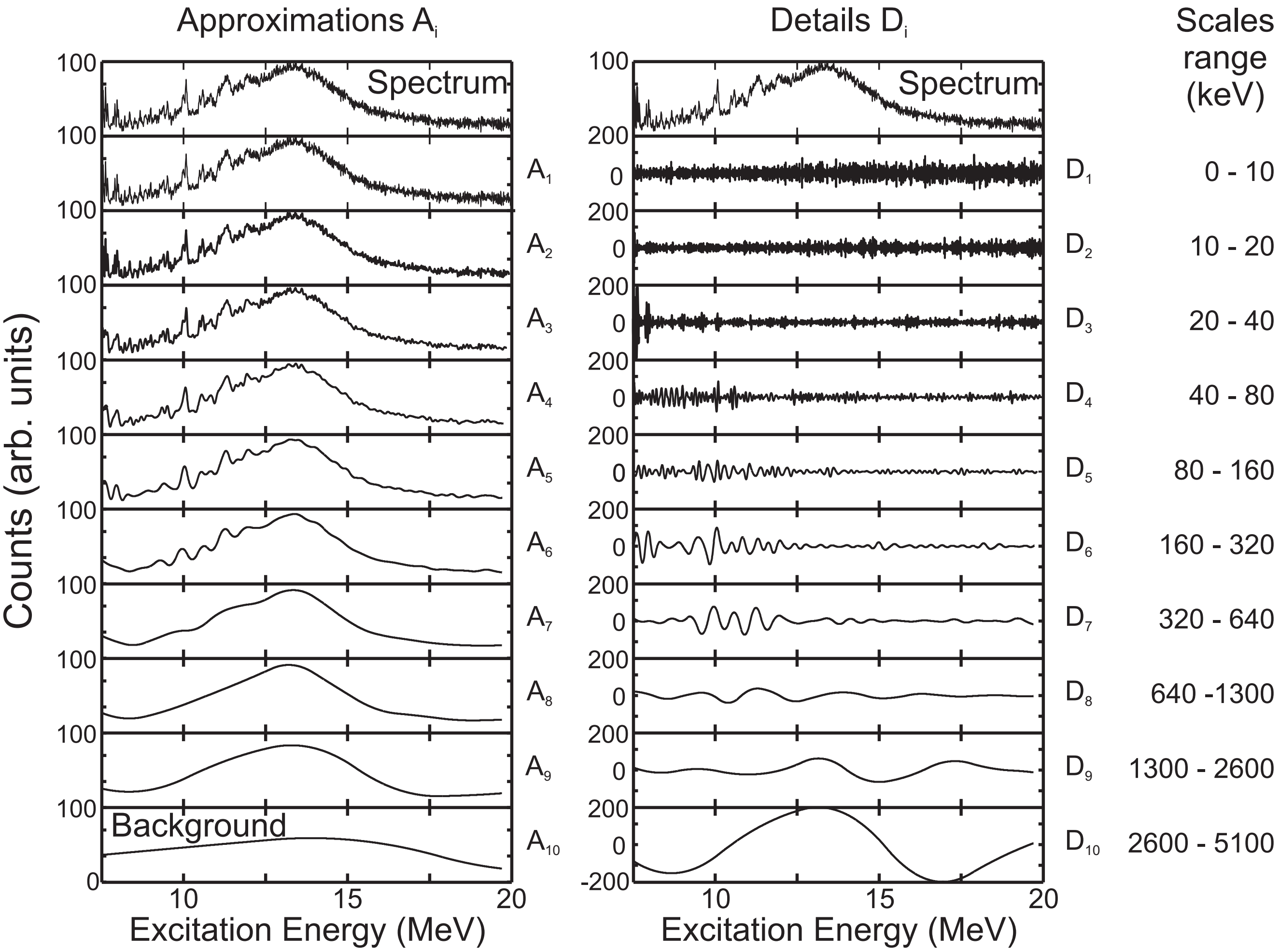

Fig. 6.7: Decomposition of the ^{208}Pb(p,p') spectrum with the DWT analysis into approximations A_i and details D_i. The approximation A_9 describes the total width of the GDR, thus A_{10} can be adopted as background shape.

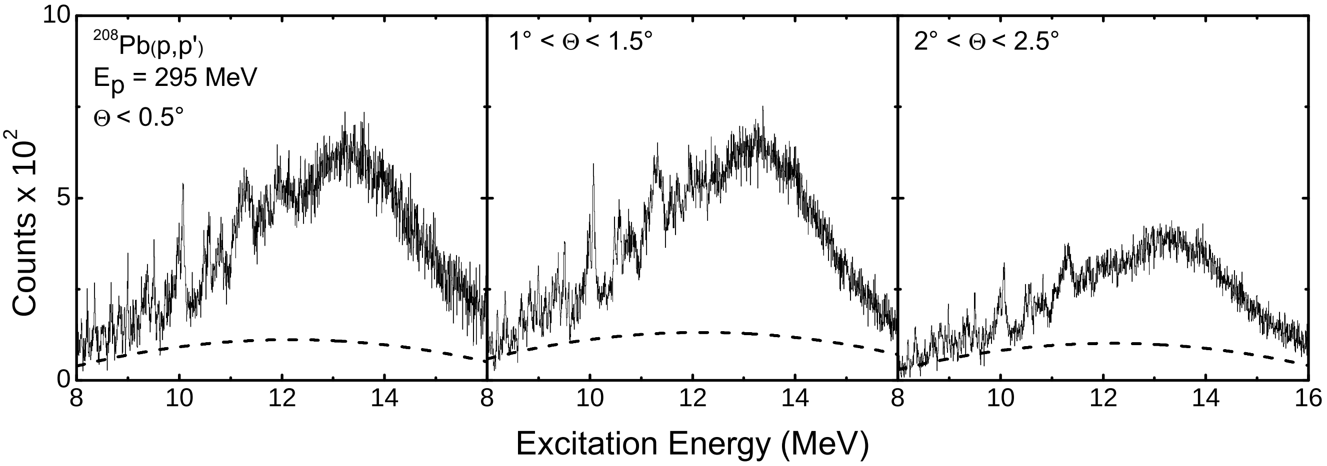

Fig. 6.8: Excitation energy spectra of the ^{208}Pb(p,p′) reaction measured at 0° setting of the Grand Raiden spectrometer for different scattering angle cuts. The dashed lines show background exctracted by means of the DWT.

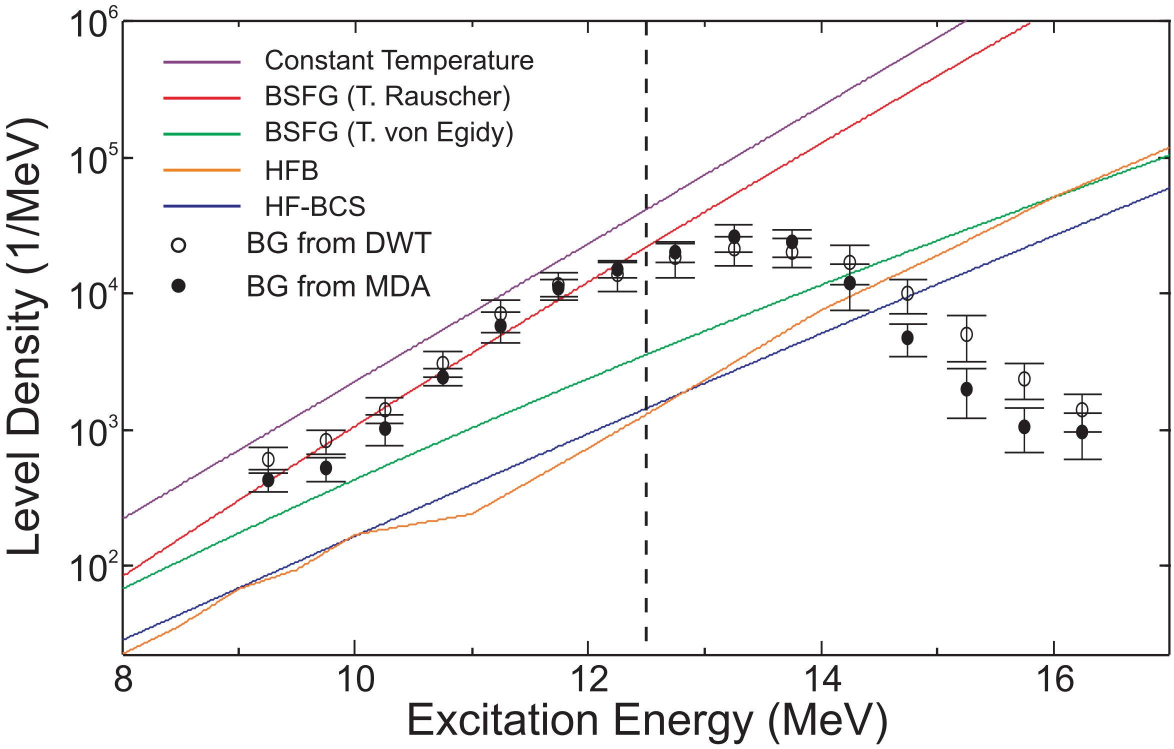

Fig. 6.9: Comparison of the experimentally obtained level densities for 1^- states in ^{208}Pb in the energy range from 8.5 to 16 MeV with predictions from BSFG using the model of [135] (red line) or from [185] (green line), constant temperature model [186] (purple line), HFB-BCS [128] (blue line) and HFB [187] (orange line). The dashed line shows the limit in excitation energy of the applicability of the fluctuation analysis.

in good agrement with the BSFG parametrization from [135]. The CT model from [186] reproduces correctly the energy dependence but gives two times higher level densities, while all other models fail to he magnitude and the energy dependence of the experimental data. Not sufficient statistics in the experimental spectrum or the onset of of the Ericson fluctuations in the excitation energy region above 12 MeV can be responsible for the drop-down of experimentally deduced level densities. The phenomenon has also been observed in the analysis of M2 resonances in 180° electron scattering [191]. The consistency check of the analysis using different angles suggests an upper limit of the applicability of the fluctuation analysis method in the present case indicated by the dashed line in Fig. 6.9.

7 Summary and outlook

The present thesis reports on a measurements of the dipole strength distributions, both electric and magnetic, in ^{208}Pb. Proton scattering at and close 0° at energies of a few hundred MeV is established as a new experimental tool allowing for an extraction of the complete E1 strength up to about 20 MeV. Dispersion matching techniques enable high resolution measurements reaching ΔE = 25 - 30 keV (FWHM). Furthermore, polarization observables were measured to distinguish spinflip and non-spinflip transitions. The emphasis of the present thesis was placed on the extraction of the information on the complete electric dipole strength distribution and related quantities such as the electric dipole polarizability, photon strength function. The high energy resolution furthermore enables an extraction of level densities of 1^- states and the study of characteristic scales of the IVGDR fine structure.

Two independent methods were applied to differentiate between electric and magnetic dipole excitations in the measured spectra, viz. a multipole decomposition analysis based on the cross section angular distributions, and alternatively a study of the total spin transfer based on measured polarization transfer coefficients. The results of both methods show excellent agreement within the uncertainties.

The B(E1) strength distribution was determined in the excitation energy region from 4.8 to 20 MeV, assuming Coulomb excitation of the 1^- states. These data provide an unique opportunity to study the pygmy dipole resonance as well as isovector giant dipole resonance structure simultaneously. Below the neutron separation energy, reduced transition probabilities for 1^- states are in a very good agreement with the data from the nuclear resonance fluorescence experiments [28, 29, 30, 31]. However, in the energy range from the neutron threshold to 9 MeV additional strength, compared to data from $^{208}\mathrm{Pb}(\gamma,\gamma')$ and $^{207}\mathrm{Pb}(n,\gamma)$ [158] reactions is observed in the present work. In the PDR region, assumed to be between 6.2 MeV and 8.2 MeV, the total B(E1) strength in ^{208}Pb amounts to (1.54±16) e^2fm^2 with a centroid energy E_c=7.43(2) MeV. The total gamma absorption cross sections in the energy region up to 20 MeV were extracted. Results in the excitation region of the GDR are in the excellent agreement with previous (γ, xn) data from the Saclay group [168] and total nuclear photon absorption experiment [170]. The deduced B(E1) strength distribution was compared to the theoretical models calculations, such as QPM and RQTBA, allowing for complex configurations beyond the $1p-1h$ doorway states and aiming at a detailed picture of the structure of the low-lying dipole strengths and the GDR. The comparison reveals problems: the PDR strength is either under- or overpredicted, the GDR centroid is not correct for the RQTBA, and the width of the resonance is only partially described.

The static nuclear dipole polarizability α_D of ^{208}Pb is of particular interest, because of the strong correlation between the dipole polarizability and the neutron skin thickness predicted by recent theoretical investigations [38, 39]. A significant result of the present work is a highly precise value of α_D that is of highest important for the determination of the neutron skin. The value α_D averaged over all available data, including the present work, is (18.9±0.5) fm^3/e^2 in the energy region up to 19 MeV, that improves previous uncertainties a lot.

Another important aspect in studies of the dipole response below and above the particle emission threshold is in the extraction of the photon strength function, especially around the neutron threshold, where large discrepancies between different experimental methods occur. A comparison of the present PSF to one obtained using the Oslo method, based on the compound nucleus reaction (^{3}He, ^{3}He'γ) [175], can provide an information on the validity of the Axel-Brink hypothesis [46]. However, a more detailed investigation of the available data is still needed for this purpose.

In order to understand the physical nature of the fine structure of the GDR and to extract its energy scales, a novel method, based on a wavelet transform analysis, was applied. It gives model-independent information on the scales and their localization in the energy spectrum. By the comparison of the experimental data to QPM and RQTBA predictions, one can gain information on the dominant damping mechanism. The results suggest that Landau damping known to be important in light nuclei, persists as dominant damping mechanism in a nucleus as heavy as ^{208}Pb.

The data allow an extraction of spin- and parity-separated level densities of 1^- states in ^{208}Pb in the GDR region. This is achieved by means of a fluctuation analysis. Both the background, which is supposed to include all contributions of multipolarities other than $\Delta L = 1$, and the level densities have been obtained in a self-consistent way using the fact that level density is an intrinsic feature of the nucleus. A version of the BSFG model allowing for additional phenomenological parameters in local mass regions describes the experimental results well, while a global BSFG parametrization fails. The constant temperature model gives a correct energy dependence, but the absolute LDs are of factor of two too large. Microscopic models predict too small LDs and a wrong energy dependence.

After establishing this new experimental tool by the case study on ^{208}Pb, it can be applied to many important questions including

- E1 strength in the tin isotope chain, where data from stable and very neutron-rich unstable nuclei can be combined. The data analysis of an experiment on ^{120}Sn is underway.
- Systematics of α_D and the PDR strength as a test of the predicted relation to the neutron skin thickness and the density dependence of the symmetry energy.
- Explanation of discrepancies in PSF deduced from different experiments, in particular a test of the Axel-Brink hypothesis by comparison to γ-decay of compound nuclei. The present experimental technique is particularly suited because it does not only provide f^{E1}, but also strong constraints on the LD to be used in the analysis of γ-decay experiments.
- Role of deformation
  - a double-hump structure of spin M1 resonance [60], whose interpretation is unclear.
  - properties of the PDR in a well-deformed heavy nucleus, where nothing is known.

  A RCNP experimental proposal to measure ^{154}Sm is approved and will be conducted in May 2011.

A B(E1) strengths and photoabsorption cross sections in ^{208}Pb.

B(E1) strengths observed in photon scattering experiments of [28, 29, 30, 31].

Tab. A.1: B(E1) strengths observed in ^{208}Pb(γ,γ') reactions.

E_x, MeV	Ref. [28] B(E1), 10^{-3} e^2fm^2	Ref. [29] B(E1), 10^{-3} e^2fm^2	Ref. [30] B(E1), 10^{-3} e^2fm^2	Ref. [31] B(E1), 10^{-3} e^2fm^2
4.8413(12)	121(8)	126.5(136)	116(21)	111.7(129)
5.2921(11)	122(8)	107.9(114)	106(17)	112.0(128)
5.5119(11)	484(36)	381.0(40)	394(61)	381.3(442)
5.9470(4)	15.4(16)	11.8(27)	15(3)	9.4(23)
6.2635(4)	48.6(63)	27.9(32)	47(9)	33.4(42)
6.3130(10)	38(59)	30.4(42)	35(8)	47.2(56)
6.3623(4)	22.8(41)	17.4(24)	23(6)	16.8(23)
6.4860(10)	3(1)	8.0(23)	3.3(14)	
6.7198(6)	41.3(235)	93.7(100)	78(13)	101.5(117)
7.0634(5)		140.6(150)	129(20)	153.9(179)
7.0834(4)		76.6(83)	70(11)	86.9(104)
7.1785(2)		7.9(17)		6.8(16)
7.2069(2)				3.9(12)
7.2433(6)		8.5(16)	6.7(24)	13.9(51)
7.2805(2)		17.5(24)		
7.3326(5)		213.2(225)	190(29)	244.0(278)
7.5490(3)		85.2(13)		6.5(13)
7.9130(33)		44.2(15)		

Photoabsorption cross sections extracted from the present work using proton scattering at 0° and Ref. [168, 170] with (γ,xn) and (γ,all) reactions, respectively.

Tab. A.2: Photoabsorption cross section from ^{208}Pb($\vec{p}$,$\vec{p}'$) reaction (present work), (γ,xn) experiment [168] and (γ,all) measurements [170].

Present work					
E_x, MeV	σ_{abs}, mb	E_x, MeV	σ_{abs}, mb	E_x, MeV	σ_{abs}, mb
9.000 - 9.200	53.0(37)	12.800 - 13.000	561.90(330)	16.600 - 16.800	202.38(258)
9.200 - 9.400	74.4(44)	13.000 - 13.200	618.70(380)	16.800 - 17.000	190.44(254)
9.400 - 9.600	82.6(49)	13.200 - 13.400	660.56(386)	17.000 - 17.200	169.90(280)
9.600 - 9.800	68.0(42)	13.400 - 13.600	652.78(368)	17.200 - 17.400	158.77(237)
9.800 - 10.000	113.4(69)	13.600 - 13.800	642.13(333)	17.400 - 17.600	152.56(216)

Continued on next page...

Tab. A.2 – Continued

E_x, MeV	σ_{abs}, mb	E_x, MeV	σ_{abs}, mb	E_x, MeV	σ_{abs}, mb
10.000 - 10.200	146.1(88)	13.800 - 14.000	654.57(337)	17.600 - 17.800	131.60(320)
10.200 - 10.400	96.6(57)	14.000 - 14.200	621.15(245)	17.800 - 18.000	119.98(288)
10.400 - 10.600	159.30(100)	14.200 - 14.400	577.98(248)	18.000 - 18.200	121.00(250)
10.600 - 10.800	171.64(104)	14.400 - 14.600	540.29(179)	18.200 - 18.400	118.03(253)
10.800 - 11.000	177.42(112)	14.600 - 14.800	495.84(134)	18.400 - 18.600	108.36(256)
11.000 - 11.200	245.12(162)	14.800 - 15.000	454.27(157)	18.600 - 18.800	108.28(328)
11.200 - 11.400	332.30(210)	15.000 - 15.200	393.66(176)	18.800 - 19.000	103.49(139)
11.400 - 11.600	295.94(184)	15.200 - 15.400	365.52(172)	19.000 - 19.200	88.4(141)
11.600 - 11.800	324.25(205)	15.400 - 15.600	353.40(130)	19.200 - 19.400	75.6(62)
11.800 - 12.000	375.61(241)	15.600 - 15.800	286.14(144)	19.400 - 19.600	91.5(156)
12.000 - 12.200	403.63(253)	15.800 - 16.000	269.94(144)	19.600 - 19.800	76.3(185)
12.200 - 12.400	421.93(273)	16.000 - 16.200	239.75(185)	19.800 - 20.000	78.8(155)
12.400 - 12.600	459.29(279)	16.200 - 16.400	224.95(215)	20.000 - 20.200	67.4(102)
12.600 - 12.800	508.80(310)	16.400 - 16.600	224.84(224)	20.200 - 20.400	58.5(102)

Ref. [168]

E_x, MeV	σ_{abs}, mb	E_x, MeV	σ_{abs}, mb	E_x, MeV	σ_{abs}, mb
7.35 - 7.65	22.9(22)	11.85 - 12.15	413.4(45)	16.35 - 16.65	207.1(157)
7.65 - 7.95	26.3(18)	12.15 - 12.45	458.7(51)	16.65 - 16.95	186.5(154)
7.95 - 8.25	28.9(19)	12.45 - 12.75	520.9(61)	16.95 - 17.25	167.8(156)
8.25 - 8.55	31.3(21)	12.75 - 13.05	580.6(122)	17.25 - 17.55	149.8(158)
8.55 - 8.85	36.2(25)	13.05 - 13.35	623.4(131)	17.55 - 17.85	137.3(159)
8.85 - 9.15	47.6(27)	13.35 - 13.65	635.6(146)	17.85 - 18.15	127.0(160)
9.15 - 9.45	63.4(30)	13.65 - 13.95	620.3(136)	18.15 - 18.45	115.3(162)
9.45 - 9.75	80.8(31)	13.95 - 14.25	589.9(135)	18.45 - 18.75	105.4(162)
9.75 - 10.05	106.4(33)	14.25 - 14.55	536.4(133)	18.75 - 19.05	97.1(167)
10.05 - 10.35	123.6(35)	14.55 - 14.85	475.7(141)	19.05 - 19.35	89.3(172)
10.35 - 10.65	158.6(37)	14.85 - 15.15	420.6(142)	19.35 - 19.65	80.4(173)
10.65 - 10.95	206.2(38)	15.15 - 15.45	363.4(149)	19.65 - 19.95	74.9(175)
10.95 - 11.25	272.2(40)	15.45 - 15.75	317.6(152)	19.95 - 20.25	74.5(176)
11.25 - 11.55	316.1(41)	15.75 - 16.05	272.4(151)	20.25 - 20.55	72.2(177)
11.55 - 11.85	363.7(42)	16.05 - 16.35	234.7(156)	20.55 - 20.85	67.9(190)

Ref. [170]

E_x, MeV	σ_{abs}, mb	E_x, MeV	σ_{abs}, mb	E_x, MeV	σ_{abs}, mb
9.58	66.6(58)	11.82	408.0(98)	14.78	463.8(92)
9.73	79.4(42)	11.96	420.0(66)	15.06	398.6(187)

Continued on next page...

Tab. A.2 – Continued

E_x, MeV	σ_{abs}, mb	E_x, MeV	σ_{abs}, mb	E_x, MeV	σ_{abs}, mb
9.81	114.4(50)	12.09	435.2(74)	15.34	350.9(179)
9.93	133.6(50)	12.19	462.3(90)	15.66	310.4(211)
10.05	112.9(74)	12.45	516.5(99)	15.94	265.1(203)
10.20	101.0(82)	12.66	533.3(91)	16.22	225.3(196)
10.35	131.3(90)	12.77	562.0(107)	16.51	207.9(180)
10.45	165.6(106)	12.87	592.3(83)	16.76	184.9(196)
10.68	184.0(82)	13.02	614.6(107)	17.04	171.4(204)
10.80	210.3(90)	13.18	644.2(107)	17.33	150.0(212)
10.98	243.8(90)	13.37	643.4(91)	17.58	141.3(212)
11.09	306.7(82)	13.45	638.7(67)	17.85	130.2(196)
11.19	312.3(98)	13.61	637.9(107)	18.13	123.9(196)
11.36	301.2(90)	13.76	629.2(115)	18.38	117.6(188)
11.48	321.9(90)	14.03	603.0(107)	18.65	108.1(205)
11.60	336.3(98)	14.23	570.4(107)	18.91	94.7(189)
11.72	388.9(106)	14.52	492.4(91)		

References

[1] M.N. Harakeh and A. van der Woude, *Giant resonances: fundamental high-frequency modes of nuclear excitation*, (Oxford University Press, Oxford, 2001).

[2] J. Speth and A. van der Woude, Rep. Prog. Phys. **44** (1981) 719.

[3] W. Bothe and W. Gentner, Z. Phys. **106** (1937) 236.

[4] G.C. Baldwin and G.S. Klaiber, Phys. Rev **71** (1947) 3.

[5] M. Goldhaber and E. Teller, Phys. Rev. **74** (1948) 1046.

[6] H. Steinwedel, J.H.D. Jensen, and P. Jensen, Phys. Rev. **79** (1950) 1019.

[7] G.E. Brown and M. Bolsterli, Phys. Rev. Lett. **3** (1959) 472.

[8] W. Andrejtscheff, C. Kohstall, P. von Brentano, C. Fransen, U. Kneissl, N. Pietralla, and H.H. Pitz, Phys. Lett. **B 506**, (2001) 239.

[9] P.O. Lipas, Nucl. Phys **A 573** (1994) 231.

[10] M. Wilhelm, E. Radermacher, A. Zilges, and P. von Brentano, Phys. Rev. **C 54** (1996) R449.

[11] G.A. Bartholomew, E.D. Earle, A.J. Ferguson, J.W. Knowles, M.A. Lone, Adv. Nucl. Phys. **7** (1972) 229.

[12] F.R. Metzger, *Resonance fluorescence in nuclei,* Progr. Nucl. Phys. **7** (1959) 54.

[13] T. Hartmann, M. Babilon, S. Kamerdzhiev, E. Litvinova, D. Savran, S. Volz, and A. Zilges, Phys. Rev. Lett. **93** (2004) 192501.

[14] S. Volz, N. Tsoneva, M. Babilon, M. Elvers, J. Hasper, R.-D. Herzberg, H. Lenske, K. Lindenberg, D. Savran, and A. Zilges, Nucl. Phys. **A 779** (2006) 1.

[15] D. Savran, M. Fritzsche, J. Hasper, K. Lindenberg, S. Müller, V.Yu. Ponomarev, K. Sonnabend, and A. Zilges, Phys. Rev. Lett. **100** (2008) 23501.

[16] P. Mohr, J. Enders, T. Hartmann, H. Kaiser, D. Schiesser, S. Schmitt, S. Volz, F. Wissel, and A. Zilges, Nucl. Instr. Meth. **A 423** (1999) 480.

[17] M. Erhard, A.R. Junghans, C. Nair, R. Schwengner, R. Beyer, J. Klug, K. Kosev, A. Wagner, and E. Grosse, Phys. Rev. **C 81**. (2010) 034319.

[18] G. Rusev, R. Schwengner, R. Beyer, M. Erhard, E. Grosse, A.R. Junghans, K. Kosev, C. Nair, K.D. Schilling, A. Wagner, F. Dönau, and S. Frauendorf, Phys. Rev. **C 79** (2009) 061302(R).

[19] R. Schwengner, G. Rusev, N. Tsoneva, N. Benouaret, R. Beyer, M. Erhard, E. Grosse, A.R. Junghans, J. Klug, K. Kosev, H. Lenske, C. Nair, K. D. Schilling, and A. Wagner, Phys. Rev. **C 78** (2008) 064312.

[20] R. Schwengner, R. Beyer, F. Dönau, E. Grosse, A. Hartmann, A.R. Junghans, S. Mallion, G. Rusev, K.D. Schilling, W. Schulze, A. Wagner, Nucl. Instr. Meth. **A 555** (2005) 211.

[21] K. Govaert, F. Bauwens, J. Bryssinck, D. De Frenne, E. Jacobs, W. Mondelaers, L. Govor, and V.Yu. Ponomarev, Phys. Rev. **C 57** (1998) 2229.

[22] B. Özel, *Study of the* ^{112,120}*Sn* (γ,γ') *reaction and systematics of the pygmy dipole resonance at the Z=50 shell closure*, Doctoral thesis, Çukurova University, Adana, Turkey (2008).
B. Özel, J. Enders, P. von Neumann-Cosel, I. Poltoratska, A. Richter, D. Savran, S. Volz, A. Zilges, Nucl. Phys. **A 788** (2007) 385.

[23] P. Adrich, A. Klimkiewicz, M. Fallot, K. Boretzky, T. Aumann, D. Cortina-Gil, U. Datta Pramanik, Th.W. Elze, H. Emling, H. Geissel, M. Hellström, K.L. Jones, J.V. Kratz, R. Kulessa, Y. Leifels, C. Nociforo, R. Palit, H. Simon, G. Surowka, K. Sümmerer, W. Walus, and the LAND-FRS Collaboration, Phys. Rev. Lett **95** (2005) 132501.

[24] A. Klimkiewicz, N. Paar, P. Adrich, M. Fallot, K. Boretzky, T. Aumann, D. Cortina-Gil, U. Datta Pramanik, Th.W. Elze, H. Emling, H.Geissel, M. Hellström, K.L. Jones, J.V. Kratz, R. Kulessa, C. Nociforo, R. Palit, H. Simon, G. Surowka, K. Sümmerer, D. Vretenar, and W. Walus for the LAND-FRS Collaboration, Phys. Rev. **C 76** (2007) 051603(R).

[25] M. Laszewski and P. Axel, Phys. Rev. **C 19** (1979) 342.

[26] T. Chapuran, R. Vodhanel, and M.K. Brussel, Phys. Rev. **C 22** (1980) 1420.

[27] D.F. Coope, L.E. Cannell, and M.K. Brussel, Phys. Rev. **C 15** (1977) 1977.

[28] J. Enders, P. von Brentano, J. Eberth, A. Fitzler, C. Fransen, R.-D. Herzberg, H. Kaiser, L. Käubler, P. von Neumann-Cosel, N. Pietralla, V.Yu. Ponomarev, A. Richter, R. Schwengner, and I. Wiedenhöver, Nucl. Phys. **A 724** (2003) 243.

[29] N. Ryezayeva, T. Hartmann, Y. Kalmykov, H. Lenske, P. von Neumann–Cosel, V.Yu. Ponomarev, A. Richter, A. Shevchenko, S. Volz, and J. Wambach, Phys. Rev. Lett. **89** (2002) 272502.

[30] T. Shizuma, T. Hayakawa, H. Ohgaki, H. Toyokawa, T. Komatsubara, N. Kikuzawa, A. Tamii, and H. Nakada, Phys. Rev. **C 78** (2008) 061303(R).

[31] R. Schwengner, R. Massarczyk, B.A. Brown, R. Beyer, F. Dönau, M. Erhard, E. Grosse, A.R. Junghans, K. Kosev, C. Nair, G. Rusev, K.D. Schilling, and A. Wagner, Phys. Rev. **C 81** (2010) 054315.

[32] S. Typel and B. Alex Brown, Phys. Rev. **C 64** (2001) 027302.

[33] B.A. Brown, Phys. Rev. Lett. **85** (2000) 5296.

[34] R.J. Furnstahl, Nucl. Phys. **A 706** (2002) 85.

[35] M. Centelles, X. Roca-Maza, X. Viñas, and M. Warda, Phys. Rev. Lett. **102** (2009) 122502.

[36] `http://hallaweb.jlab.org/parity/prex`.

[37] C.J. Horowitz, S.J. Pollock, P.A. Souder, and R. Michaels, Phys. Rev. **C 63** (2001) 025501.

[38] P.-G. Reinhard and W. Nazarewicz, Phys. Rev. **C 81** (2010) 051303(R).

[39] J. Piekarewicz, arXiv:1012.1803v1 [nucl-th] (2010).

[40] T. Rauscher, F.-K. Thielemann, At. Data Nucl. Data Tables 75 (2000) 1.

[41] S. Goriely, Phys. Lett. **B 436** (1998) 10.

[42] A.C. Larsen and S. Goriely, Phys. Rev. **C 82** (2010) 014318.

[43] E. Litvinova, H.P. Loens, K. Langanke, G. Martínez-Pinedo, T. Rauscher, P. Ring, F.-K. Thielemann, V. Tselyaev Nucl. Phys. **A 823** (2009) 159.

[44] R. Capote, M. Herman, P. Oblozinsky, P.G. Young, S. Goriely, T. Belgya, A.V. Ignatyuk, A.J. Koning, S. Hilaire, V.A. Plujko, M. Avrigeanu, O. Bersillon, M.B. Chadwick, T. Fukahori, Zhigang Ge, Yinlu Han, S. Kailas, J. Kopecky, V.M. Maslov, G. Reffo, M. Sin, E.Sh. Soukhovitskii, and P. Talou, Nucl. Data Sheets **110** (2009) 3107, `http://www-nds.iaea.org/RIPL-3/`.

[45] G.A. Bartholomew, E.D. Earle, A.J. Ferguson, J.W. Knowles, and M.A. Lone, *Advances in nuclear physics* **7** (1973) 229.

[46] P. Axel, Phys. Rev. **126** (1962) 671.

[47] D.M. Brink, Doctoral thesis, Oxford University (1955).

[48] N. Bohr, Nature **137** (1936) 344.

[49] H.K. Toft, A.C. Larsen, U. Agvaanluvsan, A. Bürger, M. Guttormsen, G.E. Mitchell, H.T. Nyhus, A. Schiller, S. Siem, N.U.H. Syed, and A. Voinov Phys. Rev. **C 81** (2010) 064311.

[50] A. Schiller, L. Bergholt, M. Guttormsen, E. Melby, J. Rekstad, and S. Siem, Nucl. Instr. Meth. **A 447** (2000) 498.

[51] H. Beil, R. Bergère, P. Carlos, A. Leprêtre, A. De Miniac, A. Veyssière, Nucl. Phys. **A 227** (1974) 427.

[52] G. Rusev, R. Schwengner, F. Dönau, M. Erhard, S. Frauendorf, E. Grosse, A.R. Junghans, L.Käubler, K. Kosev, L.K. Kostov, S. Mallion, K.D. Schilling, A. Wagner, H. von Garrel, U. Kneissl, C. Kohstall, M. Kreutz, H.H. Pitz, M. Scheck, F. Stedile, P. von Brentano, C. Fransen, J. Jolie, A. Linnemann, N. Pietralla, and V. Werner, Phys. Rev. **C 73** (2006) 044308.

[53] G. Rusev, R. Schwengner, F. Dönau, M. Erhard, E. Grosse, A.R. Junghans, K. Kosev, K.D. Schilling, A. Wagner, F. Bečvář, and M. Krtička, Phys. Rev. **C 77** (2008) 064321.

[54] M. Guttormsen, R. Chankova, U. Agvaanluvsan, E. Algin, L.A. Bernstein, F. Ingebretsen, T. Lönnroth, S. Messelt, G.E. Mitchell, J. Rekstad, A. Schiller, S. Siem, A. C. Sunde, A. Voinov, and S. Ødegård, Phys. Rev. **C 71** (2005) 044307.

[55] M. Krtička and F. Bečvář, EPJ Web of Conferences **2** (2010) 03002.

[56] K. Alder, A. Winther, *Electromagnetic excitation*, (North-Holland, Amsterdam, 1975).

[57] E. Fermi, Z. Phys. **29** (1924) 315.

[58] C.F. Weizsäcker, Z. Phys. **88** (1934) 612.

[59] E.J. Williams, Phys. Rev. **45** (1934) 729.

[60] K. Heyde, P. von Neumann-Cosel, and A. Richter, Rev. Mod. Phys. **82** (2010) 2365.

[61] K. Langanke, G. Martínez-Pinedo, P. von Neumann-Cosel, and A. Richter, Phys. Rev. Lett. **93** (2004) 202501.

[62] K. Langanke, G. Martínez-Pinedo, B. Müller, H.-Th. Janka, A. Marek, W.R. Hix, A. Juodagalvis, and J.M. Sampaio, Phys. Rev. Lett. **100** (2008) 011101.

[63] N. Jachowicz, K. Heyde, and J. Ryckebusch, Phys. Rev. **C 66** (2002) 055501.

[64] R.M. Laszewski and J. Wambach, Comments Nucl. Part. Phys. **14** (1985) 321.

[65] D. Vergados, Phys. Lett. **B 36** (1971) 12.

[66] K. Wienhard, W. Naatz, A. Ruckelshausen, D. Ruck, R.K. Schneider, and R. Stock, Phys. Rev. Lett. **49** (1982) 18.

[67] S. Müller, G. Küchler, A. Richter, H. P. Blok, H. Blok, C. W. de Jager, H. de Vries, and J. Wambach, Phys. Rev. Lett. **54** (1985) 293.

[68] S.I. Hayakawa, M. Fujiwara, S. Imanishi, Y. Fujita, I. Katayama, S. Morinobu, T. Yamazaki, T. Itahashi, and H. Ikegami, Phys. Rev. Lett. **49** (1982) 1624.

[69] J.L. Tain, G.P.A. Berg, I. Katayama, S.A. Martin, J. Meissburger, J.G.M. Römer, and J. Wambach, Phys. Rev. **C 35** (1987) 1288.

[70] C. Djalali, N. Marty, M. Morlet, A. Willis, J.C. Jourdain, N. Anantaraman, G.M. Crawley, and A. Galonsky, Phys. Rev. **C 31** (1985) 758.

[71] R.M. Laszewski, R. Alarcon, D.S. Dale, and S.D. Hoblit, Phys. Rev. Lett. **61** 1710 (1988).

[72] C. Djalali, M. Morlet, N. Marty, J. Van de Wiele, A. Willis, F.T. Baker, L. Bimbot, C. Glashausser, J. Guillot, H. Langevin-Joliot, L. Rosier, and E. Tomasi-Gustafsson, Phys. Rev. **C 59** (1999) 118.

[73] M. Schanz, A. Richter, and E. Lipparini, Phys. Rev. **C 36** (1987) 555.

[74] A. Tamii, Y. Fujita, H. Matsubara, T. Adachi, J. Carter, M. Dozono, H. Fujita, K. Fujita, H. Hashimoto, K. Hatanaka, T. Itahashi, M. Itoh, T. Kawabata, K. Nakanishi, S. Ninomiya, A.B. Perez-Cerdan, L. Popescu, B. Rubio, T. Saito, H. Sakaguchi, Y. Sakemi, Y. Sasamoto, Y. Shimbara, Y. Shimizu, F.D. Smit, Y. Tameshige, M. Yosoi, and J. Zenhiro, Nucl. Instr. Meth. **A 605** (2009) 3.

[75] P.F. Bortignon, A. Bracco, and R.A. Broglia, *Giant resonances: nuclear structure at finite temperature* (Harwood Academic, Amsterdam, 1998).

[76] B. Block and H. Feshbach, Ann. Phys. (N.Y.) **23** (1963) 47.

[77] H. Feshbach, Rev. Mod. Phys. **36** (1964) 1076.

[78] H. Feshbach, Rev. Mod. Phys. **46** (1974) 1.

[79] Y. Kalmykov, *Fine structure of the Gamow-Teller resonance in* ^{90}*Nb and* ^{168}*Tm studied with the (*^{3}*He,t) reaction at 0°*, Doctoral thesis D17, TU Darmstadt (2004).

[80] S. Strauch, P. von Neumann-Cosel, C. Rangacharyulu, A. Richter, G. Schrieder, K. Schweda, and J. Wambach, Phys. Rev. Lett. **85** (2000) 2913.

[81] P. von Neumann-Cosel, F. Neumeyer, S. Nishizaki, V.Yu. Ponomarev, C. Rangacharyulu, B. Reitz, A. Richter, G. Schrieder, D.I. Sober, T. Waindzoch, and J. Wambach, Phys. Rev. Lett. **82** (1999) 1105.

[82] Y. Kalmykov, T. Adachi, G.P.A. Berg, H. Fujita, K. Fujita, Y. Fujita, K. Hatanaka, J. Kamiya, K. Nakanishi, P. von Neumann-Cosel, V.Yu. Ponomarev, A. Richter, N. Sakamoto, Y. Sakemi, A. Shevchenko, Y. Shimbara, Y. Shimizu, F.D. Smit, T. Wakasa, J. Wambach, and M. Yosoi, Phys. Rev. Lett. **96** (2006) 012502.

[83] A. Shevchenko, O. Burda, J. Carter, G.R.J. Cooper, R.W. Fearick, S.V. Förtsch, H. Fujita, Y. Fujita, Y. Kalmykov, D. Lacroix, J.J. Lawrie, P. von Neumann-Cosel, R. Neveling, V.Yu. Ponomarev, A. Richter, E. Sideras-Haddad, F. D. Smit, and J. Wambach, Phys. Rev. **C 79** (2009) 044305.

[84] T. Walcher, R. Frey, H.-D. Gräf, E. Spamer, and H. Theissen, Nucl. Instr. Meth. **153** (1978) 17.

[85] Y. Fujita, K. Hatanaka, G.P.A. Berg, K. Hosono, N. Matsuoka, S. Morinobu, T. Noro, M. Sato, K. Tamura, and H. Ueno, Nucl. Instr. Meth. **B 126** (1997) 274.

[86] A. Schwierczinski, R. Frey, A. Richter, E. Spamer, H. Theissen, O. Titze, T. Walcher, S. Krewald, and R. Rosenfelder, Phys. Rev. Lett. **35** (1975) 1244.

[87] G. Kühner, D. Meuer, S. Müller, A. Richter, E. Spamer, O. Titze, and W. Knüpfer, Phys. Lett. **B 104** (1981) 189.

[88] A. Shevchenko, J. Carter, G.R.J. Cooper, R.W. Fearick, Y. Kalmykov, P. von Neumann-Cosel, V.Yu. Ponomarev, A. Richter, I. Usman, and J. Wambach, Phys. Rev. **C 77** (2008) 024302.

[89] A. Shevchenko, J. Carter, R.W. Fearick, S.V. Förtsch, H. Fujita, Y. Fujita, Y. Kalmykov, D. Lacroix, J.J. Lawrie, P. von Neumann-Cosel, R. Neveling, V.Yu. Ponomarev, A. Richter, E. Sideras-Haddad, F.D. Smit, and J. Wambach, Phys. Rev. Lett. **93** (2004) 122501.

[90] P.G. Hansen, B. Jonson, and A. Richter, Nucl. Phys. **A 518** (1990) 13.

[91] W.G. Love and M.A. Franey, Phys. Rev. **C 24** (1981) 1073.

[92] M.A. Franey and W.G. Love, Phys. Rev. **C 31** (1985) 488.

[93] K. Amos, P.J. Dortmans, H.V. von Geramb, S. Karataglidis, and J. Raynal, Adv. Nucl. Phys. **25** (2000) 275.

[94] G.R. Satchler, *Direct nuclear reactions*, (Oxford University Press, New York, 1983).

[95] J. Raynal, Computing code DWBA07, NEA Data Service NEA1209/08.

[96] H.V. von Geramb, *Interactions between medium energy nucleons in nuclei*, AIP Conf. Proc. **97** (1983) 44.

[97] S. Karataglidis, P.J. Dortmans, K. Amos, and R. de Swiniarski, Phys. Rev. **C 52** (1995) 861.

[98] A. Winther and K. Alder, Nucl. Phys. **A 319** (1979) 518.

[99] C.A. Bertulani and G. Baur, Nucl. Phys. **A 442** (1985) 739.

[100] G.G. Ohlsen, Rep. Prog. Phys. **35** (1972) 717.

[101] L. Wolfenstein, Annu. Rev. Nucl. Sci. **6** (1956) 43.

[102] X.Y. Chen, J.R. Shepard, M.R. Braunstein, T.A. Carey, K.W. Jones, J.B. McClelland, L. Rees, T.N. Taddeucci, N. Tanaka, and A.D. Bacher, Phys. Rev. **C 44** (1991) 2041.

[103] T. Kawabata, *Polarization transfer in the* $^{16}O(\vec{p},\vec{p}')$ *reaction at forward angles and structure of the spin-dipole resonance*, Doctoral thesis, Kyoto University, Japan (2002).

[104] A.K. Kerman, H. McManus, and R.M. Thaler, Ann. Phys. (N.Y.) **6** (1959) 551.

[105] J.M. Moss, Phys. Rev. **C 26** (1982) 727.

[106] T. Suzuki, Prog. Theor. Phys. **321** (2000) 859.

[107] H. Sakai, T. Wakasa, H. Okamura, T. Nonaka, T. Ohnishi, K. Yako, K. Sekiguchi, S. Fujita, Y. Satou, H. Otsu, T. Uesaka, S. Ishida, N. Sakamoto, M.B. Greenfield, and K. Hatanaka, Proceedings of the International Symposium of New Facet of Spin Giant Resonances in Nuclei, Tokyo, Japan, 1997, edited by H. Sakai, H. Okamura, and T.Wakasa (World Scientific, Singapore 1998) p.29.

[108] A. Tamii, H. Akimune, I. Daito, Y. Fujita, M. Fujiwara, K. Hatanaka, K. Hosono, F. Ihara, T. Inomata, T. Ishikawa, M. Itoh, M. Kawabata, T. Kawabata, M. Nakamura, T. Noro, E. Obayashi, H. Sakaguchi, H. Takeda, T. Taki, H. Toyokawa, H.P. Yoshida, M. Yoshimura, and M. Yosoi, Phys. Lett. **B 459** (1999) 61.

[109] T. Kawabata, T. Ishikawa, M. Itoh, M. Nakamura, H. Sakaguchi, H. Takeda, T. Taki, M. Uchida, Y. Yasuda, M. Yosoi, H. Akimune, K. Yamasaki, G.P.A. Berg, H. Fujimura, K. Hara, K. Hatanaka, J. Kamiya, T. Noro, E. Obayashi, T. Wakasa, H.P. Yoshida, H. Fujita, Y. Fujita, Y. Shimbara, H. Ueno, M. Fujiwara, K. Hosono, A. Tamii, and H. Toyokawa, Phys. Rev. **C 65** (2002) 064316.

[110] V.G. Soloviev, *Theory of atomic nuclei: quasiparticles and phonons*, (IOP Publishing, Bristol, 1992).

[111] C.A. Bertulani and V.Yu. Ponomarev, Phys. Rep. **321** (1999) 139.

[112] B. Reitz, A.M. van den Berg, D. Frekers, F. Hofmann, M. de Huu, Y. Kalmykov, H. Lenske, P. von Neumann-Cosel, V.Yu. Ponomarev, S. Rakers, A. Richter, G. Schrieder, K. Schweda, J. Wambach, and H.J. Wörtche, Phys. Lett. **B 532** (2002) 179.

[113] V.Yu. Ponomarev and P. von Neumann-Cosel, Phys. Rev. Lett. **82** (1999) 501.

[114] V.Yu. Ponomarev, V.G. Soloviev, C. Stoyanov, and A.I Vdovin, Nucl. Phys. **A 323** (1979) 446.

[115] C. Walz, H. Fujita, A. Krugmann, P. von Neumann-Cosel, N. Pietralla, V. Yu. Ponomarev, A. Scheikh-Obeid, and J. Wambach, Phys. Rev. Lett. **106** (2011) 062501.

[116] P. Ring and E. Litvinova, Phys. At. Nuc. **72** (2009) 1285.

[117] E. Litvinova, P. Ring, and V.I. Tselyaev, Phys. Rev. **C 75** (2007) 064308.

[118] Y.K. Gambhir, P. Ring, and A. Thimet, Ann. Phys. (N.Y.) **198** (1990) 132.

[119] P. Ring, Z.-Y. Ma, N. Van Giai, D. Vretenar, A. Wandelt, and L.-G. Cao, Nucl. Phys. **A 694** (2001) 249.

[120] N. Paar, P. Ring, T. Nikšíc, and D. Vretenar, Phys. Rev. **C 67** (2003) 034312.

[121] A. Bohr and B. Mottelson, *Nuclear structure* (Benjamin, Reading, Mass., 1975)

[122] G.A. Lalazissis, J. König, and P. Ring, Phys. Rev. **C 55** (1997) 540.

[123] V.I. Tselyaev, Yad. Fiz. 50 (1989) 1252.

[124] E. Litvinova, P. Ring, and V.I. Tselyaev, arXiv:0910.4343v2 [nucl-th] (2009).

[125] E. Litvinova, P. Ring, V.I. Tselyaev, and K. Langanke, Phys. Rev. **C 79** (2009) 054312.

[126] J. Endres, E. Litvinova, D. Savran, P. A. Butler, M. N. Harakeh, S. Harissopulos, R.-D. Herzberg, R. Krücken, A. Lagoyannis, N. Pietralla, V. Yu. Ponomarev, L. Popescu, P. Ring, M. Scheck, K. Sonnabend, V. I. Stoica, H. J. Wörtche, and A. Zilges, Phys. Rev. Lett. **105**, (2010) 212503.

[127] O. Wieland, A. Bracco, F. Camera, G. Benzoni, N. Blasi, S. Brambilla, F.C.L. Crespi, S. Leoni, B. Million, R. Nicolini, A. Maj, P. Bednarczyk, J. Grebosz, M. Kmiecik, W. Meczynski, J. Styczen, T. Aumann, A. Banu, T. Beck, F. Becker, L. Caceres, P. Doornenbal, H. Emling, J. Gerl, H. Geissel, M. Gorska, O. Kavatsyuk, M. Kavatsyuk, I. Kojouharov, N. Kurz, R. Lozeva, N. Saito, T. Saito, H. Schaffner, H.J. Wollersheim, J. Jolie, P. Reiter, N. Warr, G. deAngelis, A. Gadea, D. Napoli, S. Lenzi, S. Lunardi,, D. Balabanski, G. LoBianco, C. Petrache, A. Saltarelli, M. Castoldi, A. Zucchiatti, J. Walker, and A. Bürger, Phys. Rev. Lett. **102** (2009) 092502.

[128] P. Demetriou and S. Goriely, Nucl. Phys. **A 695** (2001) 95.

[129] S. Hilaire, J.P. Delaroche, and M. Girod, Eur. Phys. J. **A 12** (2001) 169.

[130] E. Gadioli and L. Zetta, Phys. Rev. **167** (1968) 1016.

[131] J.R. Huizenga, H.K. Vonach, A.A. Katsanos, A.J. Gorski, and C.J. Stephan, Phys. Rev. **182** (1969) 1149.

[132] H. Vonach and M. Hille, Nucl. Phys. **A 127** (1969) 289.

[133] H.A. Bethe, Rev. Mod. Phys. **9** (1937) 69.

[134] W. Dilg, W. Schantl, H. Vonach, and M. Uhl, Nucl. Phys. **A 217** (1973) 269.

[135] T. Rauscher, F.–K. Thielemann, and K.–L. Kratz, Phys. Rev. **C 58** (1997) 1613.

[136] T.E.O. Ericson, Adv. Phys. **9** (1960) 425.

[137] T. von Egidy, H. H. Schmidt, and A. N. Behkami, Nucl. Phys. **A 481** (1988) 189.

[138] A. V. Voinov, B. M. Oginni, S. M. Grimes, C. R. Brune, M. Guttormsen, A. V. Larsen, T. N. Massey, A. Schiller, and S. Siem, Phys. Rev. **C 79** (2009) 031301(R).

[139] K. Hatanaka, K. Takahisa, H. Tamura, M. Sato, and I. Miura, Nucl. Instr. Meth. **A 384** (1997) 575.

[140] T. Shimoda, H. Miyatake, S. Morinobu Nucl. Instr. Meth. **B 70** (1992) 320.

[141] H. Sakai, H. Okamura, H. Otsu, T. Wakasa, S. Ishida, N. Sakamoto, T. Uesaka, Y. Satou, S. Fujita, K. Hatanaka Nucl. Instr. Meth. **A 369** (1996) 120.

[142] T. Wakasa, K. Hatanaka, Y. Fujita, G.P.A. Berg, H. Fujimura, H. Fujita, M. Itoh, J. Kamiya, T. Kawabata, K. Nagayama, T. Noro, H. Sakaguchi, Y. Shimbara, H. Takeda, K. Tamura, H. Ueno, M. Uchida, M. Uraki, and M. Yosoi, Nucl. Instr. Meth. **A 482** (2002) 79.

[143] M. Fujiwara, H. Akimune, I. Daito, H. Fujimura, Y. Fujita, K. Hatanaka, H. Ikegami, I. Katayama, K. Nagayama, N. Matsuoka, S. Morinobu, T. Noro, M. Yoshimura, K. Sakaguchi, Y. Sakemi, A. Tamii, and M. Yosoi, Nucl. Instr. Meth. **A 422** (1999) 484.

[144] T. Noro, Y. Mizuno, H. Togawa, S. Hirata, N. Matsuoka, O. Kamigaito, F. Hiei, Y. Sakemi, H. Akimune, and T. Takahashi, RCNP Annual Report (1990) 217.

[145] M. Yosoi, H. Akimune, I. Daito, H. Fujiwara, S. Hirata, , T. Inomata, O. Kamigaito, M. Kawabata, T. Noro, H. Sakaguchi, Y. Sakemi, T. Takahashi, A. Tamii, S. Toyama, A. Yamagoshi, M. Yoshimura, AIP Conf. Proc. **343** (1995) 157.

[146] N. Matsuoka, K. Hatanaka, S. Morinobu, T. Noro, A. Okihana, and K. Sagara, RCNP Annual Report (1991) 186.

[147] H. Fujita, Y. Fujita, G.P.A. Berg, A.D. Bacher, C.C. Foster, K. Hara, K. Hatanaka, T. Kawabata, T. Noro, H. Sakaguchi, Y. Shimbara, T. Shinada, E.J. Stephenson, H. Ueno, and M. Yosoi, Nucl. Instr. Meth. **A 484** (2002) 17.

[148] H. Takeda, *Modification of nucleon–nucleon interactions in nuclear medium and neutron densities extracted via proton elastic scattering at intermediate energies*, Doctoral thesis, Kyoto University, Japan (2002).

[149] N. Matsuoka and T. Noro, RCNP Annual Report (1987) 176.

[150] A. Tamii, *Polarization transfer observables from proton inelastic scattering from* ^{12}C *at zero degrees*, Doctoral thesis, Kyoto University, Japan (1999).

[151] A. Tamii, H. Sakaguchi, H. Takeda, M. Yosoi, H. Akimune, M. Fujiwara, H. Ogata, M. Tanaka, and H. Togawa, IEEE Trans. on Nucl. Sci. **43** (1996) 2488.

[152] T. Kawabata, H. Sakaguchi, A. Tamii, H. Takeda, T. Taki, and H. Yoshida, RCNP Annual Report (1996) 161.

[153] N. Fujita, H. Sakaguchi, Y. Maeda, A. Nonaka, H. Okamura, A. Tamii, J. Zenihiro, H. Matsubara, D. Ishikawa, T. Terashima, and Y. Yasuda, RCNP Annual Report (2008) 186.

[154] A. Tamii, priv. communication.

[155] `http://cern.ch/paw/`,
`http://cern.ch/cernlib/`.

[156] G.F. Knoll, *Radiation detection and measurement*, 3^{rd} ed., (John Wiley & Sons, New York, 2000).

[157] M. Galassi, J. Davies, J. Theiler, B. Gough, B. Jungman, M. Booth, and F. Rossi, *GNU Scientific Library Reference Manual*, 2nd ed. (Network Theory Ltd., Bristol, 2003); `http://www.gnu.org/software/gsl/`.

[158] `http://www.nndc.bnl.gov/nudat2`.

[159] Computer program KINMAT, iThemba Laboratory for Accelerator Based Sciences, Faure, South Africa, unpublished.

[160] N. Braun, Computer programm HDTV, `https://www.ikp.uni-koeln.de/projects/hdtv/trac/`.

[161] D. Besset, B. Faviera, L.G. Greeniaus, R. Hessa, C. Lechanoinea, D. Rapina, and D.W. Werren, Nucl. Instr. Meth. **166** (1979) 515.

[162] T. Wakasa, H. Sakai, H. Okamura, H. Otsu, N. Sakamoto, T. Uesaka a, Y. Satou, S. Fujita, S. Ishida, M.B. Greenfield, N. Koori, A. Okihana, and K. Hatanaka, Nucl. Phys. **A 599** (1996) 217c.

[163] T. Wakasa, H. Sakai, H. Okamura, H. Otsu, S. Fujita, S. Ishida, N. Sakamoto, T. Uesaka, and Y. Satou, Phys. Rev. **C 55** (1997) 2909.

[164] B. Bonin, N. Alamanos, B. Berthier, G. Bruge, H. Faraggi, D. Legrand, J.C. Lugol, W. Mittig, L. Papineau, A.I. Yavin, D.K. Scott, M. Levine, J. Arvieux, L. Farvacque, and M. Buenerd, Nucl. Phys. **A 430** (1984) 349.

[165] U. Garg, T. Li, S. Okumura, H. Akimune, M. Fujiwara, M.N. Harakeh, H. Hashimoto, M. Itoh, Y. Iwao, T. Kawabata, K. Kawase, Y. Liu, R. Marks, T. Murakami, K. Nakanishi, B.K. Nayak, P.V. Madhusudhana Rao, H. Sakaguchi, Y. Terashima, M. Uchida, Y. Yasuda, M. Yosoi, and J. Zenihiro, Nucl. Phys. **A 788** (2007) 36c.

[166] M.J. Martin, Nucl. Data Sheets **108** (2007) 1583.

[167] F.T. Baker, L. Bimbot, C. Djalali, C. Glashausser, H. Lenske, W.G. Love, M. Morlet, E. Tomasi-Gustafsson, J. Van de Wiele, J. Wambach, and A. Willis, Phys. Rep. **289** (1997) 235.

[168] A. Veyssière, H. Beil, R. Bergère, P. Carlos, and A. Lepretre, Nucl. Phys. **A 159** (1970) 561.

[169] Z.W. Bell, L.S. Cardman and P. Axel, Phys. Rev. **C 25** (1982) 791.

[170] K. P. Schelhaas, J. M. Henneberg, M. Sanzone-Arenhövel, N. Wieloch-Laufenberg, U. Zurmühl, B. Ziegler, M. Schumacher, and F. Wolf, Nucl. Phys. **A 489** (1988) 189.

[171] O. Bohigas, Nguyen Van Giai, and D. Vautherin, Phys. Lett. **B 102** (1981) 105.

[172] J. Zenihiro, H. Sakaguchi, T. Murakami, M. Yosoi, Y. Yasuda, S. Terashima, Y. Iwao, H. Takeda, M. Itoh, H. P. Yoshida, and M. Uchida, Phys. Rev. **C 82** (2010) 044611.

[173] A. Trzciáska, J. Jastrzçbski, P. Lubiáski, F. J. Hartmann, R. Schmidt, T. von Egidy, and B. Kłos, Phys. Rev. Lett. **87** (2001) 082501.

[174] D. Bucurescu and T. von Egidy, J. Phys. **G 31** (2005) 1675.

[175] N.U.H. Syed, M. Guttormsen, F. Ingebretsen, A.C. Larsen, T. Lönnroth, J. Rekstad, A. Schiller, S. Siem, and A. Voinov, Phys. Rev. **C 79** (2009) 024316.

[176] C.M. McCullagh, M.L. Stelts, and R.E. Chrien, Phys. Rev. **C 23** (1981) 1394.

[177] S.N. Belyaev, O.V. Vasil'ev, V.V. Voronov, A.A. Nechkin, V.Yu. Ponomarev, and V.A. Semenov, Yad. Fiz. **55**, (1992) 289.

[178] I. Daubechies, *Ten lectures on wavelets*, SIAM, 1992.

[179] J. S. Byrnes, *Wavelets and their Applications*, (Kluwer Academic Publischer, Dordrecht, 1992).

[180] C. Torrence and G. Compo, Bull. Amer. Meteor. Soc. **79** (1998) 61.

[181] I. Ireland, R. Walsh, R. Harrison, and E. Priest, Astron. Astrophys. **347** (1999) 355.

[182] A. Fedorova, M. Zeitlin, and Z. Parsa, in: Proc. PAC97, Vol. 2, 1998, pp. 1502, 1505, 1508.

[183] A. Shevchenko, O. Burda, J. Carter, G. R. J. Cooper, R. W. Fearick, S. V. Förtsch, H. Fujita, Y. Fujita, Y. Kalmykov, D. Lacroix, J. J. Lawrie, P. von Neumann-Cosel, R. Neveling, V. Yu. Ponomarev, A. Richter, E. Sideras-Haddad, F. D. Smit, and J. Wambach, Phys. Rev. **C 79** (2009) 044305.

[184] T. von Egidy, H.H. Schmidt, and A.N. Behkami, Nucl. Phys. **A 481** (1988) 189.

[185] T. von Egidy and D. Buchurescu, Phys. Rev. **C 72** (2005) 044311.

[186] T. von Egidy and D. Bucurescu, Phys. Rev. **C 80** (2009) 054310-1.

[187] S. Hilaire and S. Goriely, Nucl. Phys. **A 779** (2006) 63.

[188] B. Jonson, E. Hagberg, P.G. Hansen, P. Hornshøj, and P. Tidemand–Petersson, *Proc. 3rd Int. Conf. on Nuclei far from Stability*, Cargèse, 1976, CERN **76–13** (1976) 277.

[189] P.G. Hansen, Annu. Rev. Nucl. Part. Sci. **29** (1979) 69.

[190] S. Müller, *Untersuchung transversaler elektrischer Dipolanregungen in ^{90}Zr und Bestimmung von Protonen und Neutronen spinflip Amplituden in der Anregung des $J^{\pi} = 1^{+}$ Zustands bei $E_x = 5.845$ MeV in ^{208}Pb mit inelastischer Elektronenstreuung*, Doctoral thesis D17, TH Darmstadt (1983).

[191] F. Neumeyer, *Untersuchung magnetischer Kernanregungen in ^{48}Ca und ^{90}Zr mit hochauflösender Elektronenstreuung unter 180°am S-DALINAC*, Doctoral thesis D17, TU Darmstadt (1997).

[192] B. Reitz, *Weiterentwicklung des Detektorsystems am QCLAM−Spektrometer des S−DALINAC und Untersuchung der Reaktionen ^{48}Ca(e,e′) und ^{58}Ni(e,e′) unter 180°*. Docotral thesis D17, TU Darmstadt (2000).

[193] E.P. Wigner, in: C.E. Porter (Ed.), *Statistical theories of spectra: fluctuations*, (Academic Press, New York, 1965) 200.

[194] C.E. Porter and R.G. Thomas, Phys. Rev. **104** (1956) 483.

[195] T. Guhr, A. Müller–Groeling, and H.A. Weidenmüller, Phys. Rep. **299** (1998) 189.

[196] R. U. Haq, A. Pandey, and O. Bohigas, Phys. Rev. Lett. **48** (1982) 1086.

Danksagung

Hiermit möchte ich mich bei allen herzlich bedanken, die mich durch ihren überdurchschnittlichen Einsatz bei der Entstehung dieser Arbeit unterstützt haben.

Als erstes möchte ich mich bei Herrn Prof. Dr. Peter von Neumann-Cosel für die Aufnahme in seine Arbeitsgruppe bedanken. Mit großem Interesse und Unterstützung hat er den Fortgang meiner Arbeit begleitet und stand bei Fragen stets zur Verfügung. Dankbar bin ich ihm auch für die Möglichkeit an Tagungen und auswärtigen Experimenten teilzunehmen.

Herrn Professor Dr. Dr. h.c. mult. Achim Richter danke ich sehr dass er mir die Möglichkeit gab, an der Technischen Universität Darmstadt erst meine Master Arbeit durchzuführen und anschließend zu promovieren.

Herrn Professor Dr. Jochen Wambach danke ich für die Übernahme des Korreferates.

I am indebted to Professor Dr. Atsushi Tamii for the perusal of the manuscript and availability of the polarization observables calculations, as well as for fruitful discussions and his unresting and enormous help during the realization of the experiments.

My special thanks goes to the accelerator group of the RCNP, which provided an excellent beam, and all the collaborators for their countless help during the experiments. Special thank goes to the Dr. Hiroaki Matsubara for his support and encourage during my first stay in Japan.

I am grateful to Dr. Vladimir Ponomarev for the QPM calculations and a lot of helpful discussions, ideas and suggestions. I am also thankful to Dr. Elena Litvinova for the RQTBA calculations.

Weiterhin danke ich allen Arbeitskollegen aus dem IKP, insbesondere Anna Maria Krumbholz und Andreas Krugmann für die tolle Zusammenarbeit während Experimenten in Japan. Bei allen derzeitigen und ehemaligen Mitarbeitern der Spektrometer-Gruppe möchte ich für die gute Zusammenarbeit danken. Ich bedanke mich bei allen Mitstreitern aus dem Büro 22 für eine angenehme Arbeitsatmosphäre. Ich danke auch den Kollegen aus dem Arbeitszimmer 35, insbesondere Herrn Matthias Fritzsche, für hilfreiche Diskussionen während Kaffeepausen.

Herrn Dr. Harald Genz danke ich herzlich für die Zusammenarbeit bei verschiedenen Veranstaltungen und seine Hilfe und Unterstützung in alltäglichen Fragen und Problemen.

Zum Schluss möchte ich mich bei meiner Familie, besonders bei meiner Mama, meiner Schwester Olena und meine Oma Galyna, bedanken, die mich während des Studiums aus der Ukraine immer unterstützt haben. Ein besonderer Dank gilt meiner Zwillingsschwester Yuliya dafür daß sie immer für mich da ist. Ich danke auch den Familien Fritzsche und Zweidinger für die wertvolle Unterstützung. Ein großer und lieber Dank geht an meinen Freund Markus Zweidinger, der mir vor allem in der abschließenden Phase so viel Hilfe und Verständnis entgegen brachte.

Die vorliegende Arbeit wurde gefördert durch die DFG im Rahmen des Sonderforschungsbereich 634 und 446JAP 113/267/0-2.

Lebenslauf

Iryna Poltoratska

10. Februar 1982	Geboren in Kamjanets-Podilskyi, Ukraine
1989 – 1996	Gymnasium Nr. 14, Kamjanets-Podilskyi,Ukraine
1996 – 1999	Lyzeum Nr. 18, Kamjanets-Podilskyi, Ukraine
1999 – 2005	Studium der Physik an der Fakultät für Physik und Technik der Karazin Kharkiv National University, Ukraine, Vertiefungsrichtung Kernphysik
2002 - 2003	Praktikum an der Karazin Kharkiv National University, Ukraine, Bachelorstudiumabschluss. Thema: ”Pulsed Gamma Activation Analysis of Short-living Radionuclides ”
Juli 2004 - Feb. 2005	Diplompraktikum am Institut für Kernphysik der Technischen Universität Darmstadt
Februar 2005	Abschluss des Studiums mit Master of Science mit Auszeichnung. Thema: ”Dipole Strength in ^{112}Sn up to 7 MeV from a Nuclear Resonance Fluorescence Study at the S-DALINAC”
März 2005 - Sep. 2007	Stipendiatin der Technischen Universität Darmstadt in Rahmen Graduiertenkolleg 410: ”Physik und Technik von Beschleuniger”
seit Sep. 2007	Wissenschaftlicher Mitarbeiterin am Institut für Kernphysik der Technischen Universität Darmstadt

Erklärung zur Dissertation

Hiermit versichere ich, die vorliegende Dissertation ohne Hilfe Dritter nur mit den angegebenen Quellen und Hilfsmitteln angefertigt zu haben. Alle Stellen, die aus Quellen entnommen wurden, sind als solche kenntlich gemacht. Diese Arbeit hat in gleicher oder ähnlicher Form noch keiner Prüfungsbehörde vorgelegen.

Darmstadt, den 15. Februar 2011

(I. Poltoratska)